ARSENIC TRISULFIDE ON LITHIUM NIOBATE DEVICES FOR INFRARED INTEGRATED OPTICS

A Dissertation

by

XIN XIA

Submitted to the Office of Graduate Studies of
Texas A&M University
in partial fulfillment of the requirements for the degree of

DOCTOR OF PHILOSOPHY

May 2011

Major Subject: Electrical Engineering

ARSENIC TRISULFIDE ON LITHIUM NIOBATE DEVICES FOR INFRARED INTEGRATED OPTICS

A Dissertation

by

XIN XIA

Submitted to the Office of Graduate Studies of
Texas A&M University
in partial fulfillment of the requirements for the degree of

DOCTOR OF PHILOSOPHY

Approved by:

Chair of Committee,	Christi K. Madsen
Committee Members,	Ohannes Eknoyan
	Andrew K. Chan
	Michael B. Weimer
Head of Department,	Costas N. Georghiades

May 2011

Major Subject: Electrical Engineering

ABSTRACT

Arsenic Trisulfide on Lithium Niobate Devices for Infrared Integrated Optics.

(May 2011)

Xin Xia, B.S., Huazhong University of Science and Technology

Chair of Advisory Committee: Dr. Christi K. Madsen

Arsenic trisulfide (As_2S_3) waveguide devices on lithium niobate substrates ($LiNbO_3$) provide a set of compact and versatile means for guiding and manipulating optical modes in infrared integrated optical circuits, including the integrated trace gas detection system. As a member of the chalcogenide glass family, As_2S_3 has many properties superior to other materials, such as high transparency up to 10 μm, large refractive index and high nonlinear coefficient. At the wavelength of 4.8 μm, low-loss As_2S_3 waveguides are achieved: The propagation loss is 0.33 dB/cm; the coupling efficiency is estimated to be 81%; and less than 3 dB loss is measured for a 90-degree bent waveguide of 250 μm bending radius. They offer an ideal solution to the optical interconnection— the fundamental element of an optical circuit.

$LiNbO_3$ is a birefringent crystal that has long been studied as the substrate material. Titanium diffused waveguides in lithium niobate substrate (Ti: $LiNbO_3$) have excellent electro-optical properties, based on which, on-chip polarization converters are demonstrated. New benefits can be obtained by integrating As_2S_3 and Ti: $LiNbO_3$ to form a hybrid waveguide, which benefits from the high index contrast of As_2S_3 and the

electro-optical properties of Ti: $LiNbO_3$ as well as its easy connection with commercial single mode fibers.

For hybrid waveguides, the mode coupling is key. A taper coupler is preferred owing to its simplicity in design and fabrication. Although preliminary experiments have shown the feasibility of such integration, the underlying mechanism is not well understood and guidelines for design are lacking. Therefore, a simulation method is first developed and then applied to the taper coupler design. Devices based on taper couplers are then fabricated and characterized. The study reveals that in the presence of mode beating, it is not necessarily the longer taper that is the better coupling. There exists an optimum length for a taper with fixed width variation. A two-stage taper design can largely reduce the total length, e. g. by 64%, while keeping the coupling efficiency above 90%. According to the frequency domain analysis, these practical taper couplers work for a wavelength range instead of a single wavelength.

DEDICATION

To my family

ACKNOWLEDGEMENTS

I would like to thank my committee chair and advisor, Dr. Christi K. Madsen. This dissertation work would not have been possible without her expert guidance. I am very thankful for her encouragement and constant patience. I would also like to express my gratitude to other committee members, Dr. Ohannes Eknoyan, Dr. Andrew K. Chan and Dr. Michael B. Weimer, for their time and effort in guiding and supporting me throughout the course of this research.

I appreciate very much the help and discussions from my friends and colleagues. They are Mehmet Solmaz, Renato Rabelo, Donnie Adams, Weechong Tan, Xiaomin Song, Wonju Sung, W. Tim Snider, Jacob Webb, Yifeng Zhou, Qi Chen, Jae Kim, Xin Wang and Dwayne Denton. Besides, I am grateful to ISSE staff, Robert Atkins, Jim Gardner, Travis James and George Flores for their support and help.

I would like to thank my friends and colleagues in Mirthe as well. Thanks to Candice Tsay, Dr. Craig B. Arnold and Dr. Claire F. Gmachl from Princeton University for their help on building the quantum cascade laser setup; thanks to Elaine Lalanne, Sheng Liu and Dr. Anthony M. Johnson from UMBC for their help and discussion on experiments of direct light coupling; and thanks to Federico Lopez, Dingkai Guo, David Miller and a lot of other friends for the support and help in Mirthe as a big family.

Finally, I would like to thank my beloved wife Chang for her love, help and encouragement and our parents for their unconditional love and support.

TABLE OF CONTENTS

CHAPTER Page

LIST OF FIGURES

FIGURE Page

FIGURE Page

FIGURE Page

FIGURE Page

LIST OF TABLES

CHAPTER I

INTRODUCTION

1.1. Background and motivation

1.1.1. Integrated trace gas detection system

Infrared (IR) light is the electromagnetic radiation with a wavelength ranging from 769 nm to 100 μm, which can be further categorized as near IR (769 nm to 2.5 μm), mid IR (2.5 μm to 25 μm) and far IR (25 μm to 100 μm) [1]. Its wavelength is longer than that of visible light but shorter than that of microwaves. It has many applications: Fiber-optic telecommunication favors the wavelength around 1.5 μm because signals have low attenuation loss in the medium of silica fiber [2]. Infrared imaging is used extensively for military and civilian purposes, such as surveillance, night vision, remote temperature sensing, and spectroscopy. Among them, one of the most important applications is trace gas detection technique.

Trace gas detection techniques are based on transmission IR spectroscopy. The configuration is illustrated in Fig. 1. Light emitted from a wide-spectrum laser source passes through a volume of gas, and is incident onto an IR detector. During its propagation through the gas, the gas molecules absorb energy at certain wavelengths, forming the absorption spectrum, which can be obtained by converting the transmission spectrum received at the detector.

This dissertation follows the style of *Journal of Lightwave Technology*.

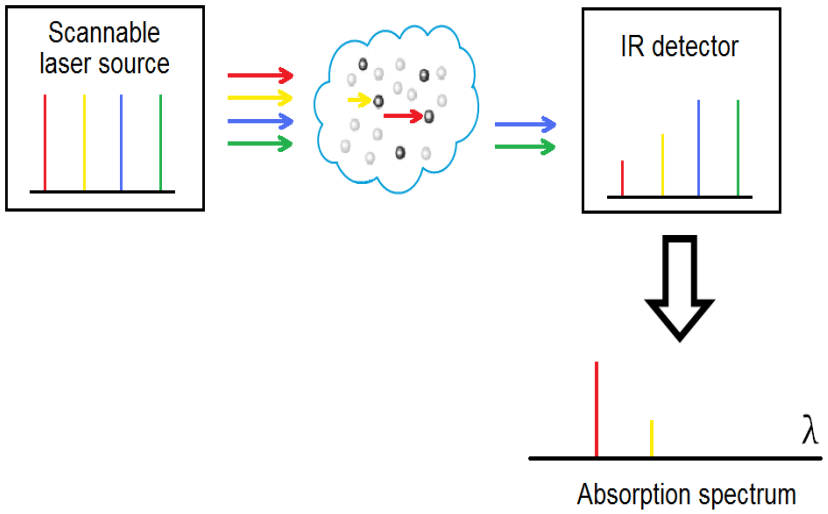

Fig. 1. Transmission spectroscopy.

The principle is that each kind of molecule exhibits a unique and strong absorption pattern in the wavelength range from 3 μm to 12 μm, i. e. falls into the mid IR region. By comparing that absorption spectrum of the gas with the standard molecule spectra, the information of molecules composition of the gas is then obtained.

Compared to other spectroscopy methods, trace gas detection techniques directly give the information of molecules instead of that of elements. In addition, it has three advantages. The first one is uniqueness: every molecule has its own particular absorption pattern that is like its fingerprint, because the light is absorbed by the fundamental vibrational bands that the gaseous chemical substances are composed of. A computer simulated absorption spectrum of a list of molecules is shown in Fig. 2 [3], where the wavelength is from 3 μm to 5 μm. Secondly, it has high sensitivity. The strength of the absorption peak is so large that it makes particle-per-billion and even single-molecule-detection possible. And thirdly, it is neither invasive nor destructive. Once realized, this

technology will have a considerable amount of applications in medical diagnostics in a fast and less painful way, monitoring atmosphere quality, industrial production and in the field of safety and security.

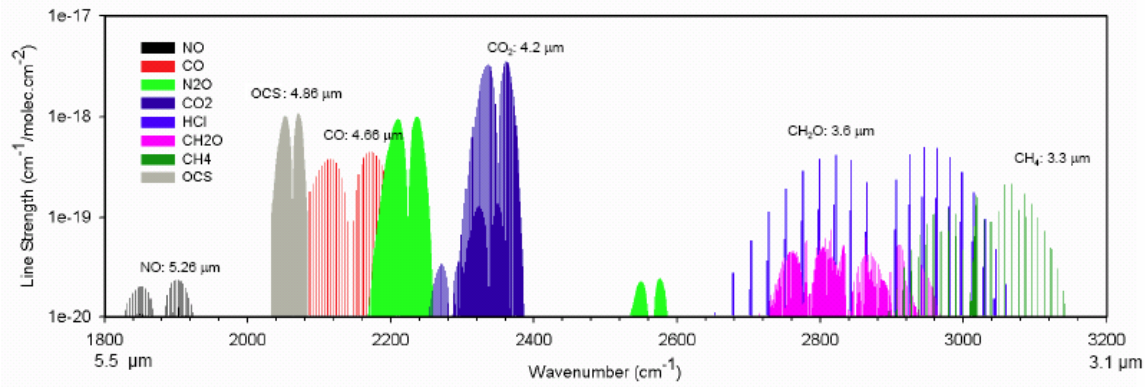

Fig. 2. Absorption spectrum of selected molecules.

Although the idea of trace gas detection has been demonstrated for a long time, it is not practically used. The reason is that the actual optical system requires bulky components, such as free-space lasers, detectors, wave plates and lenses, as Fig. 3 [3] shows. In order to make it practically useful, we have to make it compact and portable. The solution is optical integrated circuits, which are a thin-film-type optical circuit designed to have a certain function by integrating a laser diode as the source, functional components, such as switches or modulators, and interconnection waveguides and photodiodes as detectors, on a single substrate [4]. Through integration, a more compact, stable and functional optical system can be expected [4], and can be presumably fabricated by adapting the current Integrated Circuit (IC) fabrication technology. As a result, the volume can be increased and the cost can be lowered. But to realize it, we

have a long way to go. The first thing to do is to integrate the light source and the interconnection waveguide.

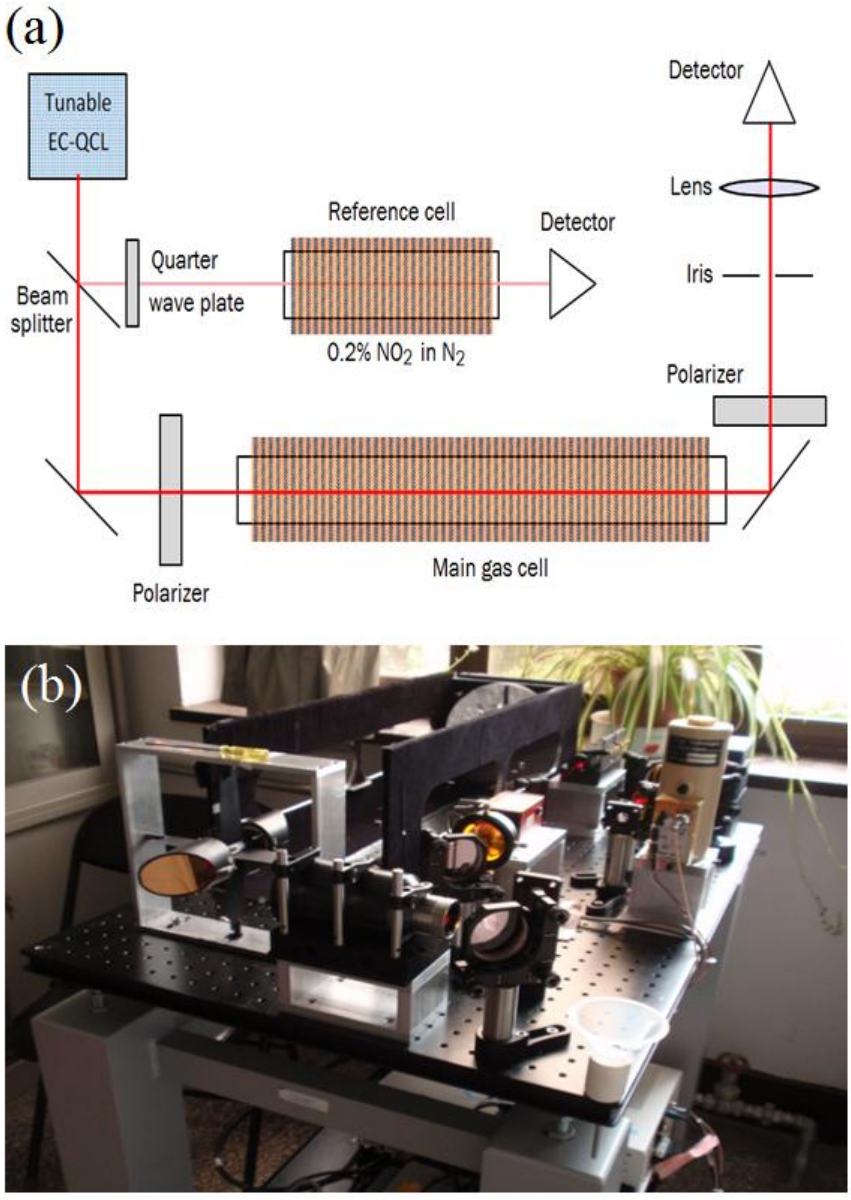

Fig. 3. Traditional trace gas detection system: schematic (a) and picture (b).

The invention of quantum cascade lasers (QC lasers) is the first step toward the goal of on-chip integration. It emits mid IR light based on the principle of inter-sub-band transition and tunneling between adjacent quantum wells. Compared to lead-salt lasers, III–V based antimonite inter-band lasers, or even inter-band lasers based on type II transitions, the QC lasers have the advantage of a large T_0 and higher temperature ~300 K operation [5]. Moreover, since they are small, compact and made by semiconductor fabrication technology— Molecular Beam Epitaxy (MBE) or Metal-Organic Chemical Vapor Deposition (MOCVD), they are ideal for integrated optics that enables on-chip photonic signal processing.

As the development of efficient, robust, widely tunable quantum cascade lasers are ongoing, there is an increasing significance to realize the interconnection— the optical waveguide, which is the pre-requisite to integrate the detector and other optical devices such switch and modulators for integrated trace gas detection system.

1.1.2. Chalcogenide glass waveguides and polarization converters

Among several choices of waveguide materials for mid IR, chalcogenide glass is a good candidate. Chalcogenide glass is a set of amorphous materials composed of chalcogen elements (sulphur, selenium and tellurium) covalently bonded with one or two structural elements such as Ge, As, Sb, Ga, etc [6]. Compared to silicon dioxide (SiO_2) that has strong absorption in the mid IR, they exhibit good transparency and potentially low loss for both 1.3–1.55 μm telecommunication windows and mid IR optical bands up to 10 μm in wavelength [7]. The transmittance spectra comparing to that of SiO_2 and

fluoride glasses (ZBLAN) are shown Fig. 4 [8], where we can see that the SiO_2 cutoff is around 4 μm, while telluride glass extends good transmittance to 20 μm. Generally speaking, the lower intrinsic loss is, the lower the absorption is, and the higher the transmission is. For our purpose, arsenic tri-sulfide (As_2S_3) is suitable and its property has long been studied [9]. Its large refractive index and high nonlinearity make it ideal for all optical signal processing [10]. On the downside, it is a very brittle material that requires careful handling and processing, and it is a photosensitive material, i.e., its refractive index can change as above-band-gap wavelength light shines on it, leading to the instability of the optical property of the material. But that problem can be eliminated by annealing after film deposition.

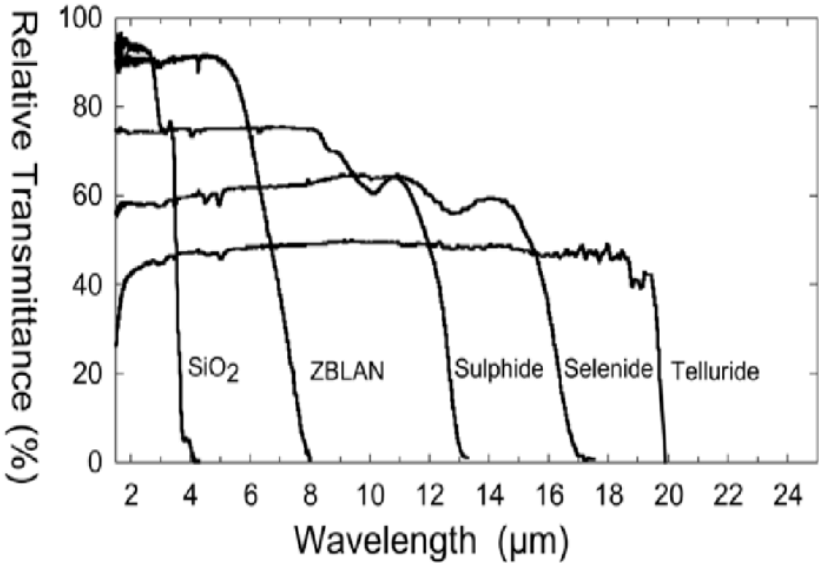

Fig. 4. Transmittance spectra of ordinary glasses.

An unfavorable characteristic of quantum cascade lasers is that it can only emit light in Transverse Magnetic (TM) polarized mode due to its working principle. But sometimes transverse electric (TE) polarized mode is preferred. Moreover, for some applications, such as Faraday Rotation Spectroscopy (a sensitive method for detecting radicals and ions, shown in Fig. 3), it is indispensable to have the function of polarization controll. So an integrated optical device, which is capable of on-chip polarization conversion, is in need. Electro-optic devices based on titanium diffused waveguide in lithium niobate (Ti: $LiNbO_3$) provides a promising solution. Utilizing the excellent electro-optical property of the lithium niobate crystal, the optical mode can be converted from TM mode to TE mode during propagation in a titanium diffused waveguide, or vice versa. However, Ti: $LiNbO_3$ suffers from the problem of weak confinement of the mode due to the small index contrast ($\Delta n<0.03\%$), which makes it difficult to fabricate compact structures with small features, such as tight bends and rings, and so it limits the application as an optical interconnect.

With chalcogenide (As_2S_3) waveguides, this problem can be easily overcome since the index contrast is as large as 20%. And furthermore, lithium niobate ($LiNbO_3$) is a very good substrate for As_2S_3 waveguides. First, it has a wider transmission range (2-5 μm) than SiO_2, which is transparent up to 3.5 μm only [8]). Secondly, the thermal expansion coefficient of $LiNbO_3$ (perpendicular 15×10^{-6} /℃ and parallel 5×10^{-6} /℃) is much closer to that of As_2S_3 (21.4×10^{-6} /℃) than SiO_2 (5×10^{-7} /℃), giving a better adherence between the film and the substrate during the thermal processes in waveguide fabrication. Therefore, if we can integrate both waveguides together, we can benefit

from the strong wave-guiding capability of As_2S_3 waveguide and meanwhile manipulate optical modes in more versatile ways taking advantage of electro-optic effect of Ti: $LiNbO_3$ [11] as well as the easy connection with commercial single mode fibers.

1.1.3. As_2S_3-Ti: $LiNbO_3$ mode couplers

Actually, the idea of integration of different materials, in other words, hybrid waveguides, can have a great significance to the whole field of integrated optics in a much wider scope.

Integrated optics, as the platform using photons for signal processing, has many advantages over traditional integrated electric circuits, such as substantially greater bandwidth and thus ultra-high speed. Considerable research has been carried out in this field and various promising schemes have been proposed, as shown in Table I. For example, silicon-on-insulator (SOI) waveguide were demonstrated to make compact structures such as sharp bends and rings, owing to its large refractive index contrast between the waveguide material silicon (n=3.5) and the substrate silica (n=1.45). Chalcogenide (ChG) glass waveguides exhibit ultra-low loss (0.05 dB/cm), broad transmission spectrum up to mid infrared (10 μm), and a large nonlinear coefficient. Titanium diffused waveguides in lithium niobate (Ti: $LiNbO_3$), on the other hand, have great electro-optical tuning capability and large mode field diameters comparable to that of single mode fibers and thus can seamlessly connect with current telecommunication systems. Although the cost is relatively high, III-V semiconductor waveguides can be easily built with III-V lasers and detectors.

Table I. Comparison of some integrated optical waveguides.

Waveguides	**SOI**	**ChG**	**Ti: $LiNbO_3$**	**III-V**
Index contrast	~60%	~20%	<0.03%	~70%
Dimension	~300 nm	~3 μm	~10 μm	~2 μm
Propagation loss	3 dB/cm	0.25 dB/cm	0.3 dB/cm	1.5 dB/cm
Coupling loss	7 dB	<7 dB	0.5 dB	3 dB

While different schemes have their own merits and shortcomings, reciprocal benefits can be obtained from integration of them. There was a hybrid-waveguide-structure reported that consists of III-V (AlGaInAs) quantum wells bonded to a silicon waveguide. Based on that, the evanescent laser [12], amplifier [13] and waveguide photodetector [14] were developed. Yariv et al. proposed another Si/III-V hybrid structure to realize lasers, amplifiers and modulators based on supermode theory [15]. Work was reported on preliminary results of As_2S_3 on Ti: $LiNbO_3$ hybrid waveguide devices [16, 17]. Besides, silicon-organic hybrid integration was also demonstrated to overcome the free carrier generation of silicon [7] and to enhance its optical nonlinearity [8].

A directional coupler is the simplest functional device to couple light by transferring energy between two adjacent waveguides. However, in practice its coupling efficiency can be fairly low due to the phase mismatch of waveguides and small tolerance to fabrication errors. Alternatively grating couplers and taper couplers are used.

In [18], a grating assisted waveguide coupler is proposed to couple light: the guided mode is converted into a radiation field first, and then back to a guided mode of another waveguide. Considering the directionality of light coupling in gratings, two waveguides are stacked vertically; In that case, complicated fabrication process is required to actually make it. The experimental work has not been published yet, and mostly gratings couplers are applied as an intermediate means to improve light coupling from single mode fibers to the waveguides [19, 20].

Taper couplers, on the other side, are generally preferred owing to its simplicity in design and fabrication. Despite diverse forms, the general taper coupler is composed of two parallel waveguides placed in close proximity: one is uniform whereas at one end of the other one, the width is gradually varied. The change is so slow that coupling into radiation modes can be neglected. During the light propagation in the taper, the mode is transformed gradually from one waveguide into another. Although the principle is intuitively quite simple, the design in most cases is conservative because of the lack of precise modeling guidelines and accurate modeling tools [21].

Therefore, the main purpose of this dissertation work is to study arsenic trisulfide (As_2S_3) waveguide devices on the substrate of lithium niobate ($LiNbO_3$) for integrated trace gas detection system, from design to fabrication and to characterization. They are low-loss As_2S_3 waveguides, polarization converters using titanium diffused waveguides (Ti: $LiNbO_3$) and As_2S_3-Ti: $LiNbO_3$ taper couplers.

1.2. Previous work

1.2.1. As_2S_3 waveguides and polarization converters on Ti: $LiNbO_3$

In the near infrared region (1550 nm), Ruan et al. have made chalcogenide waveguides with the propagation loss as low as 0.25 dB/cm by dry etching [22]. On the top of Ti: $LiNbO_3$ structure, As_2S_3 waveguides of low propagation loss (0.20 dB/cm) was achieved [23]. Fabrication of lower than 0.5 dB/cm chalcogenide waveguides through Si-CMOS-compatible lift-off technology was reported by Hu et al [24]. Other fabrication methods such as photosensitive laser beam writing [7], helium ion implantation [7], and hot embossing [25] were also investigated. Based on that, there are applications such as sampled Bragg gratings [26] and studies on nonlinearity such as pulsed nonlinear spectral broadening [27] and wavelength conversion via cross phase modulation [28].

In contrast to the ongoing fruitful research on optical waveguides in the near infrared, much less attention is paid to the field of mid infrared. Up to now there is only a little work that has been reported, and some of them involve only theoretical study and computer simulation [29]. To our best knowledge, the first experimental result was reported by Nicolas Ho et al. It is a channel waveguide that was made by the photo-darkening effect via laser writing in As_2Se_3 [30]. The best propagation loss is 0.5 ±0.1 dB/cm for TE and 1.1 ±0.1 dB/cm for TM at the wavelength of 8.4 μm. The coupling efficiency is only 20% due to a lack of optimization of mode mismatching. The core-to-cladding refractive index contrast is estimated to be 0.04, which is low for making compact structures. Besides that, solution-cast As_2S_3 waveguides with the propagation

loss of 9.47 dB/cm at 4.8 μm was reported [31]. They were made by dissolving As_2S_3 into propylamine solvent, molding it with polydimethylsiloxane (PDMS) and evaporating the solvent. The waveguides were 10-50 μm high and 20-80 μm wide, on a GaAs substrate with a 2 μm thick SiO_2. The coupling loss is 16.4 dB high, due to the air-As_2S_3 reflections and rough cleave face. From the above results, we can see that they are kind of at the preliminary stage of mid IR waveguide study and there is large room for improvement. We should be able to make better waveguides by reducing the propagation loss and coupling loss.

Although titanium diffused waveguides and related electro-optical devices have been studied extensively since 1980, most of the work was done around the wavelength of 1.5 μm. For mid IR, as regard to electro-optical devices using Ti: $LiNbO_3$, Mach-Zehnder interferometer based on titanium diffused waveguides on $LiNbO_3$ working at the wavelength of 2.6 μm was demonstrated, with the extinction ratio as high as ~30 dB and V_π ~14 V for the extraordinary mode [32]. However, as an essential function that gives us the controllability of light polarization, a polarization converter in this wavelength range has not been reported yet.

1.2.2. As_2S_3-Ti: $LiNbO_3$ mode couplers

A lot of theoretical study was carried out to investigate taper couplers, and different approaches were developed. Lee et al. proposed an equivalent waveguide concept employing a conformal mapping method, which was combined with the Beam Propagation Method (BPM) to conduct analysis [33]. In [21], tapered waveguides were

analyzed by considering the whole taper as a succession of short linear taper fragments and modeling each of them using a two-dimensional BPM that solves directly the Helmholtz equation.

However, most of the early work focused on correcting simulation methods to improve the accuracy, and the underlying physical mechanism governing the power transfer was not described [34]. Therefore few guidelines can be found for designers. It is until recently, more and more researchers began to look into taper couplers from the angle of local modes, i. e. supermodes. In [34], Xia et al. defined and distinguished between the resonant coupling and adiabatic coupling from the view of supermode: the co-directional coupler is a resonant coupler, in which optical power is split equally between the fundamental supermode (even mode) and the first-order supermode (odd mode), and the beating between these two modes transfers the light from one waveguide to another; in adiabatic couplers, the power is maintained in the fundamental mode, and it is spatially transferred from one waveguide to another [34]. Resonant couplers are compact and simple but highly sensitive to unavoidable variations during fabrication [34]. Adiabatic couplers, on the contrary, don't require the exact control of taper length and gap, but need longer length [35]. Sun et al. conducted a series of studies on the behavior of supermodes in adiabatic couplers [15, 35] and found that the longer the taper is, the smaller the amount of power is coupled into the higher order mode. A mathematical expression of the shortest adiabatic tapers is derived in [35].

As such theoretical work contributed a lot to our understanding of taper couplers, the study on issues of practical application and modeling is still lacking. In practice, we

often need to balance the taper length and the coupling efficiency, since we may not have sufficient space to fulfill the adiabatic condition, and we may want certain coupling efficiency that is not necessarily 100%. Mach-Zehnder interference filters, for example, typically use 3 dB couplers. Moreover, the materials and structures used may limit or affect the coupling. Thus, there are a lot of efficient but non-adiabatic taper couplers desired in practice.

In published papers most simulations were conducted based on beam propagation method (BPM) [36]. BPM calculates the electromagnetic fields during light propagation process and gives distributions of electric or magnetic fields, and so is the distribution of energy. It is highly accurate as long as certain assumptions are met. However, limited knowledge of underlying mechanisms can be obtained from the simulation process, so it is widely used as a means of examining the designed taper coupler instead of guiding design at the first place. Alternatively, the modeling of taper couplers can be based on the concept of modes using the coupled mode theory, which can provide insights to the mode evolvement in the coupler and thus provide immediate guidelines for design.

Therefore, the first step of this study is to develop a new modeling method of taper couplers based on the coupled mode and the supermode theory, and then apply it to analyze and design practical taper couplers for As_2S_3-Ti: $LiNbO_3$ hybrid waveguide system, followed by the fabrication and characterization.

1.3. Organization of the dissertation

After the introduction in Chapter I, the theories of electromagnetics, optical waveguides, coupled mode theory and polarization conversion induced by electro-optical effects, are briefly reviewed in Chapter II. They are the theoretical foundations to the study carried out in this dissertation work.

In Chapter III, after a high-level introduction of the general design process, the design of low-loss, single mode, chalcogenide glass waveguides on lithium niobate substrate based on those theoretical tools is first discussed, followed by that of integrated polarization converters on Ti: $LiNbO_3$. Next, the work is presented of the investigation on applying supermode theory to the efficient taper design for coupling light from Ti: $LiNbO_3$ to As_2S_3 waveguides, from both theoretical and practical aspects. The modeling method is first developed and the simulation aided design is then conducted.

In Chapter IV, the fabrication of the As_2S_3 waveguides and integrated Ti: $LiNbO_3$ polarization converters are introduced. The process development is explained in response to two questions: why do I choose the particular technology for certain processing steps and how to optimize the operation parameters to get the best result. Due to limitation of our facilities in making ultra-fine patterns (smaller than 1 μm), the photolithography of As_2S_3- Ti: $LiNbO_3$ taper coupler is done at Penn State University (PSU), which is also talked about briefly.

In Chapter V, the experimental results on fabricated waveguides and devices are presented, followed by the detailed discussion and analysis. Details of the measurement

setup are talked about as necessary. Then the dissertation is concluded with a brief discussion on future work in Chapter VI.

CHAPTER II

THEORETICAL REVIEW

2.1. Electromagnetic theory

Electromagnetic phenomena can be elegantly described by the classic electromagnetism (classical electrodynamics) theory if quantum effects are negligible. The electromagnetic radiation, including its excitation, propagation and interaction with media are governed by Maxwell's equations. Scottish physicist and mathematician James Clerk Maxwell published them in a four-part paper "On Physical Lines of Force" between 1861 and 1862 [37]. Maxwell's equations in differential form are shown in equation (2.1) to (2.4).

$$\nabla \cdot \boldsymbol{E} = \frac{\rho}{\varepsilon_0} \tag{2.1}$$

$$\nabla \cdot \boldsymbol{B} = 0 \tag{2.2}$$

$$\nabla \times \boldsymbol{E} = -\frac{\delta \boldsymbol{B}}{\delta t} \tag{2.3}$$

$$\nabla \cdot \boldsymbol{B} = \mu_0 \boldsymbol{J} + \mu_0 \varepsilon_0 \frac{\delta \boldsymbol{E}}{\delta t} \tag{2.4}$$

where $\boldsymbol{E}$ is the electric filed, $\boldsymbol{B}$ is magnetic field. ε_0 is permittivity and μ_0 the permeability of free space, also called the electric and magnetic constant respectively. ρ is the total free charge density. $\boldsymbol{J}$ is the total current density vector**.**

Of the four equations, the first two of them, the equation (2.1) and equation (2.2) are Gauss's law and Gauss's law for magnetism, describing how the fields emanate from

charges. Equations, (2.3) and (2.4) describe how the fields 'circulate' around their respective sources; the electric field 'circulates' around time varying magnetic fields in Faraday's law, while the magnetic field 'circulates' around electric currents and time varying electric field in Ampere's law with Maxwell's correction [37] .

Two auxiliary variables are introduced to represent the interactions of electric and magnetic fields and the media: The electric displacement field $\boldsymbol{D}$ and magnetic field (also known as magnetic flux density) $\boldsymbol{B}$, which are related to the electric field $\boldsymbol{E}$ and magnetic field $\boldsymbol{H}$ by the constitutive relations (2.5) and (2.6)

$$\boldsymbol{D} = \varepsilon_0 \boldsymbol{E} + \boldsymbol{P} \tag{2.5}$$

$$\boldsymbol{B} = \mu_0 (\boldsymbol{H} + \boldsymbol{M}) \tag{2.6}$$

where $\boldsymbol{P}$ and $\boldsymbol{M}$ are polarization and magnetization respectively.

And in conductive materials, we have Ohm's law:

$$\boldsymbol{J} = \sigma \boldsymbol{E} \tag{2.7}$$

In a vacuum, where no charges and no currents exist, those equations lead directly to $\boldsymbol{E}$ and $\boldsymbol{B}$ satisfying the Wave Equations:

$$\nabla^2 \boldsymbol{E} - \frac{1}{c^2} \frac{\partial^2 \boldsymbol{E}}{\partial t^2} = 0 \tag{2.8}$$

$$\nabla^2 \boldsymbol{B} - \frac{1}{c^2} \frac{\partial^2 \boldsymbol{B}}{\partial t^2} = 0 \tag{2.9}$$

where c is the speed of light in vacuum, which is 2.99794×10^8 m/s,

$$c = \frac{1}{\sqrt{\varepsilon_0 \mu_0}} \tag{2.10}$$

In the medium, c is substituted by the velocity of light in it. And such property of the medium is characterized by the refractive index n and the relative permittivity ε_r.

$$n = \frac{c}{v} = \frac{\sqrt{\varepsilon\mu}}{\sqrt{\varepsilon_0\mu_0}} = \sqrt{\varepsilon_r} \tag{2.11}$$

The solutions of the wave equation include all kinds of waves. Among them, the plane wave (2.12), spherical wave (2.13) and cylindrical wave (2.14) are the widely used in the following form:

$$\boldsymbol{E} = \boldsymbol{A}\exp[i(\boldsymbol{k}\cdot\boldsymbol{r} - \omega t)] \tag{2.12}$$

$$E = \frac{A_1}{r}\exp[i(kr - \omega t)] \tag{2.13}$$

$$E = \frac{A_1}{\sqrt{r}}\exp[i(kr - \omega t)] \tag{2.14}$$

where k is called the wave number, which is related to the wavelength λ by:

$$k = \frac{2\pi}{\lambda} \tag{2.15}$$

The Poynting vector is defined as the energy transported through a unit area that is perpendicular to the wave propagation direction in a unit time:

$$\boldsymbol{S} = \frac{1}{\mu}\boldsymbol{E}\times\boldsymbol{B} \tag{2.16}$$

The light absorption by the medium can be described by introducing a complex refractive index,

$$\tilde{n} = n + i\kappa \tag{2.17}$$

And then the intensity of light during propagation in the medium follows the Beer–Lambert law:

$$I = \boldsymbol{E} \cdot \boldsymbol{E}^* = |\boldsymbol{A}|^2 \exp\left(-\frac{2n\kappa\omega}{c} z\right) = I_0 \exp(-\bar{\alpha} z) \tag{2.18}$$

where $\bar{\alpha}$ is called the absorption coefficient.

Dispersion is another characteristic of the light-material interaction, which means the refractive index of the medium changes as the wavelength of incident light varies. Cauchy summarized an empirical formula in 1836 to describe the material dispersion:

$$n = a + \frac{b}{\lambda^2} + \frac{c}{\lambda^4} \tag{2.19}$$

where a, b and c are the constants that are determined by the material.

When light propagation from one medium to another, the boundary conditions need to be considered:

$$\begin{cases} \boldsymbol{n} \cdot (\boldsymbol{B}_1 - \boldsymbol{B}_2) = 0 \\ \boldsymbol{n} \cdot (\boldsymbol{D}_1 - \boldsymbol{D}_2) = 0 \\ \boldsymbol{n} \times (\boldsymbol{E}_1 - \boldsymbol{E}_2) = 0 \\ \boldsymbol{n} \times (\boldsymbol{H}_1 - \boldsymbol{H}_2) = 0 \end{cases} \tag{2.20}$$

Using the boundary conditions, the phenomenon of refraction and reflection (of plane wave) can be studied.

Assume $\boldsymbol{E_1} = \boldsymbol{A_1} \exp[i(\boldsymbol{k_1} \cdot \boldsymbol{r} - \omega_1 t)]$ is the incident wave, while $\boldsymbol{E_1'} = \boldsymbol{A_1'} \exp[i(\boldsymbol{k_1'} \cdot \boldsymbol{r} - \omega_1' t)]$ and $\boldsymbol{E_2} = \boldsymbol{A_2} \exp[i(\boldsymbol{k_2} \cdot \boldsymbol{r} - \omega_2 t)]$ are the reflected wave and refracted wave respectively, as Fig. 5 shows.

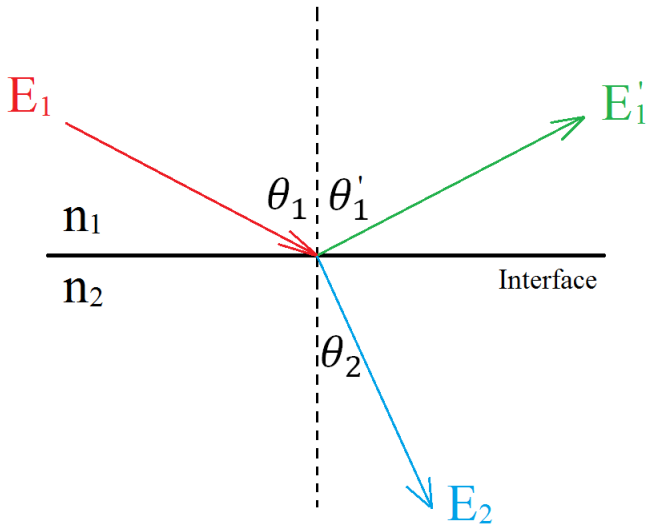

Fig. 5. Reflection and refraction.

The following relationship can be obtained:

$$\boldsymbol{k_1} \cdot \boldsymbol{r} = \boldsymbol{k_1'} \cdot \boldsymbol{r} = \boldsymbol{k_2} \cdot \boldsymbol{r} \tag{2.21}$$

Transform it using the incident and refraction angles, we have Snell's Law:

$$n_1 \sin\theta_1 = n_2 \sin\theta_2 \tag{2.22}$$

As light is incident on the interface from the large refractive index medium to small refractive index medium ($n_1 > n_2$), where the incident angle is larger than a certain value ($\theta > \theta_c$, θ_c *is* critical angle), $\sin\theta_2$ becomes larger than 1, which is meaningless. In practice, there will be no refracted light and all energy is reflected back into the large refractive index medium. That is called total internal reflection (Fig. 6 from Internet), and the critical angle can be obtained:

$$\theta_c = \sin^{-1}(\frac{n_2}{n_1}) \tag{2.23}$$

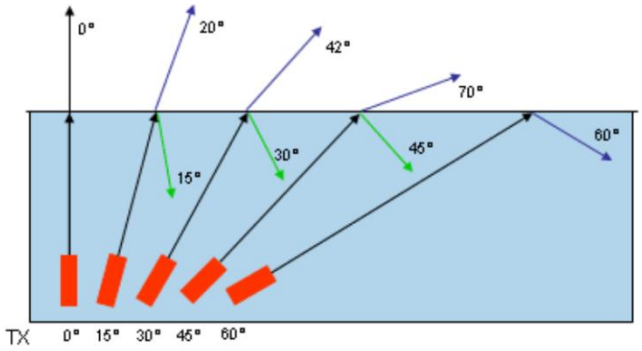

Fig. 6. Total internal reflection.

Integrated waveguides, serving as an optical interconnection, guide light by total internal reflection.

2.2. Optical waveguides

The purpose of optical waveguides is to construct a structure having a refractive index difference to confine the light based on the principle of total internal reflection. Depending on the types of refractive index change, optical waveguides can be subcategorized into step-index waveguides and graded-index waveguides. The previous structure for illustrating total internal reflection is a step-index waveguide that is formed by a high refractive index material and a low refractive index ambient. The boundary of waveguide, that is, the interface experiences an abrupt change in refractive index. If the refractive index exhibits a gradually decreasing profile from the center to the periphery, it is a graded-index waveguides.

According to the configuration of the confinement structure, the waveguides can be classified into planar slab waveguide (two-dimensional confinement) and three-dimensional waveguide, rectangular waveguide for example.

2.2.1. Two-dimensional slab waveguides

Although not widely used in practice, the planar slab waveguide is the simplest waveguide that provides insight into more complicated waveguides. The configuration is shown in Fig. 7 below.

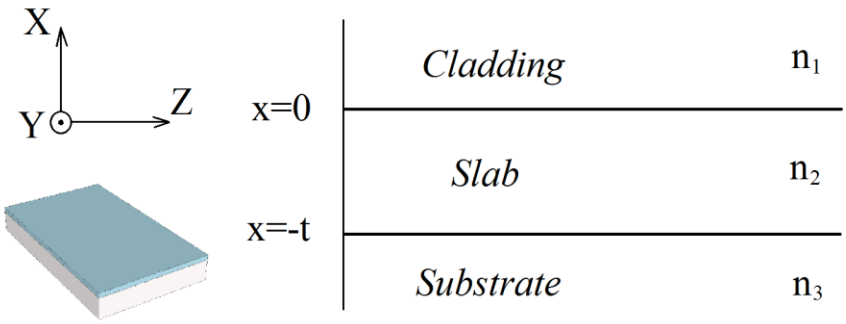

Fig. 7. Structure of slab waveguide.

If the polarization of the electric field is parallel to the slab, it is called transverse electric (TE) mode while if the magnetic field is parallel to the slab, it is called transverse magnetic (TM) mode.

Consider the plane wave solution in equation (2.12), the spatial and temporal parts can be separated. The temporal part is a common factor and we are interested in the spatial part only.

Substitute it into wave equation,

$$\nabla^2\tilde{E}(\tilde{r}) + k_0^2 n^2 \tilde{E}(\tilde{r}) = 0 \tag{2.24}$$

Then we can separate spatially x, y and z. Assuming propagation along z axis, the complex amplitude can be written as $\tilde{E}(\tilde{r}) = \tilde{E}(x,y,z) = \tilde{E}(x,y)e^{-j\beta z}$. And since for the planar slab waveguide, there is no restriction in y direction, $\tilde{E}(x,y) = \tilde{E}(x)$.

Assume the light is TE polarized, $\tilde{E}(x) = E_y(x)$,

$$\frac{d^2E_y(x)}{dx^2} + (k_0^2 n^2 - \beta^2)E_y(x) = 0 \tag{2.25}$$

Solve the above equation, we have the following solution

$$E_y(x) = \begin{cases} C'e^{-qx}, & x > 0 \\ C'\left[\cos(hx) - \dfrac{q}{h}\sin(hx)\right], & -t \le x \le 0 \\ C'\left[\cos(ht) - \dfrac{q}{h}\sin(ht)\right]e^{p(x+t)}, & x < -t \end{cases} \tag{2.26}$$

where

$$C' = 2h\left[\frac{\omega\mu P}{|\beta|(q^2+h^2)\left(t+\frac{1}{q}+\frac{1}{h}\right)}\right]^{1/2} \tag{2.27}$$

and

$$\begin{cases} q = \sqrt{\beta^2 - k_0^2 n_1^2} \\ h = \sqrt{k_0^2 n_2^2 - \beta^2} \\ p = \sqrt{\beta^2 - k_0^2 n_3^2} \end{cases} \tag{2.28}$$

And the relationship between those parameters is known as the characteristic equation (eigen-value equation):

$$\tan(ht) = \frac{q+p}{h - \frac{q \cdot p}{h}} \tag{2.29}$$

Numerical computation or graphical methods can be used to solve the characteristic equation (2.29), and h, q and p can be found. Depending on values of n_1, n_2, n_3 and t, λ, there could be more than one h. Each h value corresponds to a solution, which is called a mode, denoted by the subscript m.

For TM polarization, the solution is

$$H_y(x) = \begin{cases} -A' e^{-qx}, & x > 0 \\ A' \left[-\frac{h}{q}\cos(hx) + \sin(hx) \right], & -t \le x \le 0 \\ -A' \left[\frac{h}{q}\cos(ht) + \sin(ht) \right] e^{p(x+t)}, & x < -t \end{cases} \tag{2.30}$$

where

$$A' = 2\sqrt{\frac{\omega \varepsilon_0 P}{\beta t'}} \tag{2.31}$$

and

$$t' = \frac{\left(\frac{n_2^2}{n_1^2} q\right)^2 + h^2}{\left(\frac{n_2^2}{n_1^2} q\right)^2} \left[\frac{t}{n_2^2} + \frac{q^2 + h^2}{\left(\frac{n_2^2}{n_1^2} q\right)^2 + h^2} \cdot \frac{1}{n_1^2 q} + \frac{p^2 + h^2}{\left(\frac{n_2^2}{n_3^2} p\right)^2 + h^2} \cdot \frac{1}{n_3^2 p} \right] \tag{2.32}$$

The characteristic equation is

$$\tan(ht) = \frac{\left[\frac{n_2^2}{n_3^2}p + \frac{n_2^2}{n_1^2}q\right]}{h - \left(\frac{n_2^2}{n_1 n_3}\right)^2 \left(\frac{p \cdot q}{h}\right)} \tag{2.33}$$

Since the concept of mode is of paramount importance to wave-guiding optics, it is helpful to further our understanding. For example, it can be understood by picturing the light as directional rays between the two slabs. While moving towards the z direction, they are reflected back and forth along the boundaries according to total internal reflection, forming a "Z" shaped paths, as Fig. 8 shows. As long as the incident angle is larger than the critical angle, the light can propagate. But for some rays with certain incident angles where the phase variation over one period of reflections is 2π, and stable standing waves will be formed in the x direction, therefore the stable intensity patterns result. They are the modes of the waveguide.

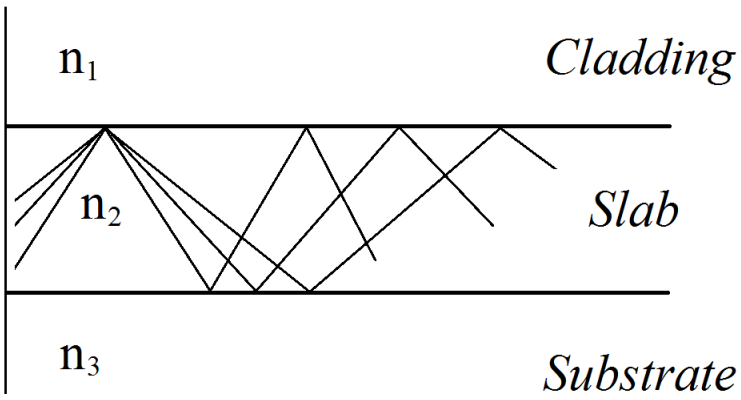

Fig. 8. Light paths in a slab waveguide.

Strict theoretical analysis requires taking into account of the phase change δ at the reflection point on both upper (δ_{upperI}) and lower (δ_{II}) boundaries, and the mode equation is,

$$\delta = 2nk_0h\cos\theta_i + \delta_{upperI} + \delta_{II} = 2m\pi \quad (m = 0,1,2,\dots) \tag{2.34}$$

In equation (2.34) the phase change at interfaces δ_{upperI} and δ_{II} can be calculated by

$$\begin{cases} \tan\dfrac{\delta}{2} = -\dfrac{\left[\sin^2\theta_i - \left(\dfrac{n_0}{n}\right)^2\right]^{1/2}}{\cos\theta_i} \; for\ TE \\ \tan\dfrac{\delta}{2} = -\left(\dfrac{n_0}{n}\right)^2 \dfrac{\left[\sin^2\theta_i - \left(\dfrac{n_0}{n}\right)^2\right]^{1/2}}{\cos\theta_i} \; for\ TM \end{cases} \tag{2.35}$$

In [2], Yariv introduces another perspective, a more wave-optic way, to look at the formation of modes mentioned above: because the refractive index of the core is higher than the surroundings, the higher index of refraction in the core of the guiding structure has an effect similar to that of a converging lens. Under the appropriate conditions, this converging effect due to the higher core index may cancel out exactly the spreading due to diffraction. When this happens, a guided mode is supported by the dielectric structure.

2.2.2. Three-dimensional waveguides

Without the restriction in y direction, the energy of light will be easily lost during propagation. Therefore, in practice most of optical waveguides confine light also in the y direction, which are known as three-dimensional (3D) waveguides.

There are generally three types of 3D waveguides: channel (rectangular) waveguides, rib waveguides and graded-index waveguides such as diffused waveguides, shown in Fig. 9.

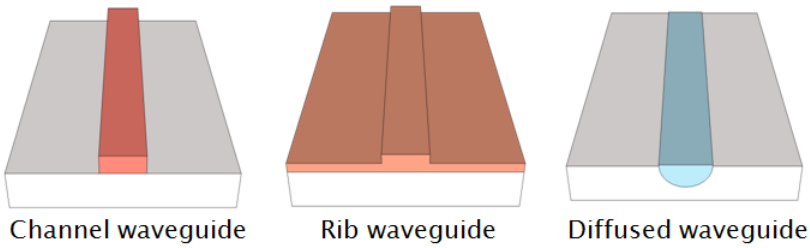

Fig. 9. Three types of three-dimensional waveguides.

Channel waveguides, due to high mode confinement, are capable of realizing compact structures, such as sharp bends. Rib waveguides have less confinement in the transverse direction, and thus generally have a larger mode size than channel waveguides. Diffused waveguides, on the other side, are typical graded-index waveguides. They have low mode confinement and therefore have very large mode size. As a result, they are suitable for alignment with single mode fibers. And since the wave-guiding structure is diffused inside the substrate and the optical mode is below the surface, they are less susceptible to surface contamination.

A typical channel waveguide, as Fig. 10 shows, consists of a substrate, a waveguide core and a cladding. In order to utilize total internal reflection, the refractive index of the core is larger than that of substrate and cladding. The difference of refractive indices is characterized by the index contrast, defined as

$$\Delta = 2\frac{n_{core} - n_{substrate}}{n_{core} + n_{substrate}} \tag{2.36}$$

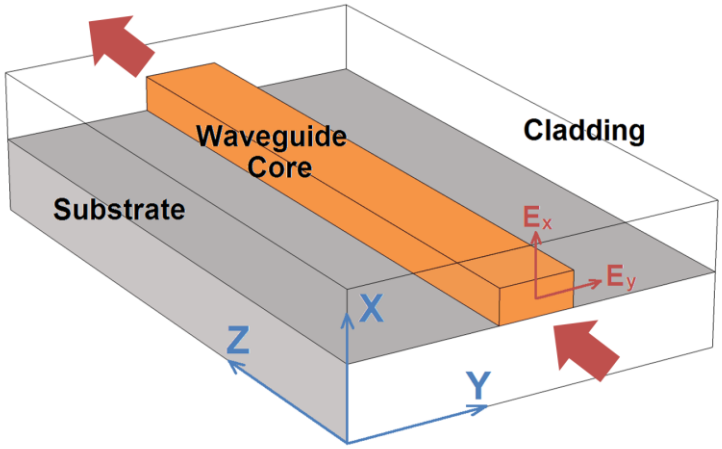

Fig. 10. Structure of channel waveguide.

Unlike microwave rectangular waveguides with perfect conductor walls that can support pure TE and TM modes, 3D dielectric waveguides only support hybrid modes, which are polarized in both directions [4]. However, if the main electric field of a mode lies in the x direction, it is called TM-like mode, sometimes simply referred to as TM mode. Similarly, we also have TE-like modes in 3D waveguides.

Generally, numerical computation needs to be carried out in order to obtain the rigorous solution. However, approximate analysis enable one to obtain an analytical solution in a closed form: if the guided mode is far from the cutoff condition, and the width of the waveguide is larger than the height, Marcatili's method and the effective index method are useful [4].

The cross-section of the waveguide is divided into nine squares, as shown in Fig. 11. Marcatilis' method treats electromagnetic fields in x and y directions separately, and then combines them together to obtain the approximate solution of the waveguide. The method ignores the fields in four shaded areas, so that it is considered good only for well-guided waveguides. The effective index method improves Marcatilis's method by taking those four shaded squares into account, and becomes an accurate, widely used approach. It first calculates the fields in one direction (x direction for example), then treats those three squares as a single square by using an effective index, and then solves the structure, which is equivalently a slab waveguide, in the y direction. In other words, the principle of these analytical methods is to convert the problem of a 3D channel waveguide into that of two 2D planar waveguides.

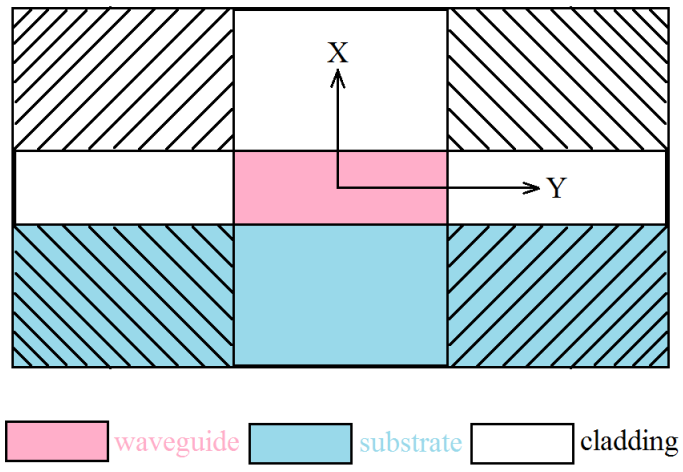

Fig. 11. Illustration of Marcatilis' method.

Besides channel waveguides, the effective index method can also be applied to analyze rib waveguides. However, for more complicated waveguide structures or more strict accuracy requirements, numerical programs need to be employed and some commercial waveguide modeling software is available, such as R-soft, FIMMWAVE and OptiSystem.

2.2.3. Characteristics of optical waveguides

For an optical waveguide, how many TE and TM modes it can support is a characteristic of the waveguide itself, which can be calculated using above mentioned methods. But what mode (or modes) propagates in it is affected by the excitation condition. In the ideal case, once a certain mode is excited, it will keep the same cross-sectional profile during propagation.

There are various methods for mode excitation, or mode coupling from exterior source into the waveguide: butt coupling and end-fire coupling that are transverse means and surface means such as prism and grating. Transverse means are generally intuitive, require less equipment, and are highly efficient. In butt coupling, a fiber or another piece of waveguide is placed next to the waveguide to be coupled, and directly let the output of the former inject into the input of the latter. The coupling efficiency can be predicted by the equation (2.37). We can see that it can be very high if the modes are identical. And if that is not the case, the coupling loss will include Fresnel loss and the mode mismatching loss. In the end-fire coupling scheme, a lens is used to focus the free-space light into the waveguide. The diffraction limit poses a limit to the coupling efficiency.

$$\eta = \frac{4\beta_i\beta_t}{(\beta_i+\beta_t)^2}\frac{\left[\int_{-\infty}^{+\infty} E_i(x)E_t^*(x)dx\right]^2}{\left[\int_{-\infty}^{+\infty} E_i(x)E_i^*(x)dx\right]\left[\int_{-\infty}^{+\infty} E_t(x)E_t^*(x)dx\right]} \tag{2.37}$$

Different modes have slightly different propagation speed, which causes pulse broadening in high speed transmission. If the waveguide only allows a fundamental mode, then there won't be such problem, it is called a single mode waveguide. And it's preferred in most cases. The size is usually small, since the larger dimension of the waveguide, the more propagation modes it can support.

An important criterion to measure a waveguide is attenuation, also known as loss. There are two types of loss that are widely used: insertion loss and propagation loss. Propagation loss, also known as the propagation attenuation, is defined by the signal attenuation (dB) per unit length [2].

$$\propto = \frac{10}{L} log_{10}\left[\frac{P(L)}{P(0)}\right] \tag{2.38}$$

However, it is difficult to know the power at a certain location of the waveguide, such as $P(0)$ and $P(L)$. Therefore, insertion loss is often used. Insertion loss is the loss of signal power resulting from the insertion of a waveguide in an optical light path and is usually expressed in decibels (dB) also. If the power transmitted to the load before insertion is P_T and the power received by the load after insertion is P_R, then the insertion loss in dB is given by [38],

$$Insertion\ loss = 10log_{10}\left[\frac{P_T}{P_R}\right] \tag{2.39}$$

The insertion loss is composed of the propagation loss and the coupling loss at the end of input and output. Therefore, we can derive the propagation loss from the insertion loss if the coupling loss is known or can be canceled out. In a word, the insertion loss measures the total performance of the waveguide as a device, including coupling loss and propagation loss, while propagation loss characterizes the waveguide itself.

Propagation losses come from the intrinsic material absorption and Rayleigh scattering, as well as from extrinsic loss, such as mode conversion loss due to imperfections, such as surface corrugation and bends. Because in sharp bends, the mode deviates from the center of the waveguide and a certain amount of power may leak into the substrate or cladding. The sharper the waveguide bends, the more power it leaks.

Rough sidewall and surface due to fabrication defects, can cause light to scatter, which is a major factor to propagation loss. The smoothness of end-facets affects light coupling from the exterior input to the waveguide, so it determines the coupling loss primarily.

2.3. Coupled mode theory

From the physical perspective, modes are a set of pre-determined electromagnetic field structures that keep stable during light propagation in the optical waveguide. They can be identified from intensity patterns formed on the cross-sectional plane in the waveguide. Mathematically, they are eigen-vectors, which form a set of orthogonal basis of the solution space to the wave equations of the waveguide. So

generally they are independent and do not have interactions. Once excited, each mode carries power and propagates along the guide independently of the presence of other modes. However, if there is a disturbance (perturbation) in the waveguide, such as surface corrugations, they may become coupled and energy may transfer from one to another. Coupled mode theory is therefore developed to study such phenomenon.

Assume in a piece of continuous ideal dielectric waveguide, TE polarized light $\tilde{E}(\tilde{r},t) = E_y(\tilde{r},t)\hat{a}_y$ is propagating, so that it satisfies the wave equation

$$\nabla^2 E_y(\tilde{r},t) = \mu \frac{\partial^2}{\partial t^2} D_y(\tilde{r},t) \tag{2.40}$$

The electric displacement is caused by the electric field in the medium:

$$D_y(\tilde{r},t) = \varepsilon(\tilde{r}) E_y(\tilde{r},t) \tag{2.41}$$

If a disturbance occurs, that is, the dielectric medium is altered, the effect can be represented by the perturbation $P_{pert}(\tilde{r},t)$:

$$D_y(\tilde{r},t) = \varepsilon(\tilde{r}) E_y(\tilde{r},t) + P_{pert}(\tilde{r},t) \tag{2.42}$$

Substitute it into the wave equation (2.40),

$$\nabla^2 E_y(\tilde{r},t) - \mu\varepsilon(\tilde{r}) \frac{\partial^2 E_y(\tilde{r},t)}{\partial t^2} = \mu \frac{\partial^2}{\partial t^2} \left[P_{pert}(\tilde{r},t)\right]_y \tag{2.43}$$

Solve it using a two-step strategy: first ignore the perturbation and find the solution to the ideal case, and then assume a small perturbation and refine the solution, we have

$$\frac{dA_s^-}{dz} e^{j(\omega t+\beta_s z)} - \frac{dA_s^+}{dz} e^{j(\omega t-\beta_s z)} - c.c = \frac{-j}{2\omega} \frac{\partial^2}{\partial t^2} \int_{-\infty}^{+\infty} \left[P_{pert}\right]_y \mathcal{E}_y^s(x) dx \tag{2.44}$$

If back reflection A_s^- can be neglected, which is true for most cases, we have

$$-\frac{dA^+(z)}{dz}e^{j(\omega t-\beta z)}-c.c=\frac{-j}{2\omega}\frac{\partial^2}{\partial t^2}\int_{-\infty}^{+\infty}P_{pert}(\tilde{r},t)\mathcal{E}(x,y)dx \tag{2.45}$$

To deliberately utilize the phenomenon of mode coupling, we need to design some device that can separate the modes. The co-directional coupler is the simplest case, illustrated in Fig. 12.

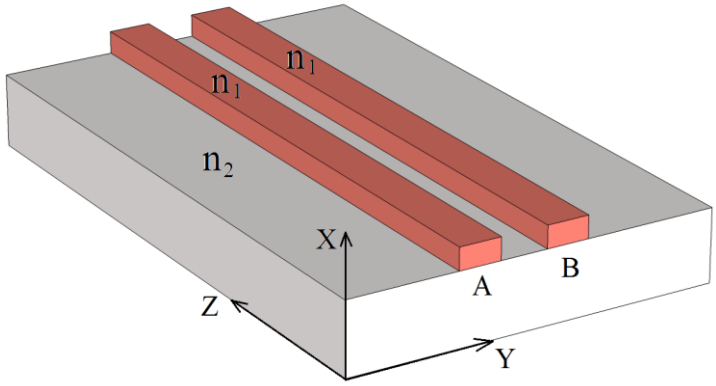

Fig. 12. Co-directional coupler.

The electric fields in two waveguides have the following form,

$$\tilde{E}_B(\tilde{r},t)=B\tilde{\mathcal{E}}_B(x,y)e^{j(\omega t-\beta_b z)} \tag{2.46}$$

$$\tilde{E}_A(\tilde{r},t)=A\tilde{\mathcal{E}}_A(x,y)e^{j(\omega t-\beta_a z)} \tag{2.47}$$

And the mode coupling can be re-written as

$$\frac{dA^+}{dz}e^{j(\omega t-\beta_a z)}+c.c=\frac{j}{2\omega}\frac{\partial^2}{\partial t^2}\int_{-\infty}^{+\infty}P_{pert}(\tilde{r},t)\mathcal{E}_A(x,y)dxdy \tag{2.48}$$

The perturbation is induced from the difference of the refractive index seen by waveguide A, with the presence of waveguide B and without it. That is,

$$\begin{aligned} P_{pert}(x,y,z,t) &= \varepsilon_0[n_1^2 - n_2^2]E_{By}(x,y,z,t) \\ &= \varepsilon_0[n_1^2(x,y) - n_2^2]\left[\frac{B^+(z)}{2}\mathcal{E}_{By}(x,y)e^{j(\omega t-\beta_b z)} + c.c\right] \end{aligned} \tag{2.49}$$

Re-arrange equation (2.48) by substitute in equation (2.49), we have

$$\begin{aligned} \frac{dA^+}{dz} = -jB(z)\Big\{\frac{\omega\varepsilon_0}{4}\int [n_1^2(x,y)_A \\ - n_2^2]\,\mathcal{E}_{By}(x,y)\mathcal{E}_{Ay}(x,y)dxdy\Big\}e^{j(\beta_a-\beta_b)z} \end{aligned} \tag{2.50}$$

Introduce κ as the coupling strength, so

$$\kappa = \frac{\omega\varepsilon_0}{4}\int [n_1^2(x,y)_A - n_2^2]\,\mathcal{E}_{By}(x,y)\mathcal{E}_{Ay}(x,y)dxdy \tag{2.51}$$

Then we have the coupled mode equations for the directional coupler

$$\begin{cases} \dfrac{dA(z)}{dz} = -j\kappa_{ab}B(z)e^{j(\beta_a-\beta_b)z} \\ \dfrac{dB(z)}{dz} = -j\kappa_{ba}A(z)e^{j(\beta_b-\beta_a)z} \end{cases} \tag{2.52}$$

For the lossless medium, the relationship in (2.53) is satisfied,

$$\kappa_{ab} = \kappa_{ba} = \kappa \tag{2.53}$$

If power is injected into waveguide A only, i. e., we have the following boundary condition:

$$\begin{cases} A(z=0) = A_0 \\ B(z=0) = 0 \end{cases} \tag{2.54}$$

If modes in waveguide A and waveguide B are phase matched, that is,

$$\Delta\beta = \beta_b - \beta_a = 0 \tag{2.55}$$

The solution of the coupled mode equations (2.52) is

$$\begin{cases} A(z) = A_0 \cos(\kappa z) \\ B(z) = -jA_0 \sin(\kappa z) \end{cases} \tag{2.56}$$

Translate into the form of intensity (power), and plot in Fig. 13

$$\begin{cases} \dfrac{P_a(z)}{P_a(z=0)} = \cos^2(\kappa z) \\ \dfrac{P_b(z)}{P_a(z=0)} = \sin^2(\kappa z) = 1 - \cos^2(\kappa z) \end{cases} \tag{2.57}$$

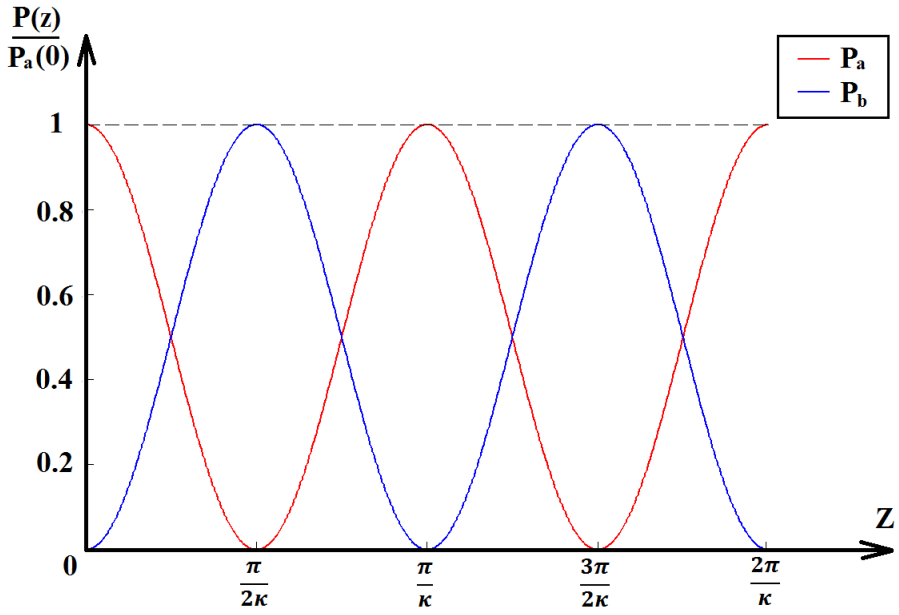

Fig. 13. Mode coupling in directional coupler (phase matched case).

From the graph, we can see that since we assume lossless, the sum of power in waveguide A and that in waveguide B equals to 1. However, because of the mode coupling between these two waveguides, the power oscillates back and forth as a result,

which can be used as the power splitter if the length is fixed at certain value. Therefore the co-directional coupler becomes a fundamental element whereas its improved counterparts can be used in plenty of applications. For that purpose, the matrix form is more convenient:

$$\begin{pmatrix} A(z) \\ B(z) \end{pmatrix} = \begin{pmatrix} \cos(\kappa z) & -j\sin(\kappa z) \\ -j\sin(\kappa z) & \cos(\kappa z) \end{pmatrix} \begin{pmatrix} A(z=0) = A_0 \\ B(z=0) = B_0 \end{pmatrix} \tag{2.58}$$

If modes in waveguide A and B are not phased matched, that is,

$$\Delta\beta = \beta_b - \beta_a \neq 0 \tag{2.59}$$

The solution becomes

$$\begin{cases} P_a(z) = P_a(0)\left[1 - \dfrac{\kappa^2}{\delta^2}\sin^2(\delta z)\right] \\ P_b(z) = P_a(0)\left[\dfrac{\kappa^2}{\delta^2}\sin^2(\delta z)\right] \end{cases} \tag{2.60}$$

where

$$\delta = \sqrt{\kappa^2 + (\Delta\beta/2)^2} \tag{2.61}$$

And the powers are plotted in Fig. 14.

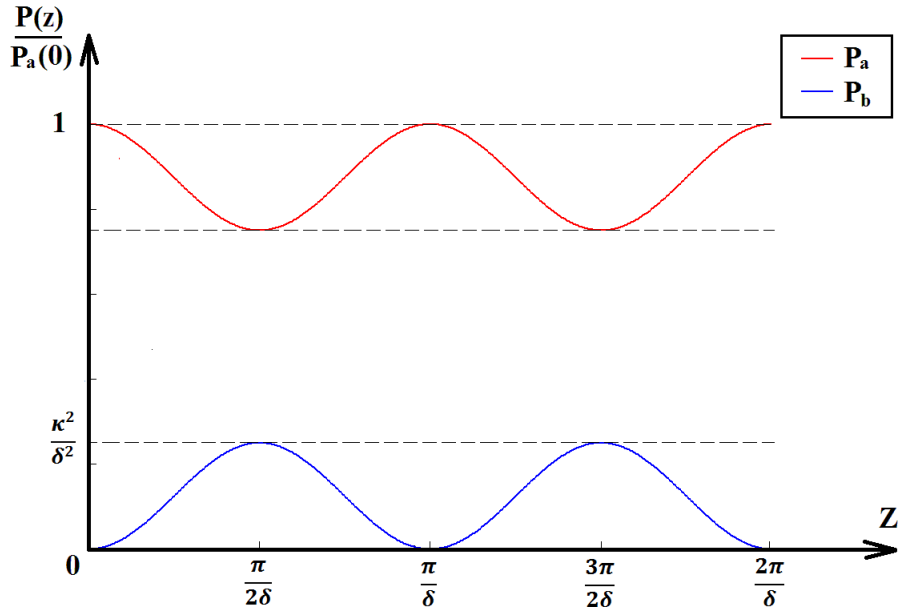

Fig. 14. Mode coupling in directional coupler (phase mismatched case).

2.4. Electro-optical effect

When an electric field is applied on a ferroelectric crystal, the refractive index of the crystal will change, which is called electro-optical effect. For crystals without inversion symmetry, such as $LiNbO_3$, the index varies linearly with the applied electric field, which is called the Pockels effect. In central-symmetrical crystals, the Pockels effect is absent and the induced index change is proportional the square of the applied electric field [4].

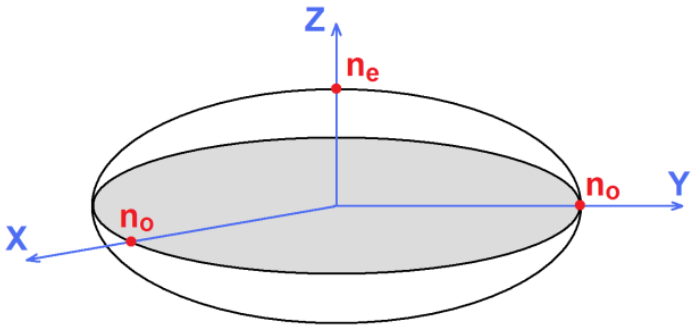

Fig. 15. Index ellipsoid of lithium niobate.

The electro-optical properties are observed in ferroelectric crystals. In those crystals, the refractive index is dependent on crystal structure such that they exhibit optical anisotropy, i. e. the refractive index changes when varying the propagation direction. An index ellipsoid is introduced for such anisotropic material to determine the refractive index (Fig. 15). When the principal axes of the index ellipsoid coincide with x, y and z, the ellipsoid can be expressed by

$$\frac{x^2}{n_x^2}+\frac{y^2}{n_y^2}+\frac{z^2}{n_z^2}=1 \tag{2.62}$$

or in terms of relative permittivity,

$$\frac{X^2}{\varepsilon_{11}}+\frac{Y^2}{\varepsilon_{22}}+\frac{Z^2}{\varepsilon_{33}}=1 \tag{2.63}$$

where $n_i^2=\varepsilon_{jj}$. Re-arrange it into to a standard form:

$$B_{11}X^2+B_{22}Y^2+B_{33}Z^2=1 \tag{2.64}$$

where $B=\frac{1}{\varepsilon_r}=\frac{1}{\varepsilon/\varepsilon_0}=\frac{1}{n^2}$.

When an electric field is applied, the index ellipsoid will be distorted: rotated and stretched along some directions. Then the equation of the index ellipsoid is described by the general equation:

$$B'_{11}X^2 + B'_{22}Y^2 + B'_{33}Z^2 + 2B'_{23}YZ + 2B'_{31}ZX + 2B'_{12}XY = 1 \tag{2.65}$$

Renaming the coefficients for convenience,

$$B'_1X^2 + B'_2Y^2 + B'_3Z^2 + 2B'_4YZ + 2B'_5ZX + 2B'_6XY = 1 \tag{2.66}$$

When compared to the coefficients of equation before applying the electric field,

$$\Delta B_i = B'_i - B_i \equiv \Delta\left(\frac{1}{n_i^2}\right) = \sum_{\substack{i=1,2,3 \\ j=1,2,\ldots,6}} r_{ij}\, E_j \tag{2.67}$$

and the change induced by the electric field can be described by a 6×3 tensor

$$\begin{pmatrix} \Delta\left(\frac{1}{n_1^2}\right) \\ \Delta\left(\frac{1}{n_2^2}\right) \\ \Delta\left(\frac{1}{n_3^2}\right) \\ \Delta\left(\frac{1}{n_4^2}\right) \\ \Delta\left(\frac{1}{n_5^2}\right) \\ \Delta\left(\frac{1}{n_6^2}\right) \end{pmatrix} = \begin{pmatrix} r_{11} & r_{12} & r_{13} \\ r_{21} & r_{22} & r_{23} \\ r_{31} & r_{32} & r_{33} \\ r_{41} & r_{42} & r_{43} \\ r_{51} & r_{52} & r_{53} \\ r_{61} & r_{62} & r_{63} \end{pmatrix} \begin{pmatrix} E_1 \\ E_2 \\ E_3 \end{pmatrix} \tag{2.68}$$

To be specific, for the first three terms,

$$B'_i \equiv \frac{1}{(n'_i)^2} = \left(B_i \equiv \frac{1}{n_i^2}\right) + \Delta\left(\frac{1}{n_i^2}\right) \text{ for } i = 1,2,3 \tag{2.69}$$

They suggest there are changes in the magnitude of refractive indices along principle axes. While, a rotation of the index ellipsoid is represented by the remaining three terms:

$$B_i' \equiv \frac{1}{(n_i')^2} = B_i = 0 + \Delta R_i \equiv \Delta\left(\frac{1}{n_i^2}\right) \text{ for } i = 4,5,6 \tag{2.70}$$

For example, the electro-optical tensor of $LiNbO_3$ (3m crystal class) is

$$r_{ij} = \begin{pmatrix} 0 & -r_{22} & r_{13} \\ 0 & r_{22} & r_{13} \\ 0 & 0 & r_{33} \\ 0 & r_{51} & 0 \\ r_{51} & 0 & 0 \\ -r_{22} & 0 & 0 \end{pmatrix} \tag{2.71}$$

While at the wavelength of 632.8 nm,

$$\begin{cases} r_{22} = 3.4 \times 10^{-12}\, m/V \\ r_{13} = 8.6 \times 10^{-12}\, m/V \\ r_{33} = 30.8 \times 10^{-12}\, m/V \\ r_{51} = 28 \times 10^{-12}\, m/V \end{cases} \tag{2.72}$$

Since

$$\sum_{j=1}^{3} r_{ij} E_j = \frac{-2\Delta n_i}{n_i^3} \tag{2.73}$$

$$\Delta n_i = -\frac{1}{2} n_i^3 \sum_{j=1}^{3} r_{ij} E_j \text{ for } i = 1,2,\ldots,6 \tag{2.74}$$

As a result of an applied electric field component E_j, the refractive indices are changed by Δn_i.

2.5. Polarization conversion

As mentioned above, B_i' $(i = 4,5,6)$ are the coefficients of cross terms YZ, ZX, XY in equation (2.66), which indicate a rotation of the principal axes of the index ellipsoid. If the input light is TM polarized, such rotation will cause polarizability along the TE direction. Provided that the phase matching condition is met, the TM mode will be gradually coupled to TE mode during the propagation (Fig. 16).

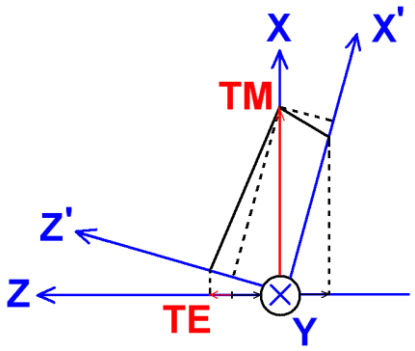

Fig. 16. Polarization conversion induced by rotation of index ellipsoid.

Assume the lithium niobate is configured in a y-cut, x-propagation manner, and an electric field is applied along y direction. The input is TM mode. According to the theory of electro-optics, we have

$$\delta\varepsilon_{23} = -n_e^2 n_o^2 r_{51} E_y^e \tag{2.75}$$

From the coupled mode equation (2.45),

$$\frac{dA^{TM}}{dx} e^{j(\omega t - \beta_{TM} x)} + c.c = \frac{-j}{2\omega}\frac{\partial^2}{\partial t^2}\int_{-\infty}^{+\infty} \left[P_{pert}\right]_z \varepsilon_y^{TM}(y)dy \tag{2.76}$$

where P_{pert} is a perturbation expressed by

$$\left[P_{pert}\right]_z = \varepsilon_o(\delta\varepsilon_{23})E_z^{TE}(y) = \varepsilon_o\left(-n_e^2 n_o^2 r_{51}E_y^e\right)E_z^{TE}(y) \tag{2.77}$$

Solve the wave equation for $H_z^{TM}(y)$, obtain $E_y^{TM}(y)$, and then substitute them into equation (2.76).

$$\begin{aligned}&\frac{dA^{TM}}{dx}e^{-j\beta_{TM}x}\\&=\frac{j}{2\omega}(j\omega)^2\left(-\varepsilon_o n_e^2 n_o^2 r_{51}E_y^e\right)\frac{B^{TE}}{2}\frac{\beta_{TM}}{\omega\varepsilon_o n_o^2}e^{-j\beta_{TE}x}\int_{-t}^{0}\varepsilon_z^{TE}(y)H_z^{TM}(y)dy\end{aligned} \tag{2.78}$$

For well guided modes, we have

$$E_z^{TE}(y) = \left(\frac{4\omega\mu}{t\beta_{TE}}\right)^{1/2}\sin\left(\frac{m\pi}{t}y\right) \tag{2.79}$$

$$H_z^{TM}(y) = \left(\frac{4\omega\varepsilon_o n_o^2}{t\beta_{TM}}\right)^{1/2}\sin\left(\frac{m\pi}{t}y\right) \tag{2.80}$$

Substitute them into equation (2.78), we have

$$\begin{cases}\dfrac{dA^{TM}(x)}{dx} = -j\kappa B^{TE}(x)e^{-j(\beta_{TE}-\beta_{TM})x}\\[2ex]\dfrac{dB^{TE}(x)}{dx} = -j\kappa A^{TM}(x)e^{-j(\beta_{TM}-\beta_{TE})x}\end{cases} \tag{2.81}$$

where

$$\kappa = \frac{1}{2}(n_e n_o)^{3/2}k_0 r_{51}E_y^e \tag{2.82}$$

Equations (2.81) are coupled mode equations for TE and TM mode, where $e^{\pm j\Delta\beta x}$ is the phase mismatch term caused by $\Delta\beta = \frac{2\pi}{\lambda_o}(n_o - n_e) = \beta_{TM} - \beta_{TE} \neq 0$, namely, the phase mismatch between TE and TM modes. The conversion efficiency will be degraded if $e^{\pm j\Delta\beta x} \neq 1$. The phase matching condition can be looked at from a

physical perspective: if the TE mode and TM mode are phase matched, the newly converted TE and the previous converted TE mode will propagate at the same pace and constructive interference will result. Otherwise, those two components will walk off and causes negligible mode conversion.

Provided that $\Delta\beta = \beta_{TM} - \beta_{TE} \neq 0$, in order to make $e^{\pm j\Delta\beta x} = 1$, we can let $\Delta\beta x = 2\pi$. By using the inter-digitated electrode pattern, a periodic E_y^e along the propagation direction (x) can be realized. And then, the electric field $E_y^e(x)$ can be expanded in a Fourier series:

$$E_y^e(x) = \sum_{M=1,3,5} \frac{4E_0}{M\pi} \sin\left(\frac{2\pi}{\Lambda} Mx\right) \tag{2.83}$$

Substitute it into equation (2.82),

$$\kappa(x) = \kappa_0 \left(\frac{-2j}{\pi}\right) \sum \frac{1}{M} \left[e^{j\left(\frac{2\pi}{\Lambda}M\right)x} - e^{-j\left(\frac{2\pi}{\Lambda}M\right)x}\right] \tag{2.84}$$

where

$$\kappa_0 = \frac{1}{2}(n_e n_o)^{3/2} k_0 r_{51} E_0 \tag{2.85}$$

Substitute it into equation (2.81),

$$\begin{cases} \dfrac{dA}{dx} = -\kappa_0 \left(\dfrac{2}{\pi}\right) B \displaystyle\sum_M \frac{1}{M} \left[e^{j\left(\frac{2\pi}{\Lambda}M + \Delta\beta\right)x} - e^{-j\left(\frac{2\pi}{\Lambda}M - \Delta\beta\right)x}\right] \\ \dfrac{dB}{dx} = -\kappa_0 \left(\dfrac{2}{\pi}\right) A \displaystyle\sum_M \frac{1}{M} \left[e^{j\left(\frac{2\pi}{\Lambda}M - \Delta\beta\right)x} - e^{-j\left(\frac{2\pi}{\Lambda}M + \Delta\beta\right)x}\right] \end{cases} \tag{2.86}$$

We have $\frac{2\pi}{\Lambda} M = \Delta\beta$ and if choosing $M = 1$ and ignore higher-order terms,

$$\begin{cases} \dfrac{dA}{dx} = +\dfrac{\kappa_0}{\pi/2} B \\ \dfrac{dB}{dx} = -\dfrac{\kappa_0}{\pi/2} A \end{cases} \tag{2.87}$$

$$\frac{2\pi}{\Lambda} = \Delta\beta \tag{2.88}$$

Equation (2.88) is called the phase matching condition.

Solve equations (2.87) with boundary condition,

$$\begin{cases} A^{TM}(x=0) = A_0 \\ B^{TE}(x=0) = 0 \end{cases} \tag{2.89}$$

The solution is

$$\begin{cases} A(x) = A_0 \cos(\kappa x) = A_0 \cos\left(\dfrac{\kappa_0}{\pi/2} x\right) \\ B(x) = -jA_0 \sin(\kappa x) = -jA_0 \sin\left(\dfrac{\kappa_0}{\pi/2} x\right) \end{cases} \tag{2.90}$$

Translate them into the form of intensity,

$$\begin{cases} \dfrac{I_A(x)}{I_0} = \cos^2(\kappa x) \\ \dfrac{I_B(x)}{I_0} = \sin^2(\kappa x) = 1 - \dfrac{I_A(x)}{I_0} \end{cases} \tag{2.91}$$

When $x = L$ so that $\kappa x = \frac{\pi}{2}$, we can obtain the expression of conversion efficiency regarding $\Delta\beta$, i. e. $\Delta\lambda$:

$$\frac{I_{TE}(\lambda)}{I_{TM}} = \frac{\sin^2\left[\dfrac{\pi}{2}\sqrt{1+\left(\dfrac{\Delta\beta/2}{\kappa}\right)^2}\right]}{1+\left(\dfrac{\Delta\beta/2}{\kappa}\right)^2} \tag{2.92}$$

CHAPTER III

DEVICE DESIGN *

3.1. Design process

The general design process of waveguides and devices is shown in Fig. 17. It begins with the high-level schematics design, then optimizing the detailed parameters using the simulation software, drawing the mask layout and having companies make the mask for us, developing the fabrication recipe for processes such as photolithography and wet/dry etching, and building the desired optical measurement setup and characterizing the device on it. If the device does not work, the problem will be figured out and the fabrication step will be redone with corrected or improved recipes. If it is a design issue, we may go back to the device simulation and start over.

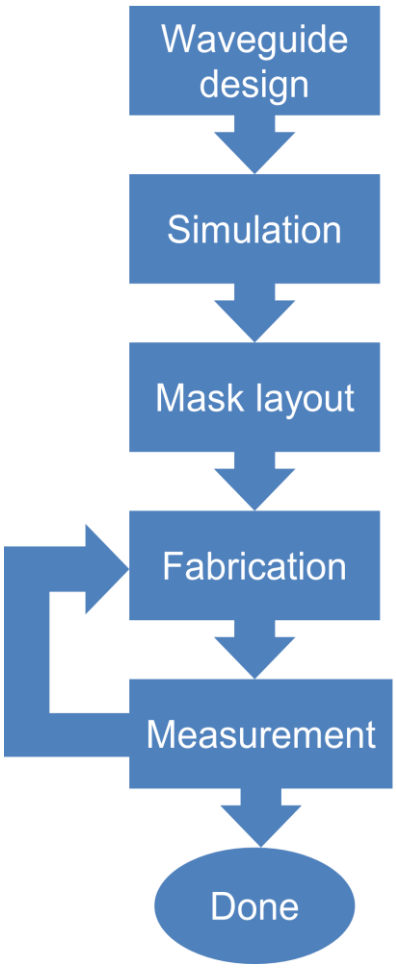

Fig. 17. Flow chart of general device design process.

3.2. As_2S_3 waveguides design and simulation

The research on the near field imaging of quantum cascade lasers reveals that a very stable mode pattern corresponding to a TM_{00} (the fundamental TM) mode can be obtained for a laser with a narrow active region [39]. The quantum cascade laser we use is a single mode, pulsed laser that emits light at the wavelength of 4.8 μm. In the vertical direction, which is perpendicular to the multilayer stack, the Full Width Half Maximum

(FWHM) of the mode is 2 μm, while in the horizontal direction; it is 10 μm, confined by the width of the active region (Fig. 18).

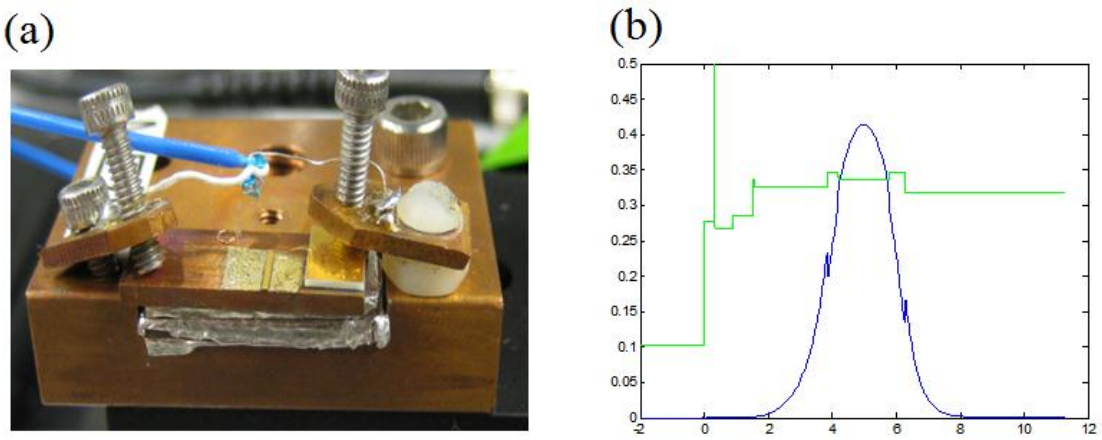

Fig. 18. Quantum cascade laser (a) and calculated mode profile (b).

Because of the working mechanism of QC lasers, which emit light by the electrons tunneling between cascading thin layers, the polarization of the optical output is perpendicular to that thin-layer stack. As a result, only TM modes can be generated by QC lasers, as shown in Fig. 19. Therefore, As_2S_3 waveguides are designed and optimized for TM mode.

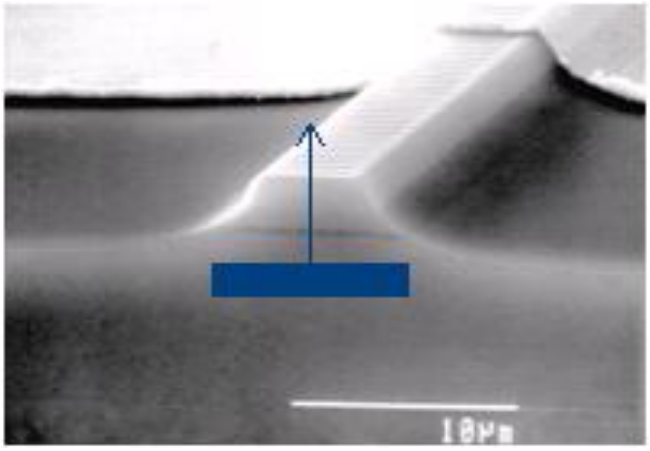

Fig. 19. SEM picture of quantum cascade laser with polarization indication.

Due to high mode confinement, channel As_2S_3 waveguides consisting of a $LiNbO_3$ substrate, an As_2S_3 waveguide core and an air cladding are designed. The index of core (As_2S_3) is 2.408 at the wavelength of 4.8 μm [9], which is larger than that of $LiNbO_3$ (2.070) and the cladding (air, 1.0).

In order to optimize waveguides that work at the fundamental TM mode and minimize the mode mismatching loss, the beam propagation method (OptiBPM, from Optiwave) is employed to simulate light propagation in straight waveguides, as shown in Fig. 20. The simulated single mode regions are shown in Fig. 20 (b). For example, assume the width of the waveguide is 7 μm, if the height is below 5.6 μm, the waveguide works in single mode condition. If the waveguide gets wider, the maximum height turns out to be smaller.

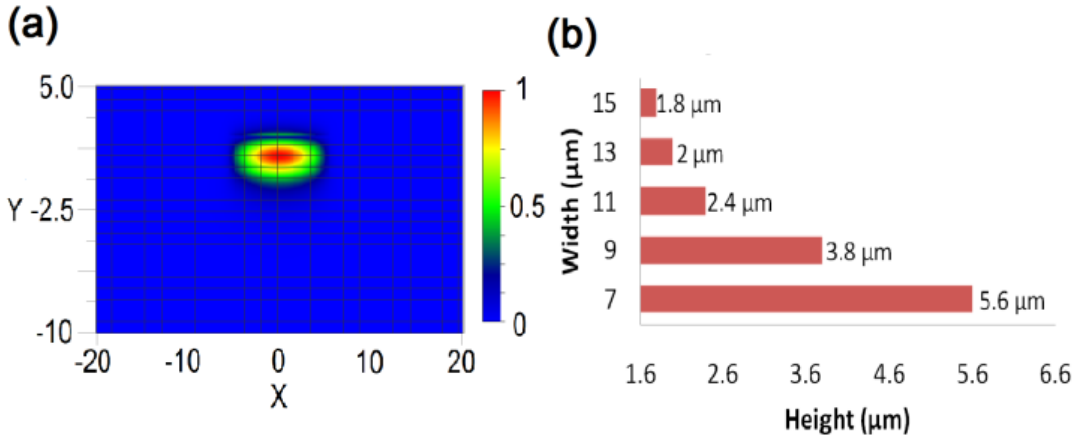

Fig. 20. Mode profile (a) and single mode condition (b) from OptiBPM.

As for bent waveguides, traditional beam propagation method is unreliable due to its paraxial approximation. Therefore, we apply FIMMWAVE (from Photo Design) using a conformal mapping method to model bent waveguides (with constant radii) instead [Fig. 21 (a)]. As mentioned above, at the wavelength of 4.8 µm, the refractive index of the As_2S_3 is 2.408 [9] while that of the lithium niobate substrate is 2.070. Such high index contrast makes tightly bent waveguides down to 100 µm radius possible, as shown in Fig. 21 (b).

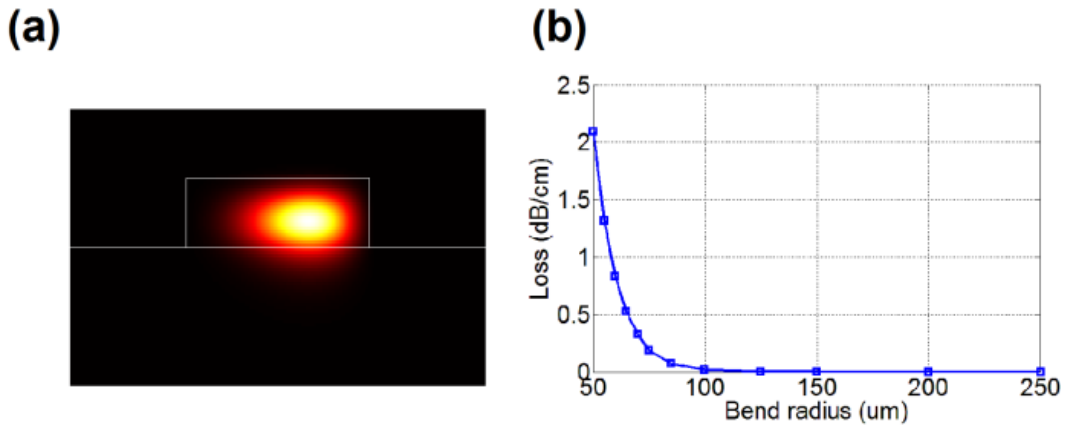

Fig. 21. Mode profile in bent waveguide (a) and bent loss from FIMMWAVE (b).

According to simulation results, straight channel waveguides that allow only the fundamental TM mode to propagate are designed (Fig. 22), of which the height is 2 μm and the width is 11 μm. Similar waveguides of width varying from 7 μm to 15 μm are also designed for measurement comparison. The bent channel waveguide pattern has a series of waveguides of width 11 μm and bend radii from 50 μm to 8 mm.

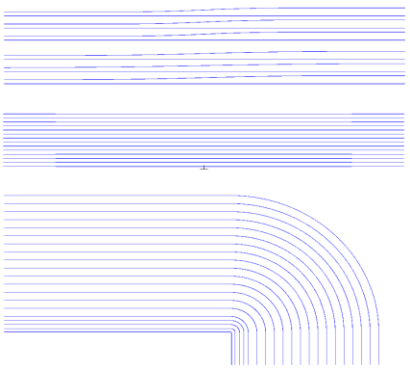

Fig. 22. Mask layout of designed waveguides.

3.3. Integrated polarization converters

According to the review on polarization conversion in Chapter II, mode conversion between TE and TM modes in lithium niobate can be achieved by applying an electric field to introduce an off-diagonal element of the electro-optic tensor. In order to utilize the largest EO coefficient r_{51} [equation (2.72)], the $LiNbO_3$ substrate has to be configured in an x-cut manner, and then the propagation can be set to y or z direction. In the former setting, TE and TM modes suffer from strong birefringence experiencing different refractive index (extraordinary n_e and ordinary n_o) during propagation, which gives us more flexibility in manipulating those two modes, but at the same time requires compensation for the phase mismatch. Inter-digitated electrodes are then designed to generate periodic change of the electric field strength along the light propagation direction to fulfill that purpose. From equation (2.88), we have the following equation that determines the period of the electrode Λ:

$$\frac{2\pi}{\lambda_0}\left|n_{eff}^{TM} - n_{eff}^{TE}\right| = \frac{2\pi}{\Lambda} \tag{3.1}$$

The complete structure is shown in Fig. 23.

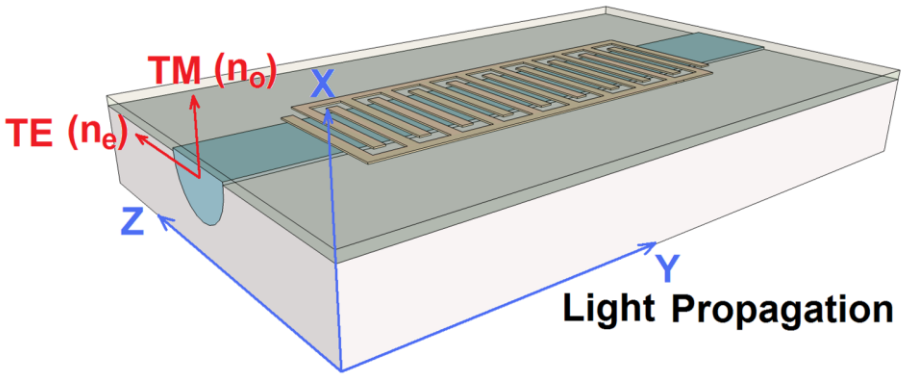

Fig. 23. Integrated polarization converter using Ti:$LiNbO_3$.

The phase matching condition, on the other hand, limits the conversion wavelength into a range as small as a few nanometers. On the contrary, for the alternative x cut, z propagation scheme, where the effective refractive index of TE and TM are the same ideally, the phases are inherently matched [40]. As a result, the bandwidth of polarization conversion is greatly enlarged. In that case, a set of simpler and non-periodic electrodes is all that we need to generate the electric field. Two types of polarization converters are illustrated in Fig. 24.

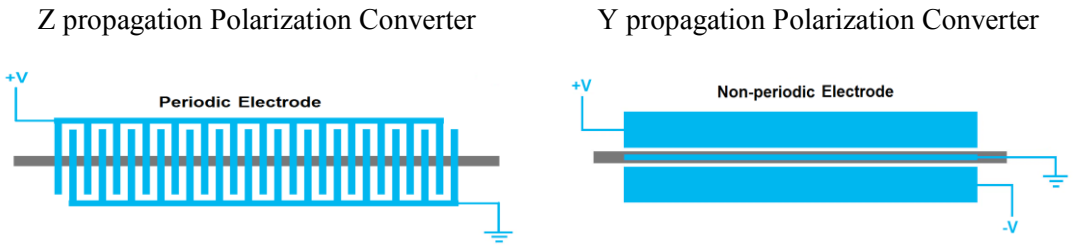

Fig. 24. Two types of polarization converter configurations.

The major difference between these two types of polarization converters lies in the electrode configuration: for y-propagation polarization converter, the inter-digitated electrode pattern has 500 periods, each period is 29 μm long and the total length is about 1.5 cm. While for the z-propagation one, a set of straight electrodes is designed, including two outer electrodes separated by 16 μm and a 3 μm wide center one. The length for all of them is 2 cm.

The research is carried out in our lab at Texas A&M University, where we have a thulium fiber laser that emits light at the wavelength of 2.05 μm. In order to optimize the performance of integrated polarization converters for that wavelength, the titanium diffused waveguides need to be designed specially. According to previous study on titanium diffused waveguide in lithium niobate at the wavelength of 2.05 μm, waveguides that have the width of 7 μm, 9 μm and 11 μm are designed (Fig. 25).

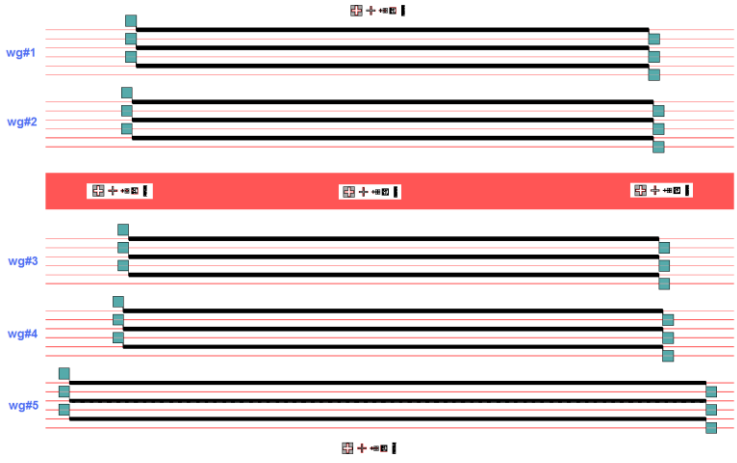

Fig. 25. Mask layout for integrated polarization converters.

In order to facilitate the alignment between different layers and examine the exposure and developing conditions, alignment marks are placed on the mask (Fig. 26).

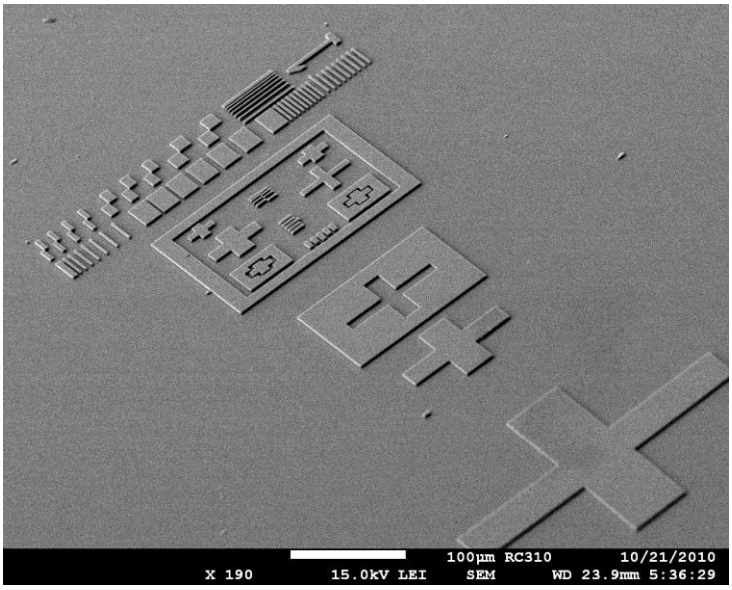

Fig. 26. SEM picture of alignment marks.

3.4. As_2S_3-Ti: $LiNbO_3$ taper coupler

3.4.1. Development on modeling method

As describe in Chapter II, modes are solutions to the wave equation. The wave equation can be viewed as an eigenvalue problem: the electric fields of modes are eigen-functions and the square of propagation constants are the eigenvalues [41]. So mathematically, the modes form a set of orthogonal basis of the solution space to the wave equation. As a result, they are independent and do not have interactions normally. That is to say, once excited, each mode carries power and propagates along the waveguide independently of the presence of other modes [41]. From the physical perspective, modes are a set of pre-determined electromagnetic field structures that are invariable along the light propagation direction, which can be identified from intensity patterns formed on the cross-sectional plane in the waveguide.

However, if there is a disturbance (perturbation) in the waveguide, such as surface corrugations and sidewall protruding, they may become coupled and energy may transfer from one to another. The well-known coupled mode theory is developed to understand such phenomenon.

As mentioned, a typical scenario for studying mode coupling is a directional coupler, consisting two adjacent waveguides. In each waveguide, only one mode is allowed to propagate. The coupled mode theory analyzes the coupled waveguides by taking one waveguide as the subject, studying the influence of the perturbation imposed by the presence of the other one. The supermode theory, however, views the coupled waveguides as a whole system, i. e. a composite two-waveguide structure, and the

normalized local modes of the system are called supermodes. The supermode theory provides us with another perspective to study the coupled waveguides.

Nevertheless, both theories describe mode coupling for scenarios that coupled waveguides are invariable along the propagation direction. But the taper coupler is a varying structure where the width of one of the waveguides is constantly changing along the propagation direction. However, the coupler can be divided into a succession of infinitely short sections. The length of each section is so small that the width can be regarded as invariant. So the simulation of a taper coupler can be divided into two steps: modeling of individual divisions and a cascade of individual models. For each division, as the width is deemed constant, it is actually a simple directional coupler, in which there are fundamental supermode and first order supermode, named as even mode E_e and odd mode E_o respectively according to the symmetry of their field distribution: for the even mode, two lobes have the same sign while for the odd mode, they have opposite signs., as shown in Fig. 27. The total field is a linear combination of even and odd modes, which are the normalized modes of the coupled system.

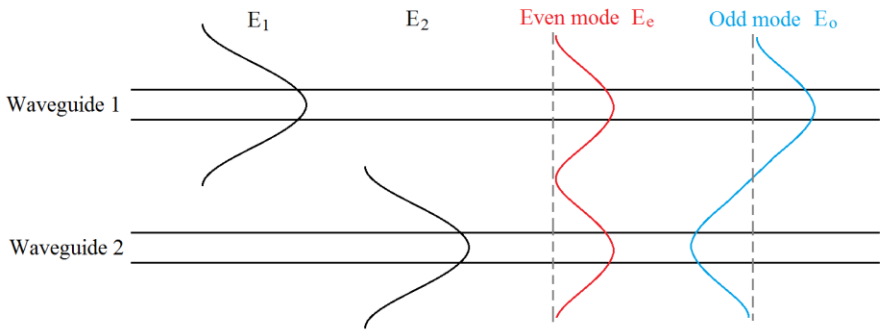

Fig. 27. Individual modes and supermodes in a directional coupler.

According to coupled mode equations, the directional coupler is described by the following equations:

$$\begin{cases} \frac{dE_1}{dz} = -j\kappa_{12}E_2 exp[-j(\beta_2 - \beta_1)z] \\ \frac{dE_2}{dz} = -j\kappa_{21}E_1 exp[+j(\beta_2 - \beta_1)z] \end{cases} \tag{3.2}$$

where E_1 and E_2 are the electric fields of modes in two waveguides, κ is the coupling strength, defined as

$$\kappa = \sqrt{\kappa_{12}\kappa_{21}}$$

$$\kappa_{12} = \frac{\omega\varepsilon_0}{4}\int [n_1^2(x,y) - n_2^2(x,y)]\, E_2(x,y)E_1(x,y)dxdy \tag{3.3}$$

$$\kappa_{21} = \frac{\omega\varepsilon_0}{4}\int [n_2^2(x,y) - n_1^2(x,y)]\, E_1(x,y)E_2(x,y)dxdy$$

Solving the coupled mode equations, we can have the expression of evolvement of two modes in each waveguide, which shows the energy flow back and forth in the waveguides as light propagates. Please refer to the appendix for details. Supermode theory, however, provides another perspective.

For a directional coupler, assume at the input light is injected into waveguide 1 only. So both even and odd modes are excited, of the same magnitude ($1/\sqrt{2}$), as shown in Fig. 28. Each of the modes propagates through the waveguide independently. Because of the difference in phase velocity, their phase becomes different and that difference increases as they propagate. As a result, the sum of two modes in waveguide 2 is no longer 0, and meanwhile the sum in waveguide 1 becomes smaller. And thus part of the energy is transferred from waveguide 1 to waveguide 2. When the phase difference reaches π, as shown on the right, the sum of two modes indicates that all energy of the

total field is transferred into waveguide 2. A similar process continues as light propagates, resulting in an oscillating pattern of the coupling curve.

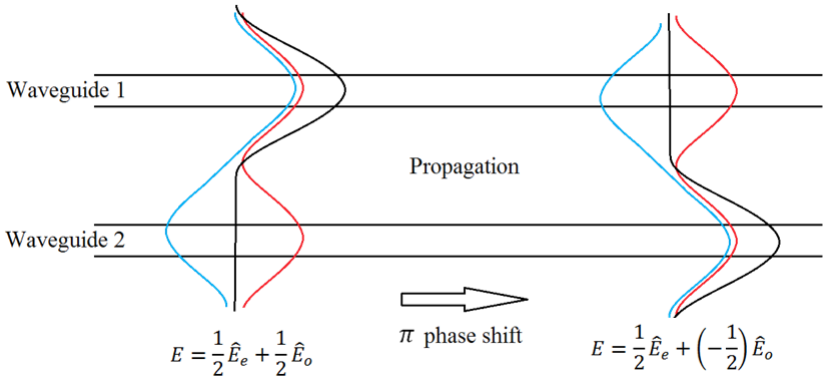

Fig. 28. Directional coupler in the view of supermode theory.

If the propagation constants of the modes in the individual waveguides are the same, namely, they are phase matched, the two lobes of the even and odd mode will be of the same size. If the propagation constants of two modes are different, that is, the phase is mismatched, the symmetry of lobes of E_e and E_o is broken, and their shapes are different. When the phase mismatch is large, the two waveguides are effectively decoupled: a wave propagating in either one of them is virtually unaffected by the existence of the other, and the supermodes of the composite structure just become those of the individual waveguides [42]. Phase mismatch is defined as the difference of the propagation constants of the two individual modes while β_C is for the two supermodes similarly:

$$\delta = \frac{\beta_2 - \beta_1}{2} \tag{3.4}$$

$$\beta_c = \frac{\beta_e - \beta_o}{2} \tag{3.5}$$

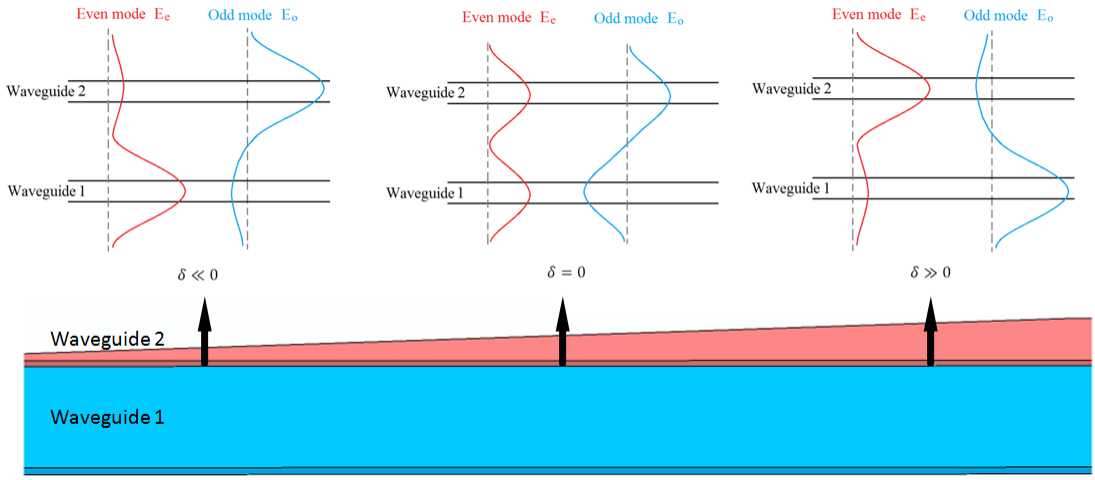

Fig. 29. Taper coupler in the view of supermode theory.

As shown in Fig. 29, if δ is much smaller than 0, most of the energy of the even mode is located in waveguide 1 while if it is much larger than 0, most of the energy of the even mode is located in waveguide 2. The opposite is true for the odd mode. So, the essence of taper coupling is to spatially transfer the energy of a supermode (even mode) from one waveguide to the other by designing the tapered waveguide so that δ sweeps from a negative value to positive value while suppressing the coupling to the other supermode (odd mode).

Assume waveguide 2 is made of material that has a higher refractive index than waveguide 1. As mentioned above, phase mismatch is defined as the difference between propagation constants $\beta_1 \, and \, \beta_2$ in the individual waveguide. β_1 is constant since

waveguide 1 is a uniform waveguide. For waveguide 2, we have $\beta_2 = \frac{2\pi}{\lambda} n_{eff}(w)$. As the width increases, the mode effective index gets bigger since a larger percentage of the mode will be located in waveguide 2, which is assumed to have a larger refractive index. Accordingly, β_2 increases. If initially β_2 is smaller than β_1 and finally it is larger than β_1, δ sweeps from a negative value to a positive value. If the even mode propagates primarily and the odd mode is effectively suppressed, energy will be spatially transferred from waveguide 1 to waveguide 2 as a result.

The larger the difference between the refractive index of waveguide 1 and waveguide 2, the larger scope δ covers, and the more thorough the energy is transferred spatially. Ideally, δ changes from negative infinity to positive infinity, whereas in practice, it is determined by the materials and structure.

By studying the transformation between individual modes and supermodes, the relation between the phase mismatch of the supermodes and that of the individual modes can be obtained, which gives a complete description of the modeling of directional couplers by parameters δ, κ and β_c [35].

$$\beta_c^2 = \delta^2 + \kappa^2 \tag{3.6}$$

β_c can be computed using β_e and β_o, δ by β_1 and β_2, and then κ can be calculated. Then we have a complete mathematical description of the model. Following the same method, models of all the divisions in the taper coupler can be obtained.

Subsequently, a transfer matrix formalism is derived to cascade all the models based on coupled mode equations. In the matrix form, the solution to the coupled mode equations is

$$\begin{bmatrix} E_1(z) \\ E_2(z) \end{bmatrix}$$

$$= \begin{bmatrix} \left[cos(\beta_c z) + \frac{j\delta}{\beta_c} sin(\beta_c z)\right] e^{-i\delta z} & -\frac{j\kappa}{\beta_c} sin(\beta_c z) e^{-i\delta z} \\ -\frac{j\kappa}{\beta_c} sin(\beta_c z) e^{i\delta z} & \left[cos(\beta_c z) - \frac{j\delta}{\beta_c} sin(\beta_c z)\right] e^{i\delta z} \end{bmatrix} \begin{bmatrix} E_1(0) \\ E_2(0) \end{bmatrix} \tag{3.7}$$

where $E_1(0)$ and $E_2(0)$ are the input electric fields in waveguide 1 and 2 respectively, let $z = z_0$ and re-arrange the equation,

$$\begin{bmatrix} E_1(0) \\ E_2(0) \end{bmatrix}$$

$$= \begin{bmatrix} \left[cos(\beta_c z_0) + \frac{j\delta}{\beta_c} sin(\beta_c z_0)\right] e^{-i\delta z_0} & -\frac{j\kappa}{\beta_c} sin(\beta_c z) e^{-i\delta z_0} \\ -\frac{j\kappa}{\beta_c} sin(\beta_c z_0) e^{i\delta z_0} & \left[cos(\beta_c z_0) - \frac{j\delta}{\beta_c} sin(\beta_c z_0)\right] e^{i\delta z_0} \end{bmatrix}^{-1} \begin{bmatrix} E_1(z_0) \\ E_2(z_0) \end{bmatrix} \tag{3.8}$$

Substitute it into the original solution, and let $z = z_0 + \Delta z$, we have

$$\begin{bmatrix} E_1(z_0 + \Delta z) \\ E_2(z_0 + \Delta z) \end{bmatrix}$$

$$= \begin{bmatrix} \left[cos(\beta_c \Delta z) + \frac{j\delta}{\beta_c} sin(\beta_c \Delta z)\right] e^{-i(\delta \Delta z)} & -\frac{j\kappa}{\beta_c} sin(\beta_c \Delta z) e^{-i[\delta(z_0+\Delta z)+\delta z_0]} \\ -\frac{j\kappa}{\beta_c} sin(\beta_c \Delta z) e^{i[\delta(z_0+\Delta z)+\delta z_0]} & \left[cos(\beta_c \Delta z) - \frac{j\delta}{\beta_c} sin(\beta_c \Delta z)\right] e^{i(\delta \Delta z)} \end{bmatrix} \begin{bmatrix} E_1(z_0) \\ E_2(z_0) \end{bmatrix} \tag{3.9}$$

Then we arrive at the transfer matrix formalism relating the model at $z_0 + \Delta z$ to the model at z_0, and by multiplying the matrices in order, the models are cascaded. As a result, the electric field at a certain point z can be obtained once we know the input $E_1(0)$ and $E_2(0)$. Define M as follow:

$$M(z_0+\Delta z; z_0)$$

$$= \begin{bmatrix} \left[\cos(\beta_c \Delta z) + \frac{j\delta}{\beta_c}\sin(\beta_c \Delta z)\right] e^{-i(\delta \Delta z)} & -\frac{j\kappa}{\beta_c}\sin(\beta_c \Delta z) e^{-i[\delta(z_0+\Delta z)+\delta z_0]} \\ -\frac{j\kappa}{\beta_c}\sin(\beta_c \Delta z) e^{i[\delta(z_0+\Delta z)+\delta z_0]} & \left[\cos(\beta_c \Delta z) - \frac{j\delta}{\beta_c}\sin(\beta_c \Delta z)\right] e^{i(\delta \Delta z)} \end{bmatrix} \quad (3.10)$$

The algorithm is summarized below:

1	Discretize the taper coupler into a sequence of sufficiently small divisions;
2	Regard each section as a directional coupler and model it using a computer program to obtain mode propagation constants β_1, β_2, β_e and β_o, and compute δ, β_c and κ;
3	Calculate the individual transfer matrix of each division based on parameters δ, β_c and κ;
4	Cascade all the divisions together by multiplying matrices in order; $$\begin{bmatrix} E_1(L) \\ E_2(L) \end{bmatrix} = \begin{bmatrix} E_1(z_{i+1}) \\ E_2(z_{i+1}) \end{bmatrix} = M(z_{i+1}; z_i) \cdot M(z_i; z_{i-1}) \cdots M(z_1; 0) \begin{bmatrix} E_1(0) \\ E_2(0) \end{bmatrix}$$
5	Calculate the coupling efficiency: If mode in waveguide 1 is excited only at the beginning, the coupling efficiency can be obtained: $$Coupling\ effciency = \frac{E_2(L)}{E_1(0)} \quad (assuming\ E_2(0) = 0)$$

3.4.2. Model building

The structure of an As_2S_3-Ti: $LiNbO_3$ coupler is illustrated in Fig. 30. A titanium diffused waveguide is formed in lithium niobate substrate (Ti: $LiNbO_3$). On the substrate

surface is a piece of tapered As_2S_3 rectangular waveguide, which is separated from the titanium diffused waveguide by a few microns. Both waveguides work in single mode condition. In Ti: $LiNbO_3$ fabrication process, the $LiNbO_3$ material under the Ti pattern rises up from the substrate surface during titanium diffusion, resulting in a 0.1 μm high bump. In order to avoid the scattering loss caused by the rough surface of the bump, an As_2S_3 waveguide is placed to the side of the bump (side coupling) instead of on the top. For simplicity, air cladding is used. The height of As_2S_3 waveguide is 470 nm.

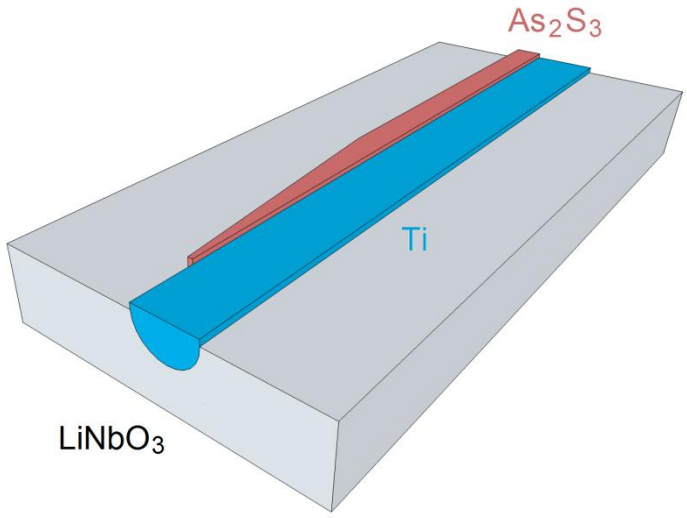

Fig. 30. Configuration of As_2S_3-Ti: $LiNbO_3$ taper coupler.

FIMMWAVE (Photon Design Ltd), a commercial software that has excellent mode solving capability, is used as a mode solver in our study. The resolution and the size of the simulation window are tested to prevent artificial errors.

Simulation starts with uncoupled waveguides, and their eigen-modes are computed individually without the presence of the other one. The propagation constants of the Ti waveguide mode and As_2S_3 waveguide mode are found to be β_1 and β_2 respectively. Then the model for the coupled system is built, and the even mode (β_e) and odd mode (β_o) are found, as Fig. 31 shows. Then δ, β_c & κ are calculated according to the aforementioned formulas.

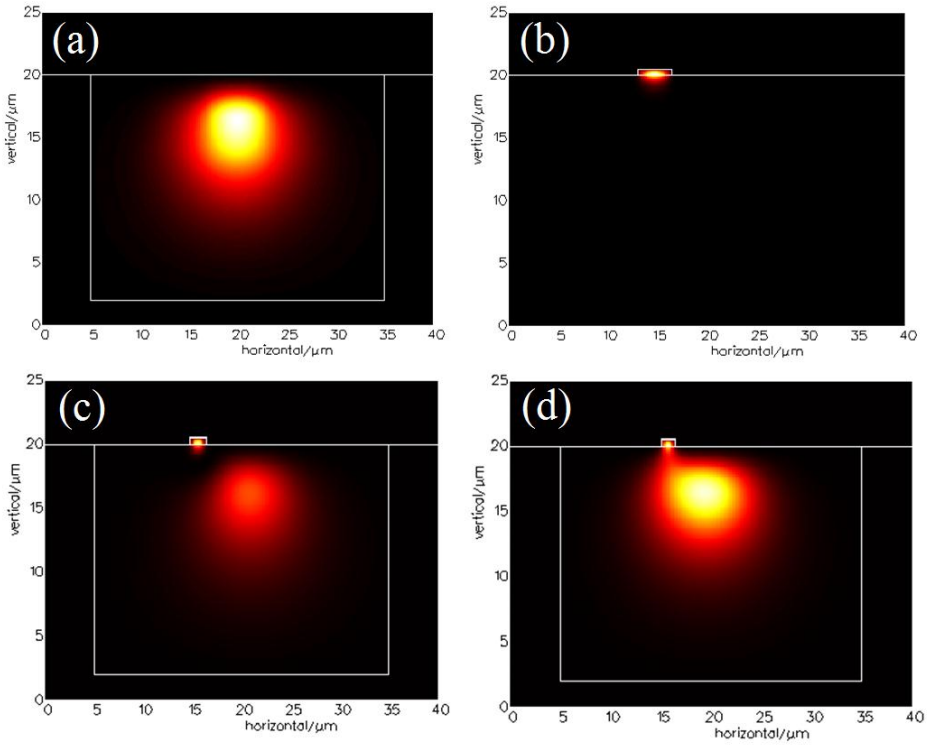

Fig. 31. The fundamental mode of the Ti waveguide (a) and the As_2S_3 waveguide (b) and the even (c) and odd mode (d) of coupled waveguides.

Two mode solving algorithms in FIMMWAVE are experimented with finite difference method (FDM) and film mode matching method (FMM). FDM is widely used

in electromagnetic wave simulations to model graded index structures, such as Ti diffused waveguides. FMM is good for structures consisting of a large uniform area, As_2S_3 rectangular waveguides for example. Results show that FMM gives much smoother results than FDM (Fig. 32). The ripples in the calculated curves are a strong indication of artificial numerical errors. Because As_2S_3 taper is the key to our As_2S_3-Ti: $LiNbO_3$ taper coupler, FMM solver is used to implement the modeling.

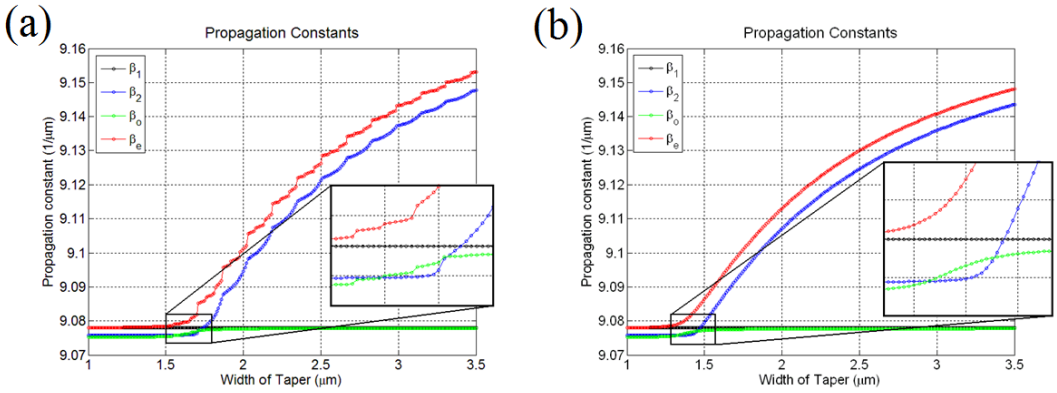

Fig. 32. Comparison of FDM (a) and FMM (b).

The approximation of a width varying waveguide with a sequence of width-constant waveguides is mathematically equivalent to the approximation of a continuous integral with the discrete summation, which induces error inevitably. As the matrices cascade, the previous error passes on, and combines with the error of the present one. Consequently, such accumulation of the errors will manifest at the end of the taper coupler, even if very small error exists in intermediate models. Simulation experiments (Fig. 33) show that discretization spacing (Δz) is critical to the numerical error, where

the length is set to 1000 μm, while N is the sampling rate, so Δz =L/N. The larger an error exists, the smaller the spacing needs to be, and the heavier the computation load is required.

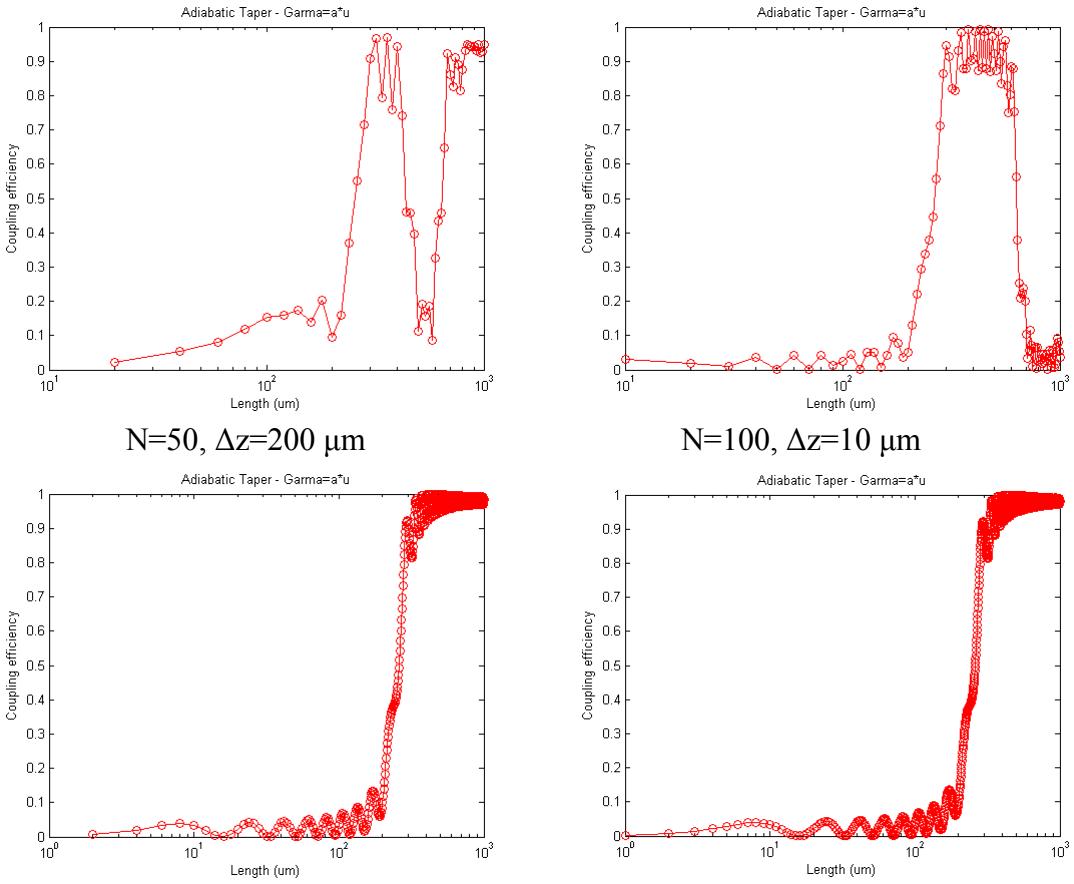

Fig. 33. Simulation experiments on numerical errors using theoretical models at the wavelength of 1550 nm, the total length is set to be 1000 μm.

In order to reduce the error at the first place, the trapezoidal approximation algorithm $\frac{\beta_c(i)+\beta_c(i+1)}{2} \cdot \Delta z$ is adopted to substitute the left Riemann sum $\beta_c(i) \cdot \Delta z$ in the

transfer matrix formalism, which saves the computing resources greatly. Moreover, interpolation is used to reach beyond the resolution limit of FIMMWAVE.

3.4.3. Simulation results

Modal parameters of four modes in all divisions at different widths of As_2S_3 taper are plotted in Fig. 34, including the propagation constants, the effective indices and the calculated δ, κ and β_c. We see that the propagation constant of the As_2S_3 mode increases gradually as its width becomes larger whereas the Ti mode remains constant.

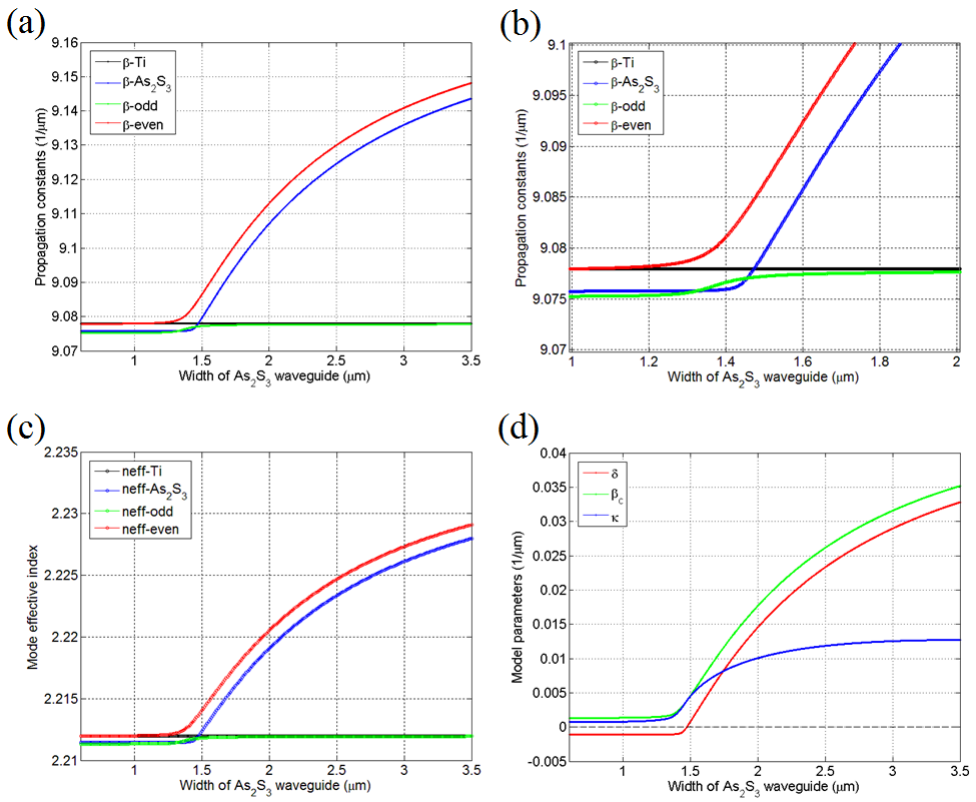

Fig. 34. The propagation constants of models at different width (a) [the expanded graph around 1.4 μm(b)], the effective indices (c), and the calculated modal parameters (d).

From Fig. 34 (b) we see clearly that the propagation constant of the even mode coincides with that of the Ti mode first and then gradually follows the trend of the As_2S_3 mode. On the contrary, for the odd mode, the propagation constant goes from the As_2S_3 mode to the Ti mode.

During this process, there is a point that the propagation constants of the As_2S_3 mode and the Ti mode are equal, corresponding to where the phase mismatch equals to 0. From the graph, it is the point where the β- As_2S_3 and β-Ti curves cross, corresponding to the width of 1.47 μm, called the critical width. It is the critical point where two waveguides are phase matched, and the energy is equally distributed in the two waveguides for both the even and odd mode. In other words, it can be regarded as the mid-point of the mode coupling process from Ti waveguide to As_2S_3 waveguide.

As the width of the As_2S_3 waveguide increases, the increasing rate of propagation constant β_2 $\beta_2$gets smaller. That means the phase mismatch δ, the difference between the propagation constants of two waveguides, will eventually cease to grow. The normalized phase mismatch γ is introduced to characterize such variation [35], as shown in Fig. 35.

$$\gamma = \frac{\delta}{\kappa} \tag{3.11}$$

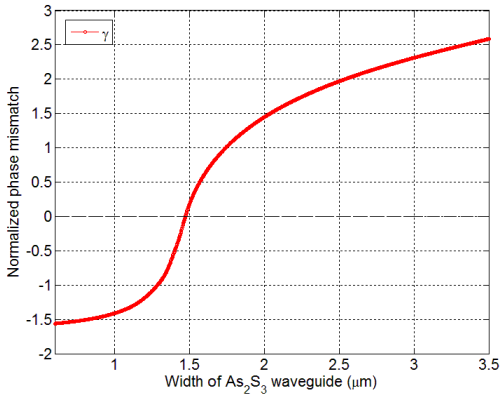

Fig. 35. Normalized phase mismatch γ.

Among the various types of taper geometries, the linear taper is most straightforward and provides insights into the general taper design. Fig. 36 shows the coupling efficiency of linear tapers of different lengths, with width varying from 1.0 μm to 3.5 μm. The squares stand for the coupling efficiency and the bars represent the magnitude of oscillation. There is an optimum point that the maximum coupling efficiency reaches 96% when the length is 5 mm. The inset curve shows the percentage of energy coupled as light propagates through a 5 mm long linear taper. We can see that it consists of a monotonically ascending part and a subsequent oscillation part. The coupling is mostly contributed by the former part while the latter is due to resonance effects.

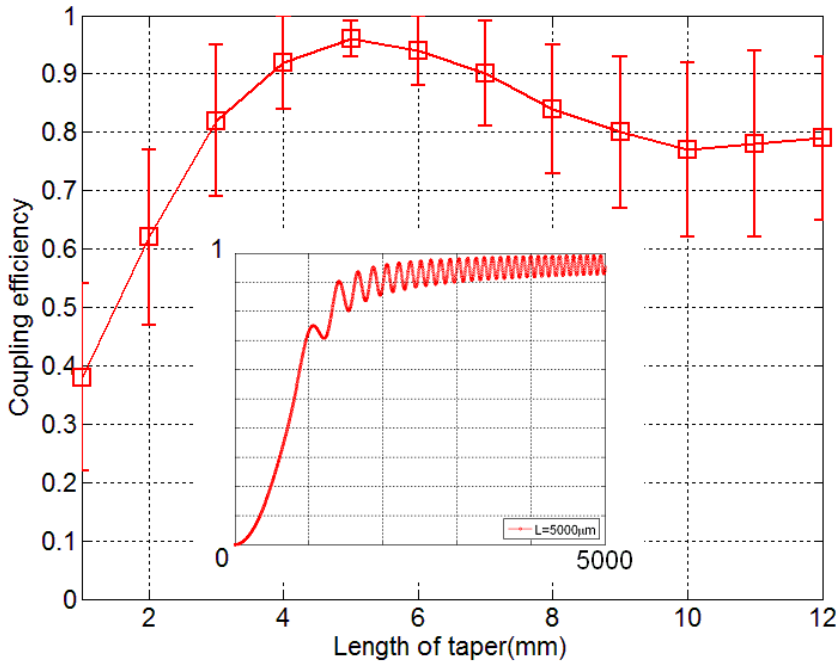

Fig. 36. Coupling efficiency for tapers of different length, with the inset figure showing the coupling process of a 5 mm long taper, i. e., the coupling efficiency versus the location along the taper.

For the even mode, the larger γ is, the more energy is located in the As_2S_3 waveguide and the less in Ti waveguide, while it is vice versa for the odd mode. Since the even mode is the mode to couple, the energy remaining in the Ti waveguide imposes an ultimate limit to the coupling efficiency. From the curve of γ in Fig. 35, we learn that at the end of the taper, γ is 2.59. Because γ is not large enough, there is still coupling between the two waveguides. Such coupling deteriorates the coupling efficiency and causes it to oscillate. The behavior of the coupler in this region is similar to that of a resonant coupler. As a result, a certain amount of energy flows back and forth between the two waveguide modes.

From the view of supermode theory, the oscillation is a result of beating between

the even and odd modes. Although the even mode is desired, the coupling of the odd mode is not completely suppressed, for example, if the length of the taper is not sufficiently long according to the adiabatic criterion in [35]. When the odd mode propagates in the taper, there is coupling between the even and odd modes and a small amount of energy flows back and forth constantly. Since at the end of the taper, the majority of the energy of the even mode is in the As_2S_3 waveguide and that of the odd mode is in the Ti waveguide, there is a constant energy flow between two waveguides, and consequently the coupling efficiency oscillates.

In the presence of mode beating, it is not necessarily the longer taper, the better the coupling. There exists an optimum length for a taper with fixed width variation: if it is shorter than that, the mode is under-coupled since it is far away from the adiabatic criterion for 100% coupling; if considerably longer than that, the coupling efficiency is degraded by the resonant effect, as Fig. 36 shows. In order to reduce the problem of mode beating, we must enlarge γ, either by increasing the phase mismatch δ or by decreasing the coupling strength κ. δ is limited by the property of the materials whereas κ can be controlled by the structure. For example, κ can be reduced by introducing a gap between As_2S_3 waveguide and Ti waveguide.

Due to process errors in fabrication, the width of the tapered As_2S_3 waveguides may not be exactly the same as the design, especially the tip width, so it is necessary to study the influence of variation of the width. For simplicity, the objective is still TM polarization, at the wavelength of 1531 nm, and the height of the waveguide is 470 nm. The result is shown in Fig. 37, in which the length is fixed to be 5 mm, while the

nominal width is 1.0 μm for the tip and 3.5 μm for the end. From the graph, it is known that the end width of the taper matters less than the initial width, namely the tip width, indicating the initial part of the taper is more important than the final part. There is an optimum value of tip width for achieving the smallest oscillation and the highest coupling. Additionally, the influence of offset, that is, the relative position of As_2S_3 waveguide to Ti waveguide, is also investigated, as shown in Fig. 38. Negative values mean the As_2S_3 waveguide is closer to the Ti waveguide while positive ones mean it is away from the Ti waveguide. As the two waveguides move closer, the spatial distance between the two waveguides is smaller, and thus the coupling is stronger. As a result, the mode beating becomes more severe, which leads to a larger oscillation at the end of the taper. But the sensitivity remains at a lower level compared to that of tip width.

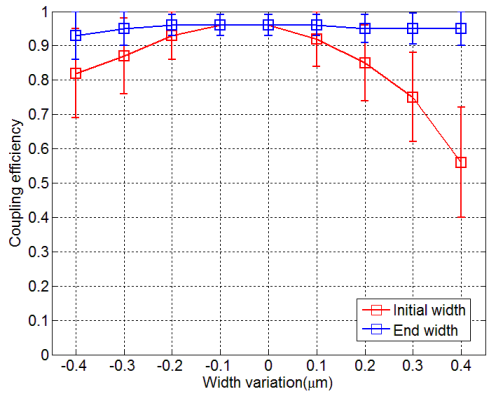

Fig. 37. Study on width variations.

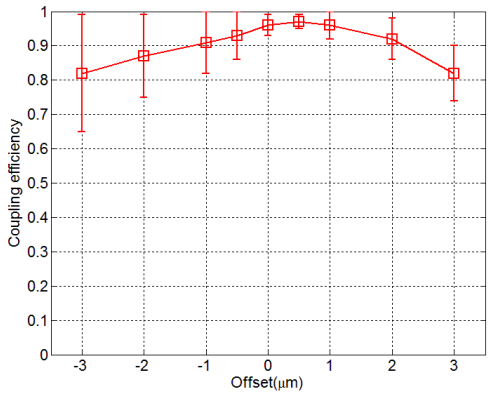

Fig. 38. Study on offset.

Although the coupling efficiency can be as high as 96%, it takes quite a few millimeters to get a decent coupling efficiency for linear tapers, which is not acceptable for ultra-compact design.

To further explore the design, the coupling curve is re-examined and the linear taper is decomposed for analysis. Based on the study on linear tapers, efficient coupling takes place in the first part of taper where the As_2S_3 waveguide expands across the critical width and correspondingly the phase mismatch δ changes from a negative value to a positive one. The critical width region contributes to efficient coupling and we want it to be sufficiently long. Once most of energy has entered the As_2S_3 waveguide, the rest of the taper can be shortened. As a consequence, we have arrived at a two-stage taper, as shown in Fig. 39.

Furthermore, since the end width of the first stage (transition width) can now be a much smaller value, the rate of width change is reduced largely. Simulation shows that for the first part of a two-stage taper, if the width varies from 1.0 μm to 1.6 μm in the length of 2 mm, the width increasing rate is 3×10^{-4}, which is equivalent to an 8.3 mm long linear taper. Along with a 1 mm long second part, with width varying from 1.6 μm to 3.5 μm, the total length is 3 mm. The coupling efficiency can still reach above 90%, whereas the total length is reduced by 64%.

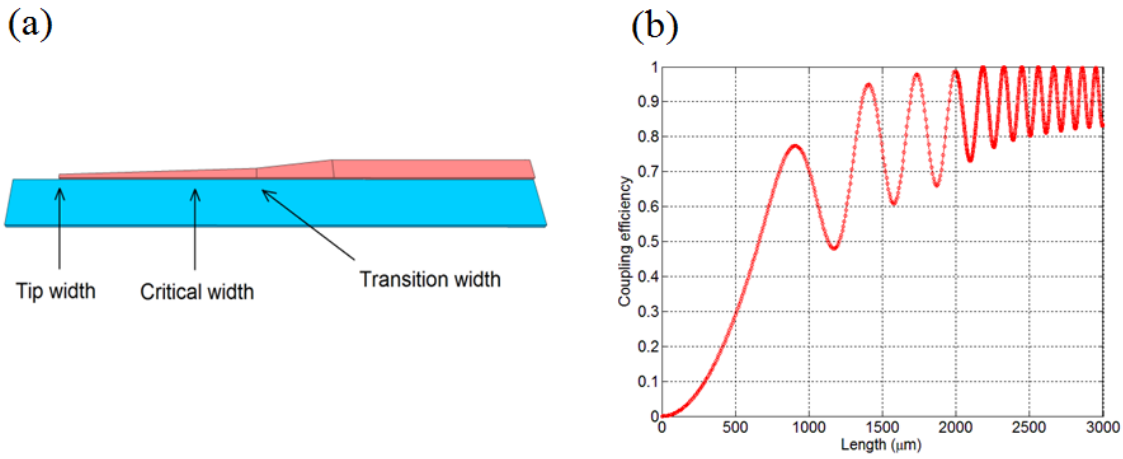

Fig. 39. Two-stage taper coupler design: configuration (a), coupling curve (b).

3.4.4. Test device design

To test the As_2S_3-Ti: $LiNbO_3$ taper coupler design, S-shaped structures are fabricated and tested on a near IR measurement setup. As shown in Fig. 40, it is composed of two taper couplers and an S-shaped As_2S_3 waveguide to connect them. The taper couplers follow the two-stage taper coupler design.

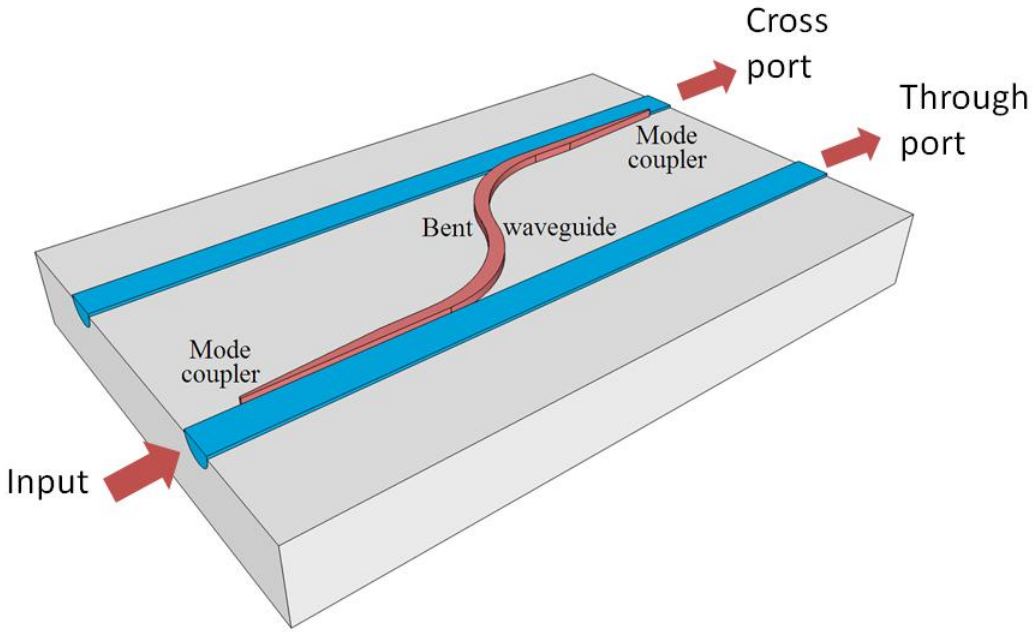

Fig. 40. Sbend structure with two taper couplers.

CHAPTER IV

FABRICATION AND PROCESS DEVELOPMENT *

4.1. Mid IR As_2S_3 waveguides

Standard microelectronics technology is adapted to develop the fabrication process for mid IR As_2S_3 waveguides (Fig. 41). Nicely shaped waveguides can be expected through optimized processes using the state of art photolithography and reactive ion etching technology, and stability and reproducibility won't be a big issue.

---

* Part of this chapter is reprinted with permission from "Low-loss chalcogenide waveguides on lithium niobate for the mid-infrared" by Xin Xia, Qi Chen, Candice Tsay, Craig B. Arnold, and Christi K. Madsen, Opt. Lett. 35, 3228-3230, 2010, copyright 2010 by OSA.
Part of this chapter is reprinted with permission from "Integrated polarization converters for mid-infrared applications" by Xin Xia and Christi K. Madsen, Lasers and Electro-Optics (CLEO) and Quantum Electronics and Laser Science Conference (QELS), 2010, copyright 2010 by IEEE.
Part of this chapter is reprinted with permission from "Analysis of As_2S_3-Ti: $LiNbO_3$ taper couplers using supermode theory" by Xin Xia, Yifeng Zhou, and Christi K. Madsen, submitted to IEEE Journal of Lightwave Technology, 2011, copyright 2011 by IEEE.

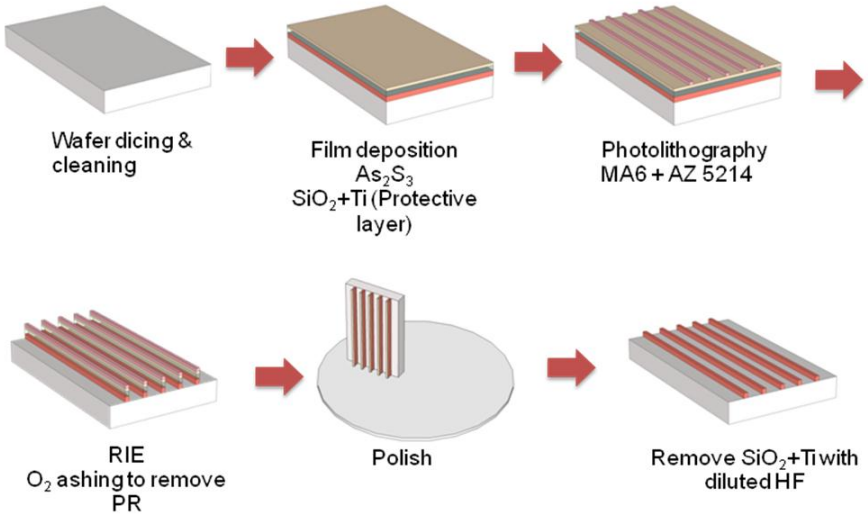

Fig. 41. Fabrication process of As_2S_3 waveguides.

Waveguide fabrication begins with dicing a wafer into square samples. The $LiNbO_3$ wafer, supplied by Crystal Technology Inc (Palo Alto, CA), is 3 inch in diameter, 1 mm in thickness, placed in x-cut, y-propagation manner. There are three standard sample sizes: 23 mm×20 mm, 11 mm×20 mm and 42 mm×17 mm. Then the sample is cleaned consecutively by soapy water, acetone ($(CH_3)_2CO$), Isopropyl alcohol (IPA, C_3H_8O), De-Ionized (DI) water and methanol (CH_3OH). Acetone, IPA and methanol are good organic solvents: acetone is widely used for its excellent cleaning capability in laboratory; IPA is also known as rubbing alcohol for it is suitable for rubbing the surface with Q-tips; methanol is light and volatile that dissolves water and evaporates rapidly, leaving no residue. After cleaning the sample is loaded into a Radio Frequency (RF) magnetron sputter system to deposit a thin film of As_2S_3.

There are mainly four methods to prepare As_2S_3 film: spin coating, thermal evaporation, pulsed laser deposition and RF sputtering. Spin coating is a cost-effective method, in which As_2S_3 solution needs to be made at first. Because As_2S_3 solution can easily be oxidized into As_2O_3, a highly toxic substance when exposed to air, the processing needs to be done under the vacuumed hood. Thermal evaporation and pulsed laser deposition are widely used by some researchers, such as Center for Ultrahigh-bandwidth Devices for Optical Systems (CUDOS) in Australia, since the melting temperature of As_2S_3 is quite low (300 ℃) compared to oxide glasses (Table II). They found that after film deposition, annealing has to be carried out so as to stabilize the refractive index of deposited As_2S_3 film; otherwise, it may change as sub-bandgap wavelength light shines on it. That is known as the photo-darkening effect, which is not necessarily a bad thing, some waveguides can be made through that effect actually [30]. In sputtering method, in which As_2S_3 is exposed to radiation in the plasma during deposition, the deposited film has already been stabilized. So no extra annealing is needed after deposition. Furthermore, our experience suggests that sputtered films are denser, and are generally better adhered to the substrate, due to the higher bombarding energy than others [23].

For an RF sputtering system, the magnetron can be used to confine electrons and elongate the electron path by making it spiral, so that the density of the plasma is increased. Consequently, there is more ionization and more ion bombardment. As a result, we will have a higher deposition rate, a lower workable pressure and a lower operation voltage. In addition, since the electrons are trapped near the cathode, they are

kept away from the anode surface, where the sample is mounted. So there are less electron bombardments on the As_2S_3 film and less additional heat generated. That is an important merit for us, since the glass transition temperature of As_2S_3 is only 180 ℃ (Table II).

Table II. Selected thermal properties of As_2S_3.

As_2S_3	Temperature
Melting Point	300 ℃
Glass Transition	180 ℃
Annealing	170 ℃

The color of the film after deposition appears yellow. An orange color means a thick film while the light yellow color suggests a low thickness. If the color turns out to be white, it is an indication that the film has been oxidized. Probably, there is air or water leak in the chamber. The process has to be stopped until the problem is found and solved. The As_2S_3 target is supplied by Amorphous Materials Co. (Garland, TX).

Then the sample is transferred into an electron beam evaporator to deposit a layer of silicon dioxide (SiO_2) and titanium (Ti). They act as a protective layer to prevent As_2S_3 from being exposed to air and protect it from being dissolved by commercial NH_4OH-based developers, which can cause formation of pinholes and peeling of the film [7].

Prior to the evaporation, the sample holders are cleaned with a sand blaster and the bell jar is heated to remove the water vapor from the chamber wall. To ensure the

mean free path is long, the deposition is done in high vacuum— the base pressure is about 10^{-7} Torr. During the electron beam evaporation, the planetary motion is used to improve the uniformity of the film. To avoid the problem of condensation and spattering at high deposition rate, the deposition rate is controlled to be slow, about 3-5 Å/sec. A quartz crystal monitor is used to monitor the thickness of deposited film. SiO_2 alone is found to be insufficient to resist the attack by alkaline based developers. Chrome (Cr) can be used instead of titanium as the upper protective layer if necessary.

The thickness of As_2S_3 is 2 μm, and that of SiO_2 and Ti are 180 nm and 30 nm, measured using Filmetrics F20, a reflective spectroscopic method. It is composed of a tungsten-halogen bulb as a white light source (400 nm - 3000 nm), a diffraction grating to spatially distinguish different wavelengths and a linear photodiode array to detect the light intensity at each wavelength. The Filmetrics is also used to measure the optical constants, such as the complex refractive index of deposited film, including both the real (n) and imaginary part (k). Since birefringence cannot be easily modeled by the Filmetrics, silicon dummies are used instead of the real $LiNbO_3$ sample.

Prior to sample measurement, a reference sample is measured as the baseline first to take into account the response inherent to the equipment, i. e. to calibrate the spectral response of the system. A dark reading is then taken to measure the magnitude of the dark current for a given integration time so later it can be subtracted. The principle of Filmetrics is to measure the interference pattern generated by the reflected (or transmitted) light from the sample, construct a model of the film stack by the initial guess so that a reflection spectrum can be calculated, and adjust the parameters in the

model to obtain a good fit between the calculated spectrum and the measured spectrum. Therefore, in order to efficiently and precisely measure the film using Filmetrics, it is critical to make the initial guess and to set the searching range.

In photolithography, a layer of widely-used positive photo-resist AZ 5214 E IR (produced by Clariant) is spun on the sample. The rotation speed is 7000 RPM and the spinning time is 40 seconds, with a 5 second acceleration/deceleration time. After soft-bake on a hotplate at 125 ℃ for 1 min, the sample is loaded onto a MA6 aligner. It is a contact I-line aligner, which allows using 6 inch mask and has a 3 inch by 3 inch exposure area. The normal exposure intensity is around 7 mW/cm^2 and the exposure time is about 12 seconds so that the average dose is more or less 80 mJ/ cm^2. After that, it is developed in MF 312 solution (1:1.2) for about 50 seconds. A high magnification (1000X) optical microscope with scales (0.625 μm/division) is used to check that the dimension of the pattern after development agrees with the design, so as to confirm the exposure and developing conditions are good. Then the sample is baked in an oven at 135 ℃ for 30min to harden the photo-resist for standing the following etching process.

It is found that dry-etching is advantageous over wet-etching in obtaining smooth sidewalls and controlling the waveguide dimensions [22], because the process of wet chemistry suffers from slanted sidewalls by undercutting of the mask layer. In order to get good waveguide surface and side walls, the sample with As_2S_3- SiO_2-Ti-Photoresist stack on it is etched through in an Oxford inductively coupled plasmas (ICP) reactive-ion-etch (RIE) system (Fig. 42).

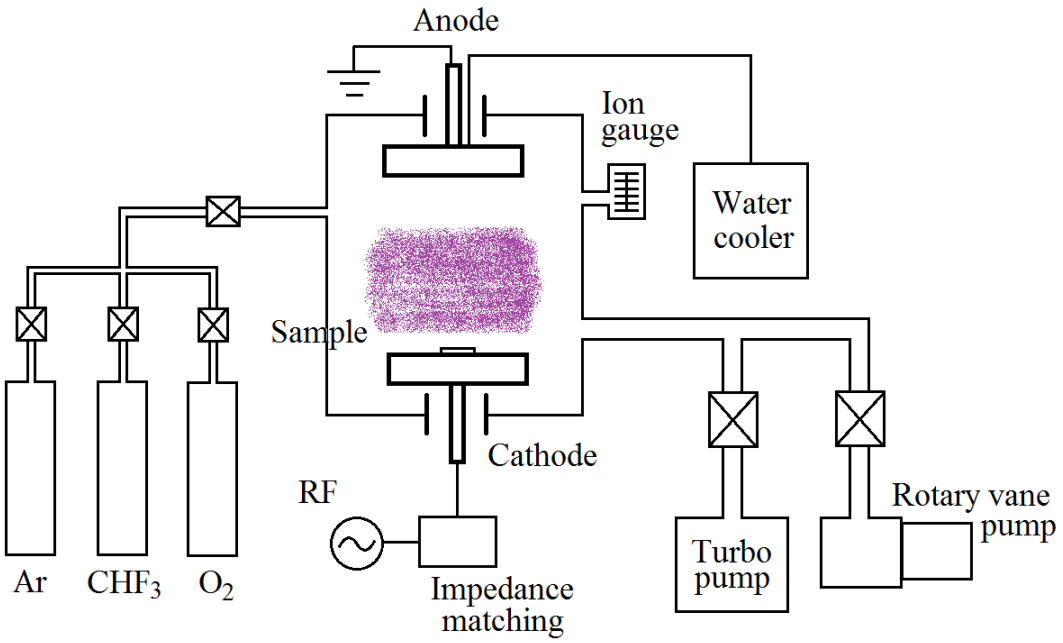

Fig. 42. Configuration of Reactive Ion Etching system.

Reactive ion etching is a type of plasma etching, in which the plasma provides the energy to overcome or lower the activation barrier. The etching process consists of inert ion bombardment, also called physical sputtering, and reactive ion bombardment, known as chemical reaction. The reactive ions bond with atoms and create volatile species while the inert ion bombardment breaks and dislodge them. The inductive coils in the system are used to inductively couple the power into the plasma so that the ionization is increased and so is the plasma density. So there are more reactive radicals and more ion current. As a result, samples have less damage but higher etching rate, and etching can be done at a lower voltage while at the same power.

CHF_3 is used for chemical reaction and Argon for physical sputtering, as shown in Fig. 43. The product AsF_x and SF_x are highly volatile materials that can be removed

easily. Argon is also known as an inert gas that can promote the plasma stability. Fluorocarbon polymer forms a passivation layer on sidewalls to promote etching directionality. It is reported that CHF_3 has a better polymer passivation on etched surface than CF_4, giving a smoother surface and sidewall profile.

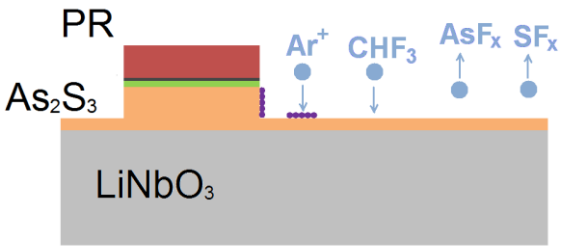

Fig. 43. Reactive etching process.

Because $LiNbO_3$ substrate is nonconductive, it suffers from charging effect, which causes two problems. First, it is difficult to get clear Scanning Electron Microscope (SEM) images, especially under high magnification. In most cases, silicon dummies are used in recipe development. Second, charging effect can cause undercut if over-etched (Fig. 44).

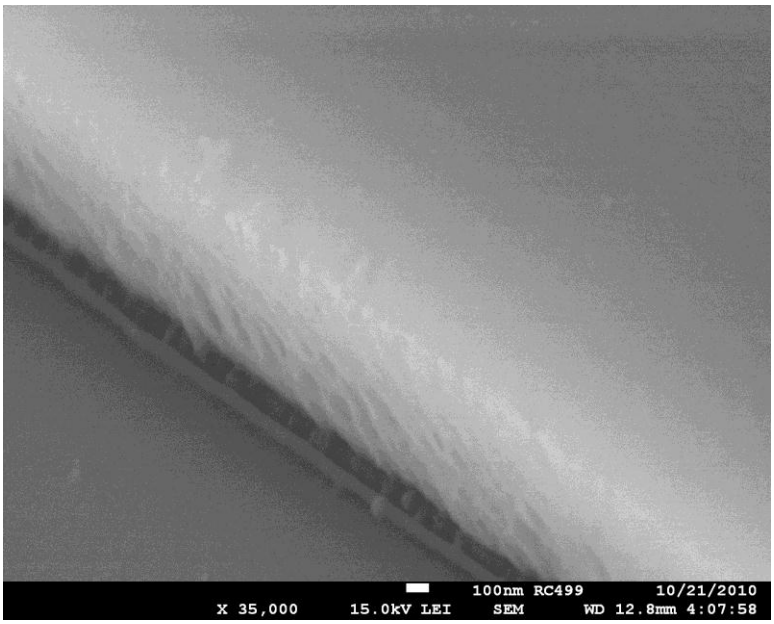

Fig. 44. SEM picture of undercut.

The mechanism of undercut can be explained using the etching of Silicon on Insulator (SOI) structure, shown in Fig. 45. As etching of silicon is close to completion, the surface of dielectric silicon dioxide is exposed. Argon ions impinge on the surface and the positive charges stay there because it is non-conductive. If etching continues further, incoming argon ions will be repelled by the positive charged surface and deflected to the foot of originally protected silicon structures, causing undercut.

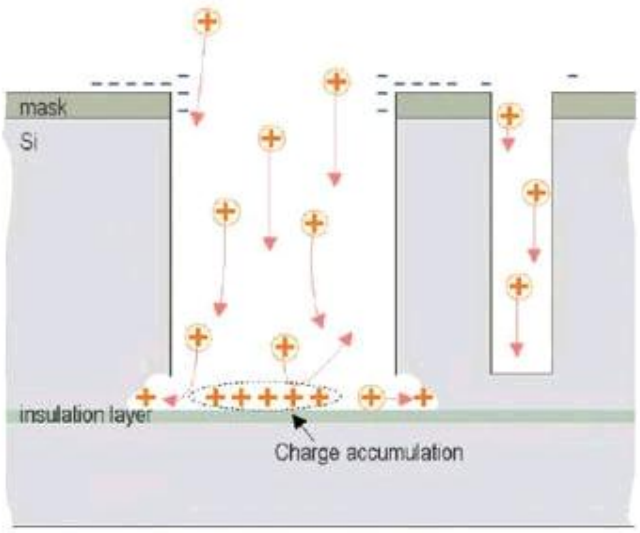

Fig. 45. Mechanism of undercut on SOI.

Therefore, to prevent undercut, etching time needs to be precisely controlled and etching rates characterized. Due to the macro-loading effect, smaller samples etch faster than larger one. So sample sizes are standardized (11 mm by 20 mm, 23 mm by 20 mm and 42 mm by 17 mm). The micro-loading effect is not a great concern for us since our pattern is generally uniform.

Although $LiNbO_3$ is a well-known difficult-to-etch material, over-etching on the sample still causes unwanted roughness that induces loss. To reduce the risk of etching into substrate, less argon is used, since argon is observed to have a much higher etching rate to $LiNbO_3$ than CHF_3.

It is also found that the removal rate of atoms of As and S from the surface are not same: due to As-As and S-S bonds in the amorphous glass, As_2S_3 surface will

become rough during etching. However, this roughness disappears as the etching of As_2S_3 completes [43].

To improve sidewall roughness, a lot of control experiments are done and finally we found that higher ICP power and lower processing pressure helps a lot. Studying the mechanism of RIE helps us to understand that, by using high power ICP, we increase the plasma density. Together with the low processing pressure, ion-to-gas molecule ratio increases so that ion scattering by gas is reduced. As a result, the general trend of ion trajectory becomes more vertical. And the sidewall etching is significantly reduced. Furthermore, the roughness on the photo-resist can be transferred into waveguides during etching, which can be alleviated by hard baking the sample for a longer time to make the resist reflow.

Resist thermal reflow is originally a technique developed in Integrated Circuit (IC) fabrication industry. The photo-resist is re-shaped by baking it above the liquid-glass transition temperature after development [44]. As a supplement to other optical extension methods for contact lithography, it is used to make smaller contact holes [44]. Several factors need to be considered in order to successfully apply the photo-resist using thermal flow process, such as flow rate, depth of focus (DOF) and Post Exposure Delay (PED) stability [45]. However, the case is much simpler for us since we only need to reduce the sidewall roughness of the photo-resist. Experimental results show that a prolonged hard-bake time serves that purpose well, as shown in Fig. 46.

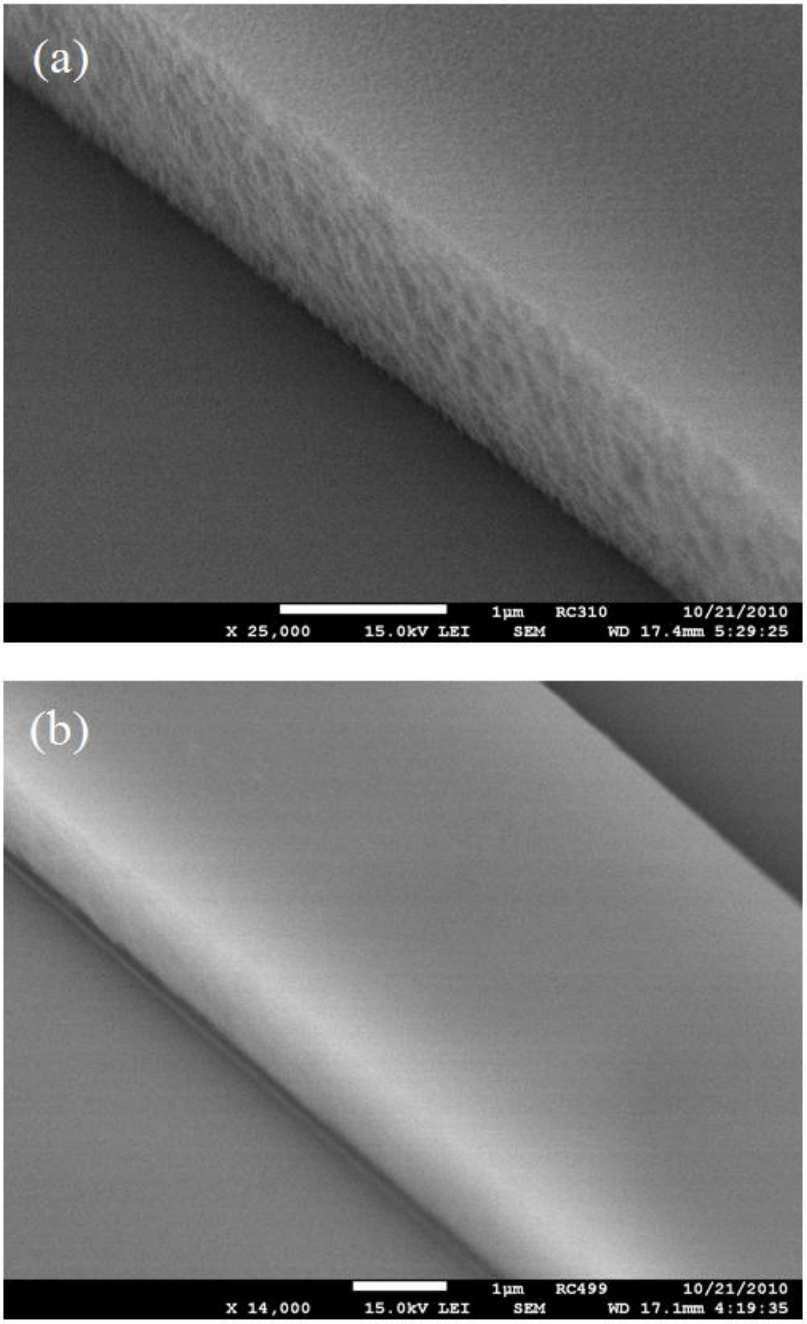

Fig. 46. Waveguide sidewall after hardbake for 10 min (a) and for 30 min (b).

As a result, the sidewall roughness is improved substantially. Using the RF power of 40W and ICP power of 300W, the etching rate of As_2S_3 is estimated to be 500 nm/min and for SiO_2 is 65 nm/min.

For optical waveguides, the smoothness of the end-facets is very critical to coupling, and as a result to the total insertion loss. Polishing is a widely used approach to solve it. The established polishing method for $LiNbO_3$ is adapted for polishing As_2S_3 waveguides on $LiNbO_3$ substrate. The sample is clamped in an aluminum chuck, and the whole work-piece is polished on a series of rotating diamond films of grain size 15 μm, 3 μm, 0.5 μm successively and finally a high optical grade end-facet is achieved. However, As_2S_3 is a brittle material and after the traditional method of polishing, most As_2S_3 waveguides have chipped ends, as Fig. 47 shows. Rarely, cases are seen of peeling, showing a rainbow color on edges.

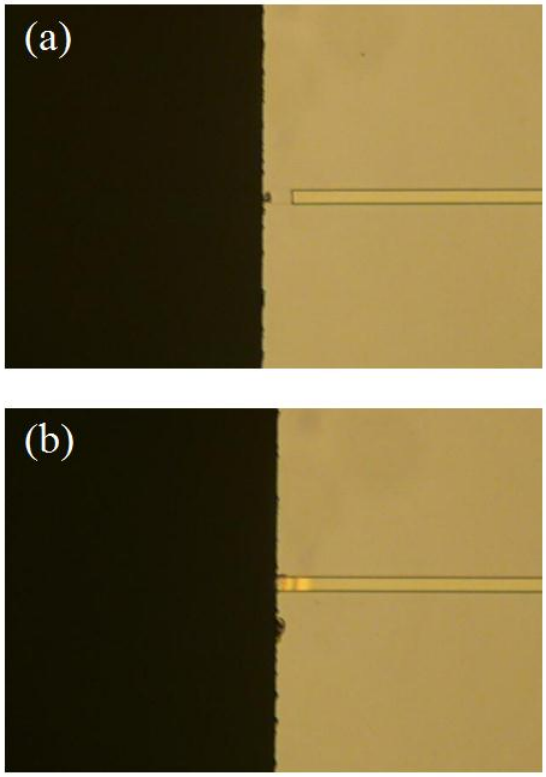

Fig. 47. Polished results: break (a) and peeling (b).

In order to understand the problem, the mechanics of materials and polishing are studied and the stress-strain curve for As_2S_3 and $LiNbO_3$ is constructed (Fig. 48). Stress is the force applied upon the material and strain represents the micro physical displacement within the material. Polishing, essentially a micro-edge cutting processing of many random grains, is most effective when in plastic cutting removal mode [46], the green curve region. Tensile strength is defined as the critical strength of the material, beyond which, the material breaks.

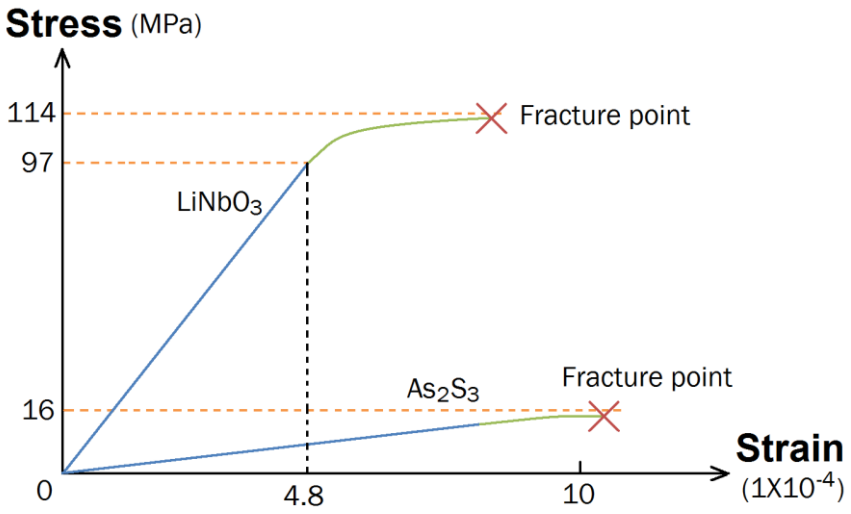

Fig. 48. Stress-strain curve for As_2S_3 and $LiNbO_3$.

From the curve in Fig. 48, we can see that As_2S_3 has a much lower tensile stress and effective polishing stress than $LiNbO_3$. So a lower pressure is applied for polishing As_2S_3 after polishing the $LiNbO_3$ substrate first. A list of mechanical properties of the materials is shown in Table III.

Table III. Mechanical properties of certain materials.

Material	Hardness	Young's Modulus	Tensile Strength
$LiNbO_3$	5	203 GPa	114 MPa
Quickstick 135 Wax	"Very high"	Not found	80-134 Mpa
SiO_2	5.4	74 GPa	68 MPa
As_2S_3	2.75	16 GPa	16 MPa
PR (SU-8)	4	2 GPa	73 MPa

Young's modulus represents flexibility of the material. The smaller that value, the higher the flexibility is. In order to protect As_2S_3 waveguides, high strength but less flexible material is preferred. Although the model above is very simplified and the real situation is much more complicated, it helps us to understand and find a solution.

Material such as photo-resist, SiO_2, and wax are used for protection. Polishing using two samples face-to-face instead of one, single sample are tried. For processing, different rotation speeds and pressure are experimented with. It is found that for polishing single samples, SiO_2 is much better than photo-resist, and through Plasma Enhance Chemical Vapor Deposition (PECVD), SiO_2 has the best quality among them. In bonded sample pair polishing, wax gives the best result, and it is even better than using SiO_2 on single sample polishing. The reason is probably that it provides a better protection on adherence.

At last, an optimized polishing recipe is developed: put two samples face to face and bond them with wax, polish the end-faces consecutively on the rotation plates of 15 μm, 3 μm and 0.5 μm with the optimized speeds, separate and clean them afterwards. The improved result is shown in Fig. 49.

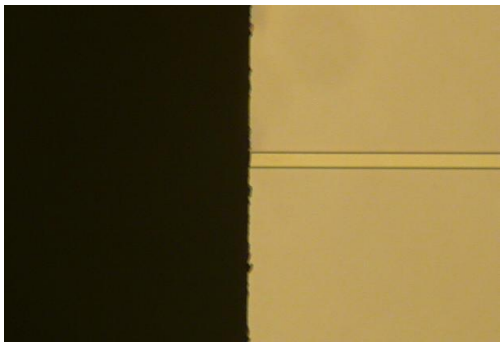

Fig. 49. Good polished result.

The protective film of SiO_2 and Ti was then removed by the diluted HF solution (HF: H_2O= 1:30) at last. The microscopic picture of waveguides after fabrication is shown in Fig. 50 and SEM picture in Fig. 51.

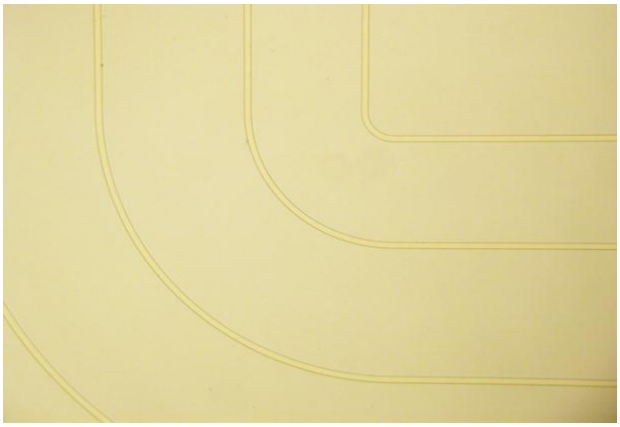

Fig. 50. Microscopic picture of As_2S_3 waveguides.

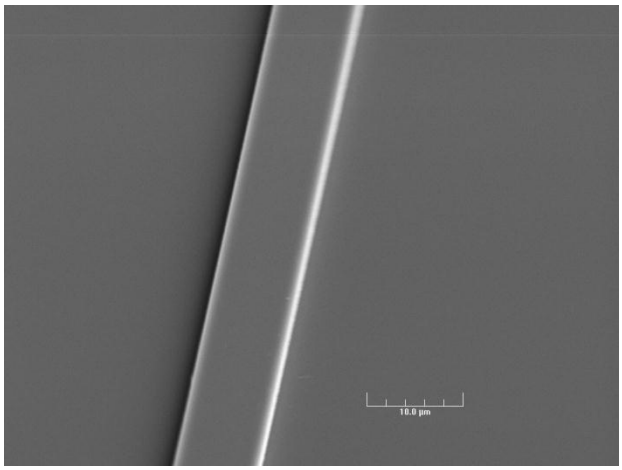

Fig. 51. SEM picture of As_2S_3 waveguide.

4.2. Integrated polarization converters on Ti: $LiNbO_3$

The fabrication of electro-optical devices on Ti: $LiNbO_3$ waveguide consists of two parts: the low-loss, single mode titanium diffused waveguides in the lithium niobate substrate for wave guiding and the buffer-electrode structure for electrical tuning. Another popular way of making titanium waveguides on lithium niobate substrates is by proton exchange, which cannot be used here, since it only creates controllable refractive index change for extraordinary index and thus only supports TE polarized modes for x cut.

Similar to the fabrication process of As_2S_3 waveguides, the sample is first diced from a lithium niobate wafer using a dicing saw, and then cleaned with soapy water, acetone, IPA, DI water and methanol. Then a thin film of titanium is deposited using Direct Current (DC) sputtering system. The configuration is shown in Fig. 52.

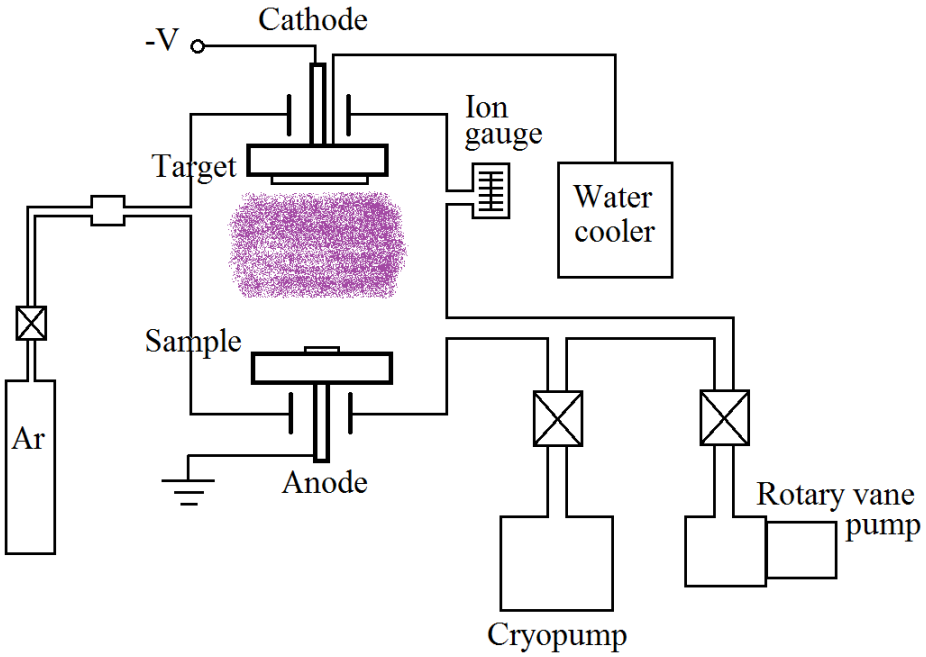

Fig. 52. Configuration of DC sputtering system.

Sputtering is a non-equilibrium, momentum transfer process for thin film deposition. Compared to titanium deposition using electron beam evaporation, it gives a titanium thin film that has higher density and better adherence to the substrate. The configuration of a DC sputtering system includes two parallel cylindrical plates, as shown in Fig. 52. There are two electrodes: one is cathode, on which the target material is mounted and the other is anode, where the sample is placed. Both of them are water cooled. Once the sample is loaded on the anode, the chamber is pumped down by a two stage pumping system, first a mechanical pump for rough pumping to 100 mTorr, then a cryo-pump is used to pump the chamber down to 10^{-6} Torr, which is the base pressure. When the chamber is open for loading the sample, water vapor enters and attaches to the wall, so it is necessary to heat the bell jar to get rid of it during high vacuum pumping.

After the base pressure is reached, argon gas is flowed into the chamber at a rate of 140 sccm, stabilizes for 15 min and then the vacuum valve is closed to a certain degree that allows argon gas to accumulate, forming a pressure of 20 mTorr. Next a high voltage is applied to the cathode, resulting in an electric field between the two parallel plates. In the strong electric field, the movement of electrons accelerates and they hit argon atoms, which causes the argon atom to ionize:

$$e^- + A \rightarrow 2e^- + A^+ \tag{4.1}$$

As equation (4.1) shows, along with a positively-charged argon ion created, another electron is generated. That electron moves and may cause ionization of another argon atom. Such a process continues and is called ionization cascade. As a result, a self-sustained plasma is ignited: electrons and ions escape from the plasma to hit the anode and cathode while new electrons and ions are generated by ionization cascading. And a purple glow can be seen due to the decay of the energetic argon species.

The larger the distance between the electrodes, the higher the plasma breakdown voltage is. Therefore, the distance between the two electrodes should be small, but it has to be long enough for electrons to gain energy. In practice, it is about 10 cm. In addition, the cathode needs to be big enough to prevent loss of electrons.

Since there is an electric field between the two parallel plates, electrons and argon ions escape at the boundary of plasma body, and electrons escape more rapidly than ions since their mass is much smaller. Consequently, the plasma body becomes positively charged. Inside the plasma body, it is a perfect conductor, that is, it is equi-

potential. So all potential drop between the two plates is across the sheath near each electrode, as Fig. 53 shows.

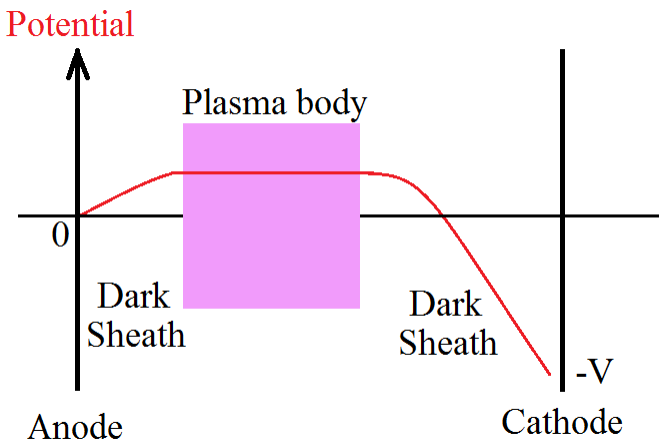

Fig. 53. Potential of plasma.

At the cathode, the escaped ions are accelerated by the sheath and hit the target. Those ions that have kinetic energy between 10 eV and 10 KeV break the bonds in the target atoms on the surface, physically displace them and eject the atom clusters out, which are a neutral species and travel through the plasma and deposit on the sample. That is the basic principle of sputtering deposition. At the anode, which is grounded, as the plasma body becomes positively charged, a potential barrier develops to suppress the electron escape.

In order to clean the source and getter the residual gas, a 15 min to 30 min pre-sputtering is done. After that, the real sample is rotated out on a holding plate and exposed to the plasma. The voltage at sputtering is about 4000 V. It is estimated that

75% of the heat is generated at the target while 25% goes to substrate. To prevent overheating of the target and substrate, water cooling is employed.

From many experimental results, the optimum thickness is 135 nm for fabricating titanium diffused waveguides working at the wavelength of 2.05 μm. The color of deposited titanium film should appear silver. If it is slightly brownish, it is the color of titanium nitride; the amount is so small that it is not a big concern. If the film appears blue, it is a strong indication of titanium oxide, which can be caused by leak of the chamber during sputtering, or virtual leaks inside the chamber. Although in the diffused process the titanium becomes oxidized after all, it renders the control of the amount of Ti we deposit on the sample difficult. So it should be avoided and the problem needs to be found and solved.

Next, the titanium waveguide pattern is transferred from the mask to the photo-resist through contact I-line photolithography with positive photo-resist AZ 5214 E IR. By wet etching using diluted hydrofluoric solution or dry etching using oxford RIE system, the pattern is then transferred into the titanium film. Since the pattern is relatively large, wet etching can also yield a good result. After removing the photo-resist through photo-resist stripper AZ 300T (from Clariant) or oxygen ashing using RIE correspondingly, the height of the titanium strips is measured by Dektak 3 profilometer, in order to precisely estimate the diffusion time.

Dektak 3 profilometer is a contact stylus surface profiler. It works by first lowering a diamond-tipped stylus onto the sample, and then slowly moves the sample beneath the stylus, so that the topology of the sample surface is transferred into the

vertical movements of the stylus, which are sensed by a transducer, and the electrical signal is digitized and sent to a computer. Therefore, to reduce the vibration and noise, an air cushion is used.

The sample is then placed in a high temperature diffusion furnace. The sample holder is made of alumina and the tube is made of quartz so that they can stand the high diffusion temperature. For titanium diffused waveguide, the optimum temperature is 1025 ℃. And the diffusion takes 13 hours 30 minutes at the rate of roughly 10 nm/hour, plus 1 hour and 15 minutes temperature ramping time. And it cools down slowly to room temperature after about 6 hours. A constant wet air flow is used: the compressed air flows out of the gas tank, through a beaker of water, and then through the quartz diffusion tube. The flowing rate is optimized to get the smoothest surface after diffusion. The purpose of the wet air flow is to provide an increased oxygen partial pressure that suppresses the observed lithium oxide (Li_2O) out-diffusion [47], which can create an undesirable lateral surface guiding layer. Later it is found that, using a hotplate to heat the wet air to 75 ℃ before letting it go into the quartz tube helps to get a smooth surface [43]. It is found that the diffusion profile of titanium is a Gaussian distribution in the lateral direction and a Hermit-Gaussian distribution in the vertical direction.

Since at this time the edges of the sample are rough, if it goes to optical testing now, the coupling loss would be so large that no significant result could be obtained. So the sample is polished on a Struers polishing machine with the procedure mentioned earlier: it is first clamped in an aluminum chuck, and two end-facets are then polished on

a series of rotating diamond films of grain size 15 μm, 3 μm, 0.5 μm successively and the rotation speeds are optimized. Water is used as the coolant. For smaller grain size, lower speed is generally preferred. Finally a high optical grade end-facet is achieved and titanium diffused waveguides are made.

In order to insulate the electrodes from titanium diffused waveguides, a buffer layer is needed. Silicon dioxide, due to its excellent dielectric property, is chosen as the buffer material. Various deposition techniques are evaluated experimentally. With the silicon dioxide deposited using electron beam evaporator, the fabricated polarization converters fail to work. The reason is suspected to be the surface charge between the $LiNbO_3$ surface and silicon dioxide film and the poor quality of electron beam evaporated SiO_2 film, due to the contamination from metals such as Au, Ti, Cr (the electron beam evaporator is one of heaviest used equipment in the lab) and the low deposition energy since electron beam evaporation is actually an equilibrium process.

With RF sputtered silicon dioxide followed with 30 minute 900 ℃ annealing, we are able to get good results. The deposition energy of RF sputtering is much higher so a denser SiO_2 film is obtained, and a 30 minute annealing at a temperature of 900 ℃ eliminates the surface charges. The resistance measured between contact pads is a good indicator of the insulating property of the SiO_2 as a buffer layer. After RF sputtering, it is around 20 KΩ while after annealing it is 130 KΩ. The thickness of silicon dioxide is 180 nm.

Sputtering, as mentioned above, is a non-equilibrium process and the energy is 10-50 eV per atom, which is much higher than that of electron beam evaporation, 1 eV per atom. With higher energy, the atoms have higher mobility and move around after arriving at the sample surface to form a denser film. So it is a preferred method to electron beam evaporation in order to get a high quality film. However, for depositing dielectric materials such as SiO_2, the RF power source must be used instead of a DC supply, to eliminate the charge built-up problem. Because dielectric materials such as SiO_2 are not conductive materials, when argon ions hit the SiO_2 target their positive charges stay there, which resist the electric field exerted by the two electrodes. If no measure is taken, as the charge build up continues, it will finally cancel the potential difference that the plasma experiences, causing it to diminish. If an alternating voltage is applied, at the negative half cycle, the polarity of the electrodes switches. The target becomes the anode, and electrons are attracted to neutralize the positive charges on it, so that the plasma and glow charge sustain and the sputtering continues.

The frequency of the alternative electric field is set to be 13.56 MHz, mainly due to historical reasons. At such high frequency, the electrons neutralize the positive charge build-up while the ions no longer follow the switching because of their larger mass-to-charge ratio. The frequency cannot be too low: if it is lower than 50 KHz, both electrons and ions follow the switching of anode and cathode, and it is basically a DC sputtering of both surfaces.

In the alternating electric field, the RF plasma can be seen as a partially resistive and partially capacitive load. In order to maximize the transmitted power and minimize

the reflected power, an impedance matching network is required to match the impedance of the load to that of the generator (50 Ω), as Fig. 54 illustrates.

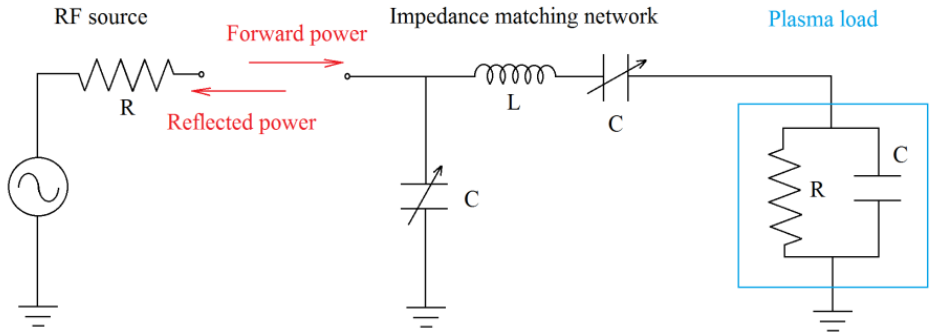

Fig. 54. Impedance matching network.

Besides argon (flow rate is 30 sccm), a small amount of oxygen (2 sccm) is also introduced into the chamber for deposition, known as reactive sputtering, so as to make the composition of the deposited silicon dioxide film right. The RF power is set to be 400 W, and the self-bias of the cathode is 1.4 kV. The base pressure is 4×10^{-6} Torr while the processing pressure is 18 mTorr. The deposition rate is 50 Å/min. Similarly to DC sputtering, water cooler is used to prevent the sample and the target from overheating.

Annealing is done in the diffusion furnace with a constant flow of compressed air. The temperature is set to be 900 ℃ and the annealing time is 30 minutes, plus a 1 hour 15 minutes temperature ramping time. During the annealing, the silicon dioxide and the lithium niobate mutually diffuse into each other and so do the surface charges, which are then trapped.

Next a layer of aluminum is evaporated with an electron beam evaporator, with a thickness of 200 nm. Then the sample goes through a similar photolithography process for patterning the electrodes as patterning the titanium film.

To etch the aluminum, an off-the-shelf aluminum etch is used, which consists of phosphoric acid, nitric acid, acetic acid and water with the ratio of 16:1:1:2. The etching generally takes 4 minutes and 30 seconds. After that, the photo-resist is removed by immersing the sample into the acetone, since the MF 312 based photo-resist developer can etch aluminum undesirably. Then the sample is ready for optical testing. The process is summarized in Fig. 55.

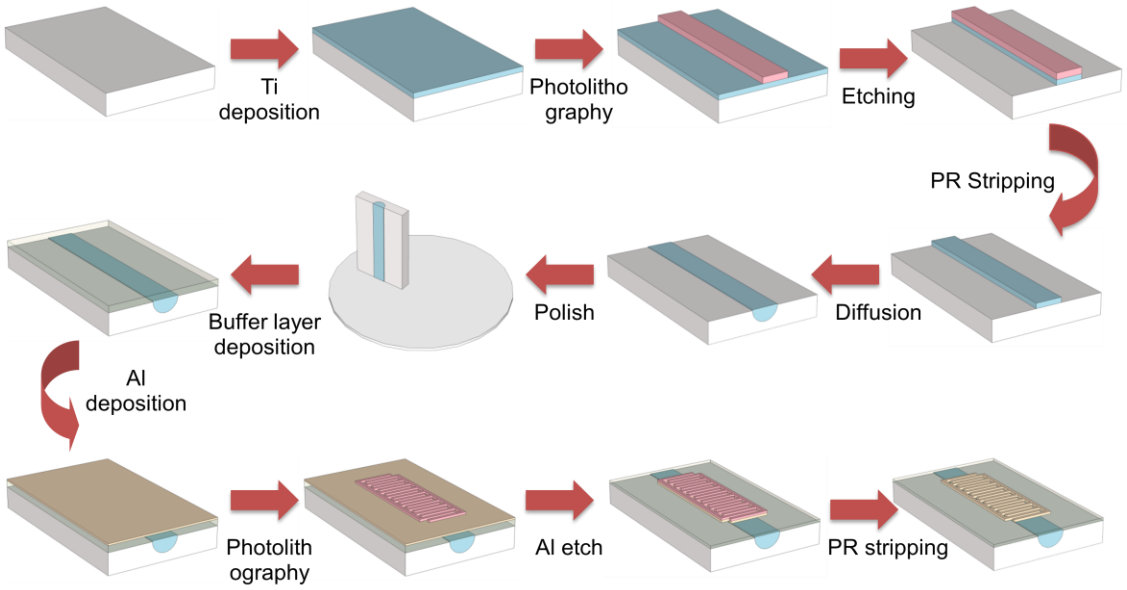

Fig. 55. Fabrication process of integrated polarization converter.

The pictures of fabricated samples under microscope inspection are shown in Fig. 56: the bright patterns are aluminum electrodes while the narrow parallel lines shows the boundaries of titanium diffused waveguides.

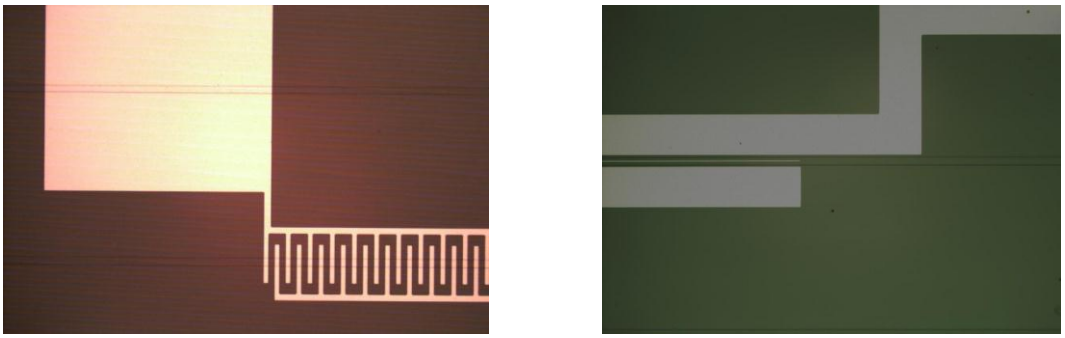

Fig. 56. Microscopic pictures of fabricated polarization converters.

4.3. As_2S_3-Ti: $LiNbO_3$ taper couplers

The As_2S_3-Ti: $LiNbO_3$ taper coupler is fabricated using photolithography and dry-etch technology. The substrate $LiNbO_3$ is a birefringent crystal with refractive index n_o=2.2119 and n_e=2.1386 (λ=1531 nm), placed in x-cut, y-propagation manner. Similar to the first step for making integrated polarization converters using Ti: $LiNbO_3$, the titanium diffused waveguide is fabricated through sputtering of a 95 nm thick titanium layer, patterning into 7 μm wide strip with photolithography and reactive ion etching (RIE), diffusion for 9 hours at 1025 ℃ and optical polishing on end-facets.

The fabrication of As_2S_3 waveguide follows the similar recipe for making stand-alone As_2S_3 waveguides, except for polishing. A layer of 0.47 μm thick As_2S_3 film is deposited on the titanium waveguide sample using an RF sputtering system, along with a

protective layer of SiO_2 and Ti, which protects the As_2S_3 from being dissolved by commercial alkaline-based developers.

Photolithography is the key to fabricating nicely shaped taper couplers to make sure the fabricated devices agree with the design, since the width of the waveguide is relatively small—only 3.5 μm, and more importantly, the tip width is only 1 μm.

Many experiments on contact photolithography using the MA6 at TAMU were carried out. It is capable of producing patterns as small as 1.0 μm theoretically, exactly the size of the taper tip. However, in practices, it is hardly feasible. SEM pictures show that the fabricated tip widths are usually larger than 1.4 μm, and deformed waveguide segments can be seen from time to time (Fig. 57).

Alternatively, a projection photolithography is carried out using a stepper at Penn State University. The minimum feature size it can produce is 0.6 μm, therefore the 1.0 μm wide taper tip can be assured in photolithography. Nevertheless the subsequent hardbake causes an expansion to a certain degree (Fig. 58). After that, the Ti-SiO_2-As_2S_3 stack is etched through to the substrate by RIE. And Ti-SiO_2 is removed in diluted hydrofluoric solution at last.

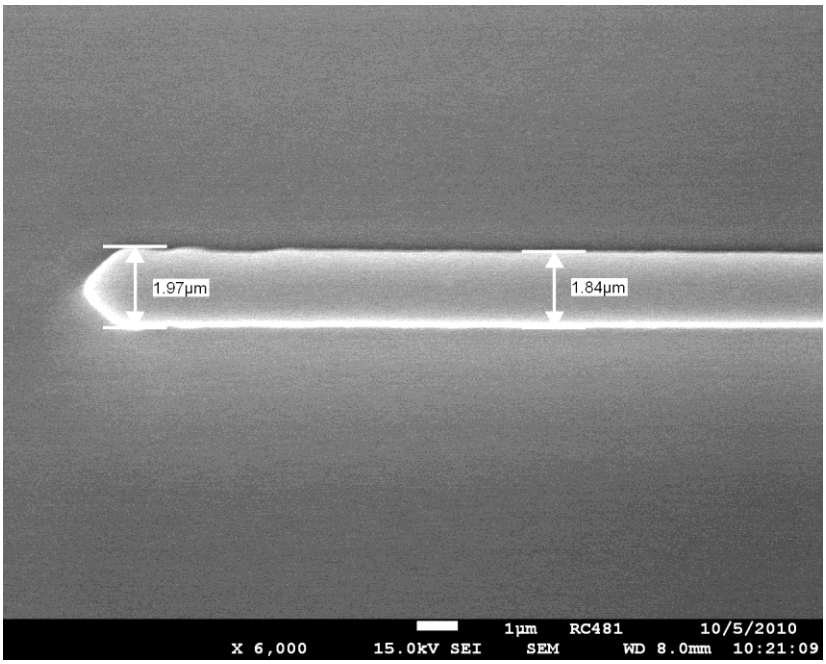

Fig. 57. Sample fabricated using contact photolithography.

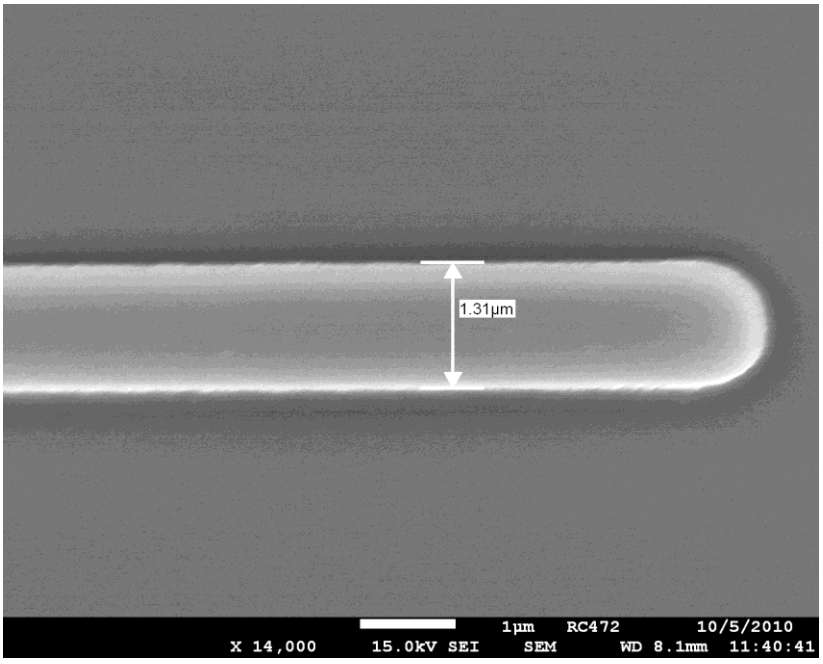

Fig. 58. Sample fabricated using projection photolithography.

The hardbake time is prolonged in order to obtain smoother sidewalls by the resist reflow process (please refer to the section of mid IR As_2S_3 waveguide fabrication), which, however, causes an expansion of As_2S_3 waveguide to a certain degree, up to 0.5 μm. The average tip width of tapered As_2S_3 waveguides after fabrication is 1.3 μm, as shown in Fig. 58. Depending on the process conditions such as exposure and development, it can be smaller or larger than that.

CHAPTER V

MEASUREMENTS AND RESULTS *

Two sets of optical measurement setups are built to characterize the waveguides and devices. One is a free-optics based setup using a quantum cascade laser at the wavelength of 4.8 μm in Dr. Craig Arnold's lab in Princeton University. We collaborate with Dr. Arnold's group on studying mid IR waveguides. The quantum cascade laser is made by Dr. Claire Gmachl's group, as a product of a research project on pulsed QC lasers. The other one is a fiber based setup built in our lab at Texas A&M University. The measurement setup has the capability for characterizing waveguides and devices at the wavelength of 1.55 μm and of 2.05 μm.

5.1. Mid IR As_2S_3 waveguide characterization

The As_2S_3 waveguides are characterized on the Princeton setup. The measurement setup is composed of a pulse generator, a single mode quantum cascade laser (QCL), a doublet of ZnSe lenses, a liquid nitrogen cooled HgCdTe detector (MCT), a pre-amplifier and a 7260 DSP lock-in amplifier from EG&G instruments. The schematic and picture of the configuration is shown in Fig. 59. Mid IR light at the wavelength of 4.8 μm is emitted from the QCL, and then butt-coupled into the waveguide, as shown in Fig. 60. Supplied at the voltage of 50 V, the laser works at the frequency of 80 kHz, has a pulse width of 100 ns and a peak power of 0.2 W. From the output end of the waveguide, the light propagates through free space and then is collected and focused by a ZnSe doublet (two lenses of focus lengths 3 cm and 1 cm respectively) into the MCT. The lock-in amplifier is used to enhance the detection of weak signals.

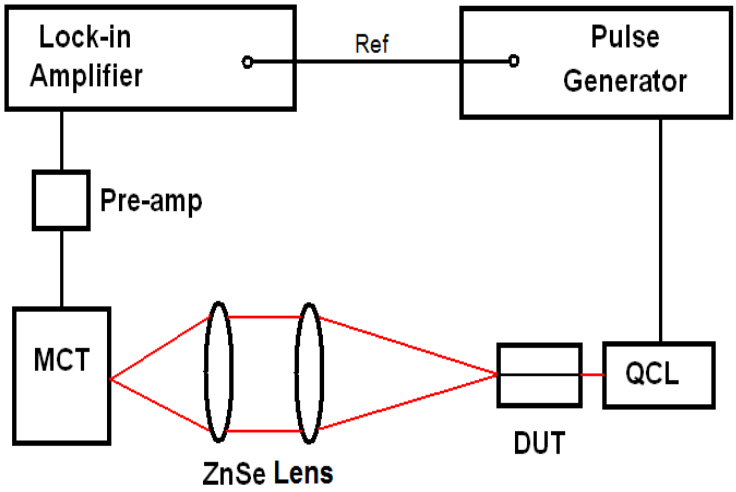

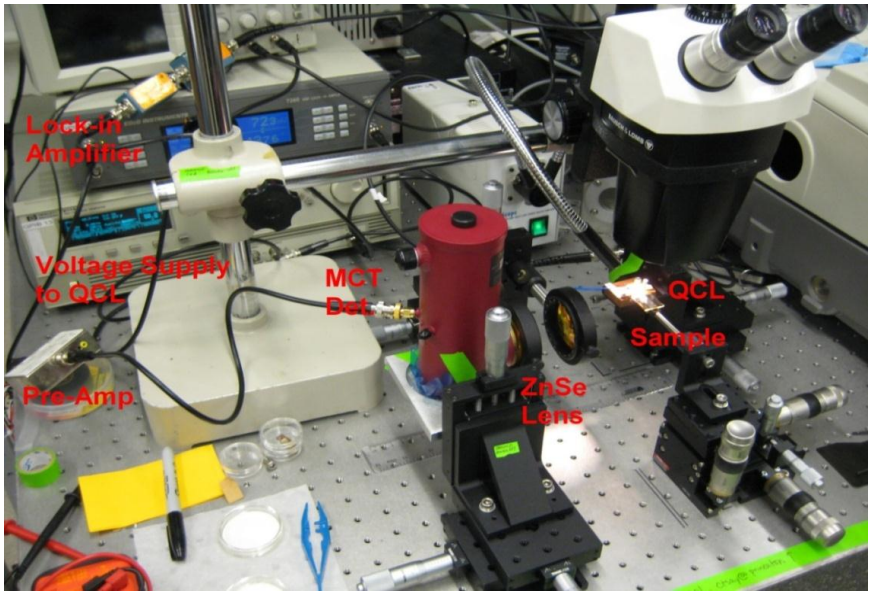

Fig. 59. Measurement setup in Princeton University.

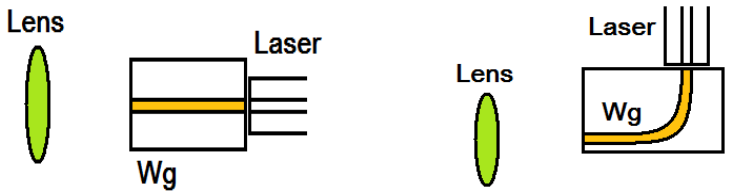

Fig. 60. Configuration of QC laser and the waveguide.

The best insertion losses of straight waveguides measured are 3.81 dB (14 mm long) and 4.27 dB (21 mm long). The results in Fig. 61 show a slight change of insertion loss as the width of the waveguide varies. The peak appears at the width of 11 μm, which is reasonable considering the fact that the width of the laser active region is 10 μm. And it also qualitatively agrees with the simulations. If the width of the waveguide is too small, a certain amount of mode power leaks into the substrate and, if it is too large, there will be higher modes propagating in the waveguide. Those higher modes are more susceptible to disturbances in the waveguides such as edge roughness than the fundamental mode. For waveguides of width 11 μm, the propagation loss of 0.33 ±0.01 dB/cm is obtained from the measurements of waveguides of three lengths: 14 mm, 18 mm and 21 mm. For waveguides of width 7 μm and 15 μm, the propagation losses are estimated to be 0.35 dB/cm and 0.71 dB/cm respectively. The propagation loss here is dominated by the scattering loss while the free carrier absorption of As_2S_3 is generally negligible [10]. Theoretically the minimum scattering loss in mid IR is even lower than that in near IR, since Rayleigh scattering intensity is proportional to $1/\lambda^4$. Therefore, further reduction in propagation loss can be expected, by improving the sidewall roughness for example. The coupling loss is then estimated to be 1.7 dB per facet based

on the total insertion loss (3.81 dB) and the propagation loss (0.33 dB/cm). Theoretical calculation shows the Fresnel reflection for the As_2S_3-air interface is 0.8 dB. Therefore, the mode mismatch between the waveguide and the QCL accounts for the remaining 0.9 dB, corresponding to a coupling efficiency of 81.3%.

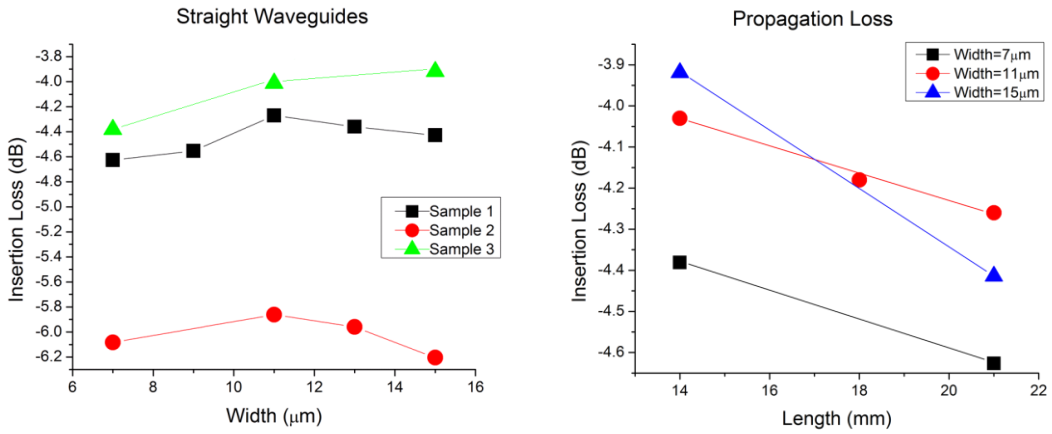

Fig. 61. Measurement results of straight waveguides.

For bent waveguides, the insertion loss tends to increase as the bending radius decreases. If the radius is large (larger than 2 mm), the results of the bends are close to those of straight waveguides, and the lowest loss is measured to be 5.6 dB at a bend radius of 7500 μm. According to FIMMWAVE simulations, as light travels through the waveguide, the sharper the waveguide bends, the farther the mode departs from the center of the waveguide and the more the optical power leaks away. Practically, since the fabrication of the waveguides is not perfect, that is, the edges have acertain degree of roughness inevitably and perhaps some exterior contamination, the deviated mode can

be disturbed and lose energy during propagation. In our experiments, we measured an insertion loss of 6.65 dB for a waveguide of bending radius 250 μm. Subtracting 1.7 dB coupling loss at each end and propagation loss along the 1 cm straight part of the waveguide, the mode loss associated with the 90- degree bend is 2.92 dB. That indicates the possibility of fabricating long waveguides by using serpentine patterns, which can be employed for future research on nonlinearities. The measurement results of a series of bend waveguides on a single sample is shown in Fig. 62.

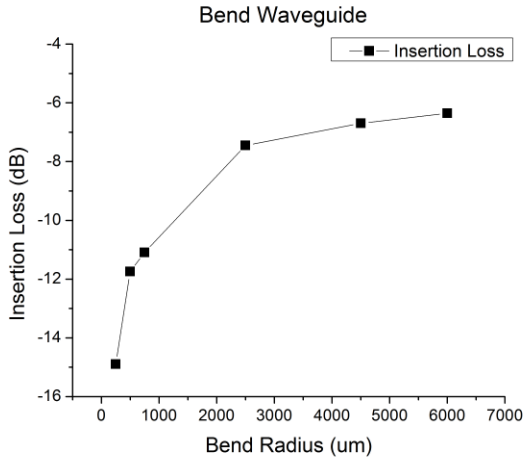

Fig. 62. Measurement results of bent waveguides.

5.2. Integrated polarization converter

The TAMU setup has the capability of characterizing waveguide devices at both 1.55 μm (near IR) and 2.05 μm (at the short end of mid IR spectrum). Owing to the mature fiber-optic telecommunication technology in near IR, a lot of off-the-shelf optical components are readily available, which provide us with a means to demonstrate the

feasibility of our design ideas and understand the working mechanisms in near IR first, and then extend the application into the mid IR.

For near IR wavelengths around 1.55 μm, a tunable laser and an optical vector analyzer (OVA, from LUNA Technologies) are used to obtain the spectral analysis of the device under test (DUT), as Fig. 63 shows [43] .

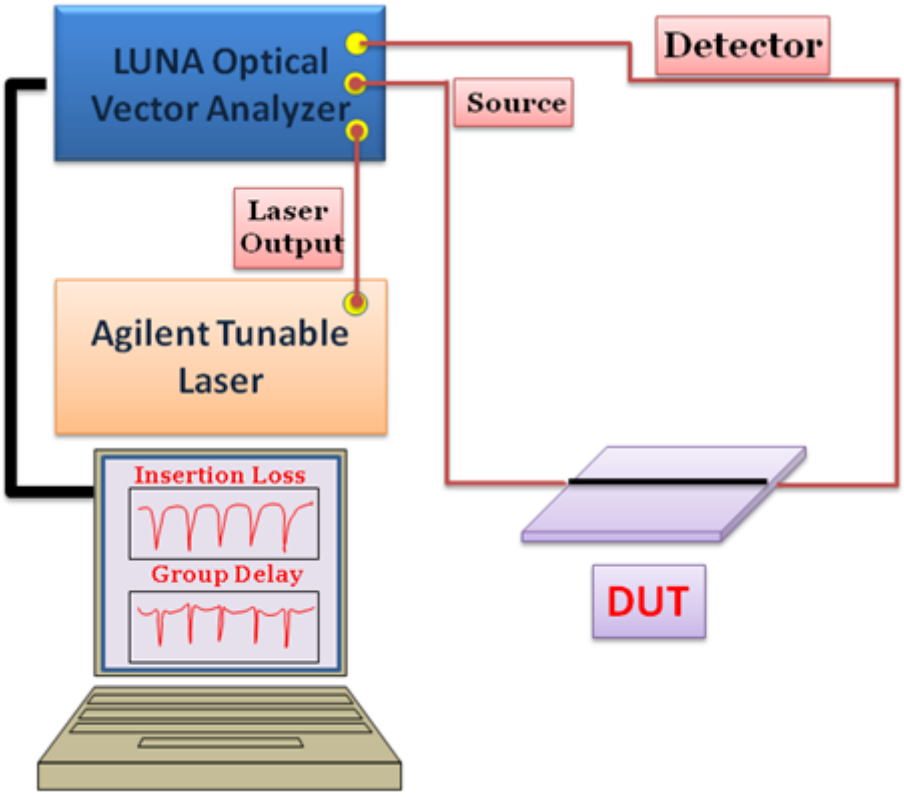

Fig. 63. Measurement setup with OVA in near IR.

Integrated polarization converters are first designed and fabricated for the wavelength of 1.53 μm. According to equation (3.1), the period is designed to be 21 μm

and there are 500 periods totally. Since the OVA measures the maximum and minimum loss only, the measurement data including the Jones matrix and the state of input polarization needs to be processed. After that, the conversion spectrum can be obtained. Both measurement results and calculated conversion spectrum are shown in Fig. 64.

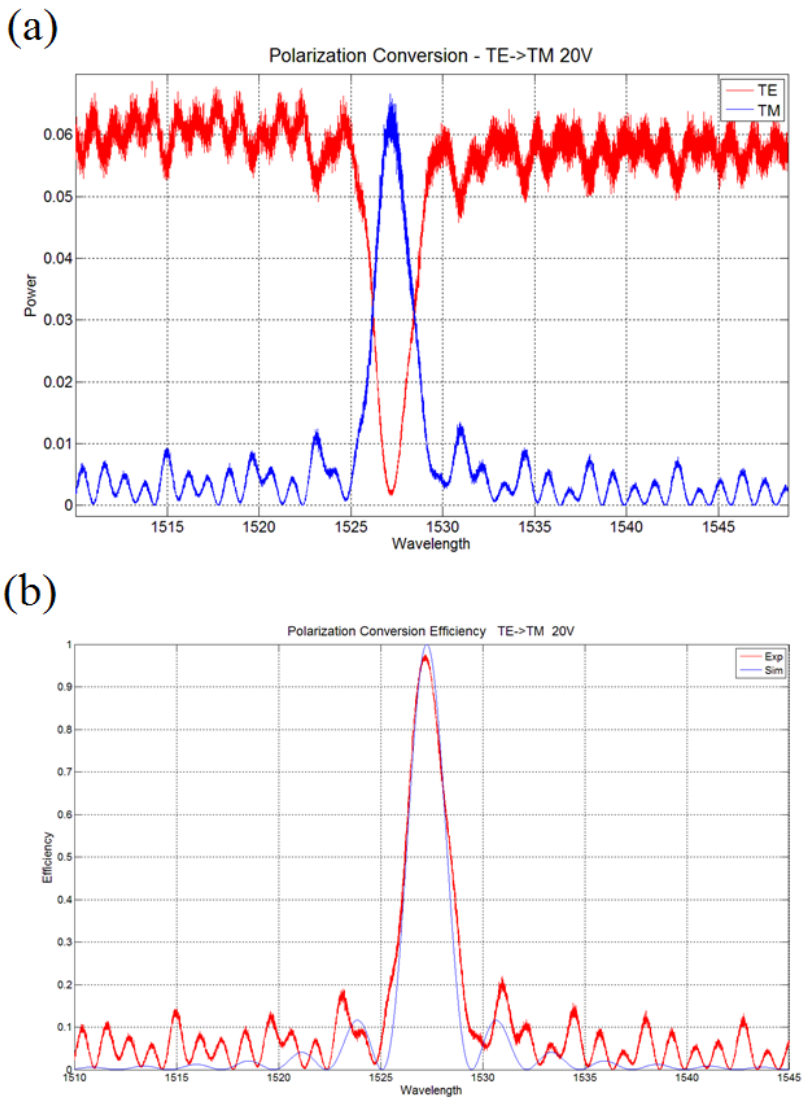

Fig. 64. Measurement result of polarization converter at λ=1.53 μm (a) and calculated conversion spectrum (b).

Then the polarization converters for mid IR are designed and fabricated. Correspondingly the characterization setup needs to be set up. A single-mode (TE_{00}) thulium fiber laser that emits light at the wavelength of 2.05 μm is used as the light source, and an IR power meter with large responsive range and a high sensitivity FTIR are used for detection. The fiber polarizer is used to control the polarization of light and an NI Data Acquisition (Daq) card and Labview program is used to process the detected signals. The measurement setup is shown in Fig. 65.

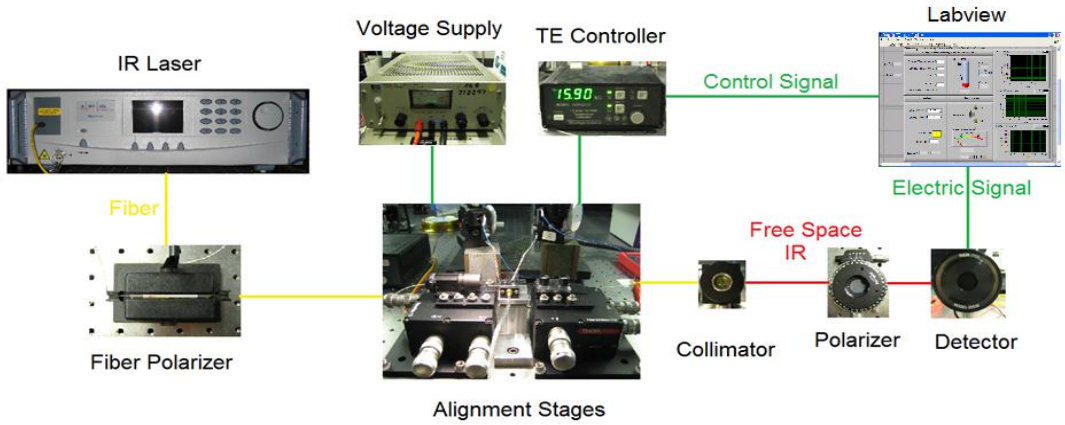

Fig. 65. Mid IR measurement setup in TAMU.

The thulium laser has a tunable output power as high as 1 Watt, with a line width of 1.5 nm centered at the wavelength of 2.05 μm. Although for the narrow bandwidth (limited to 2-3 nm) y-propagation polarization converter, the period of inter-digitated electrodes is designed to be 29.5 μm for working at the wavelength of 2.05 μm, the

fabricated electrodes may have a period or index slightly larger or smaller than that due to fabrication error. As a result, the center conversion wavelength varies from the design. However, it is temperature dependent. Therefore, a thermoelectric temperature control system is employed in the measurement setup to shift the conversion spectrum of the y-propagation polarization converter to overlap with the emission spectrum of the laser.

The thermoelectric system consists of a thermoelectric controller (LCP-3215, from Wavelength Electronics, Inc.), a thermoelectric cooling (TEC) module (TE-127-1.0-2.5, from TE Technology, Inc.) and a thermo-resistor (MP-2444 with TS-141, from TE Technology, Inc.) The thermoelectric cooling (TEC) module functions as a heating or cooling device based on the principle of the Peltier effect, i. e. an electrical current can produce heating or cooling at the junction of two materials, depending on the direction of the current flow. The resistance of the thermo-resistor is dependent on the ambient temperature, which can vary from -4 ℃ to 70 ℃. The TE controller reads the resistance, converts it into the temperature, then compares it to the set temperature and determines if the heating or cooling is needed. As a result, a calculated current flow is provided to the TEC module by the controller, which has a maximum current of 1.5 A and power of 10 Watts.

A sample holding stage made of a set of aluminum chunks designed (please refer to appendix A for details) are machined and assembled for installing the TEC module, which is bonded by thermo epoxy (TE-920H-2.5G, from Custom Thermoelectric, Inc.) to maximize thermal conduction. The thermo epoxy can stand the temperature from -25 ℃ to +110 ℃ and has a high thermal conductivity of 6.05 Watts/mK. The designed

schematic is attached in the appendix. The thermo-resistor reaches to the center of the top aluminum plate along a small drilled hole and affixed by the epoxy. On the top plate, a vacuum waveguide mount (HWV001, from Thorlabs, Inc.) is used to fix the sample while electric probes are contacted during the measurement, as shown in Fig. 66.

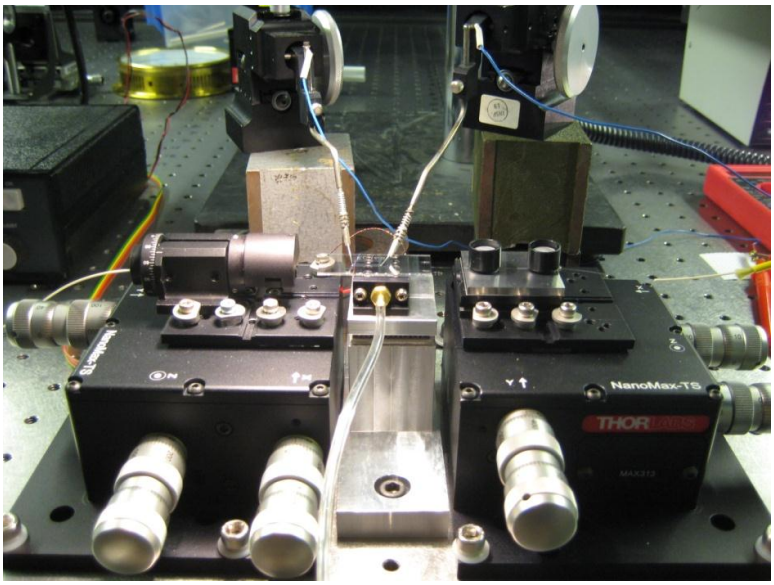

Fig. 66. Sample holding stage with thermoelectric control.

After a series of experiments, the recipe for fabricating titanium diffused waveguide for the wavelength of 2.05 μm is found: the thickness for DC sputtering is 135 nm, the optimum width in photolithography is 11 μm and the diffusion time is 13 hours and 30 minutes. And the insertion loss of the waveguides of both polarization converters can be as low as 2 dB.

For the y- propagation polarization converter, the bandwidth is calculated to be as small as 3 nm. By thermally tuning it, we find that at 28.2 ℃ (correspondingly 13.2

KΩ for thermo-resistor), its conversion spectrum overlaps exactly with the laser spectrum. The measurement result is shown in Fig. 67 along with that of z-propagation polarization.

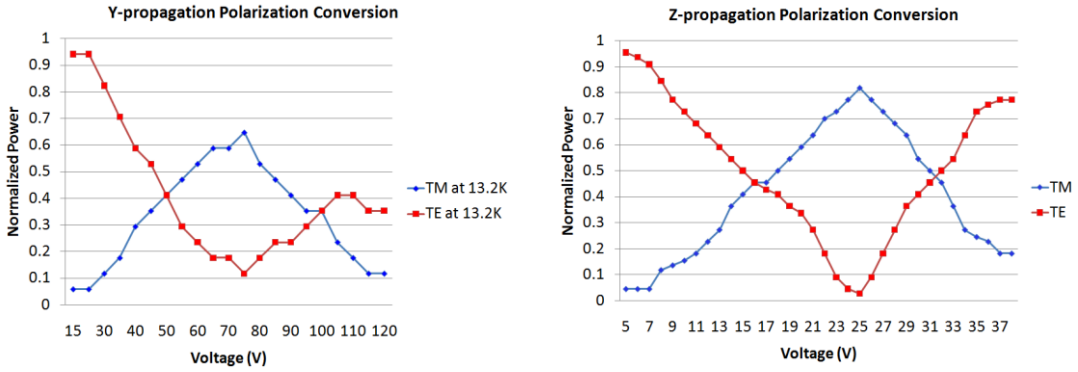

Fig. 67. Measurement results of integrated polarization converters.

The curves show the trend of mode conversion for the y-propagation polarization converter: the power of TM mode goes up while that of TE drops down as the applied voltage increases. While almost 0 at the beginning, the TM curve peaks at 75 V and then falls gradually. The maximum conversion efficiency is estimated to be 78.7%. It is noticeable that the insertion loss for both modes becomes larger as the electric voltage gets bigger. That phenomenon also happens to some of our other EO devices such as Mach-Zehner Interferometer modulators and near IR polarization converters. The reason for such deterioration is still under study; it may be due to the fluctuations of refractive index in the Ti: $LiNbO_3$ waveguides, which can be caused by fabrication errors, the strain induced by SiO_2 buffer or non-uniformity of the electrodes.

The measurement result is simulated and fitted in Matlab in order to understand the device better (Fig. 68). The fact that the maximum conversion efficiency cannot reach 100% results from the fact that the phase mismatch δ is not completely zero.

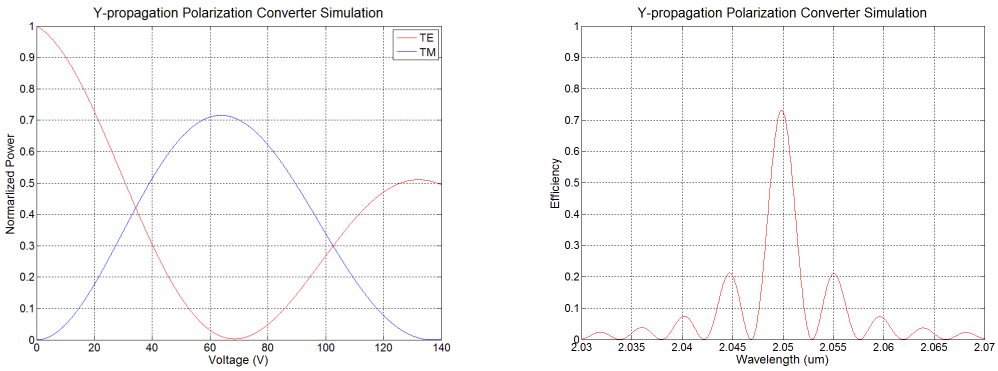

Fig. 68. Simulation results of integrated polarization converters.

For z-propagation polarization converter, since the phases of TM and TE are naturally matched, no extra measuring steps are needed and it was easier to get a neat mode conversion curve. However, because the index profile of the diffused waveguide is not symmetric, in practice the mode effective indices of TE and TM are not exactly the same, resulting in less than 100% maximum conversion efficiency. Shown on the curve in Fig. 67, TM reaches its maximum at 25 V, where the conversion efficiency is calculated to be 92.3%. The bandwidth, which is simulated in FIMMWAVE and Matlab subsequently, covers the range from 700 nm to 2.9 μm, where the upper limit is due to the mode cutoff condition of the waveguide. In addition, compared to y-propagation

polarization converter, the conversion voltage can be largely reduced by adding a center electrode, meaning a higher efficiency.

5.3. As_2S_3-Ti: $LiNbO_3$ taper coupler

Measurement results confirm the function of taper couplers (Table IV). Generally, the cross port accounts for 50% to 90% of the total output power. Neglecting the excess loss caused by propagation in the low-loss As_2S_3 and Ti waveguides, the average coupling efficiency is 73.2%. However, prior to extracting the precise coupling efficiency, the propagation loss and bending loss in As_2S_3 waveguide have to be calibrated first. Many experiments need to be done for that, and the work is still ongoing.

Table IV. Measurement data of sbends.

Pattern	Sample	Cross (dB)	Through (dB)	Cross in Total (%)
sbend 2	RC463	-12.5	-31	98.6
sbend 4	RC463	-13	-26	95.2
sbend 2	RC531	-8.8	-7.8	44.3
sbend 4	RC531	-12.3	-16.4	72
sbend 3	RC531	-15.9	-16.9	55.7

In order to understand the experimental results, actually fabricated taper couplers are analyzed using the modeling method. As mentioned previously, due to prolonged

hardbake time, the average fabricated tip width of tapered As_2S_3 waveguide is 1.3 μm, and it may be larger or smaller than that depending on fabrication conditions. A study on the influence of the tip width variation for two stage tapers was conducted, and the result is shown in Fig. 69.

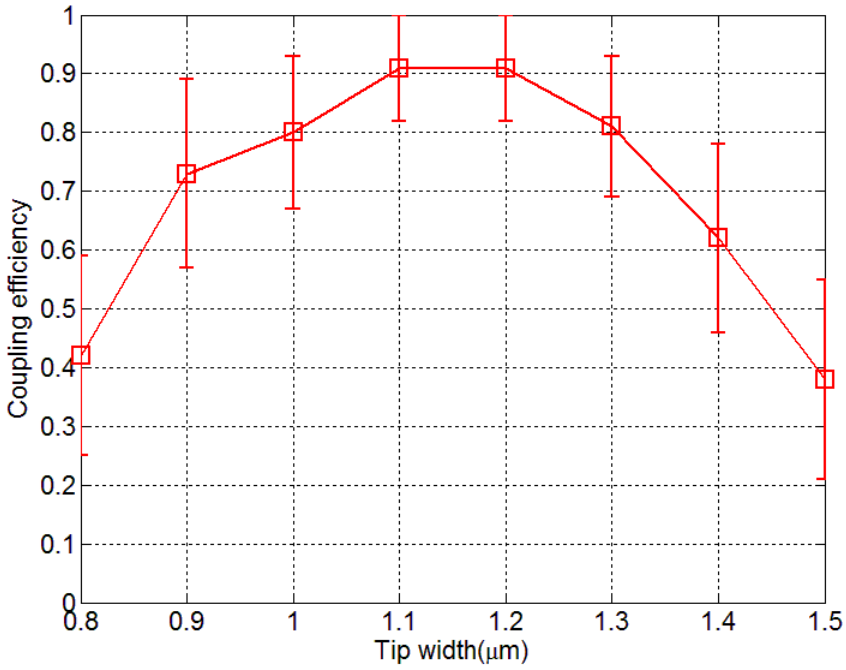

Fig. 69. Study on variation of tip width for two-stage taper design.

From the graph we can see the coupling efficiency is very sensitive to the tip width. When the tip width is 1.3 μm, the coupling efficiency is 81%±12% according to the simulation. The measurement result, average coupling efficiency 73.2% falls right into that range. When the tip is small, e. g. 0.8 μm, the actual transition width of fabricated taper coupler is 1.4 μm, which is smaller than the critical width at the

wavelength of 1531 nm (1.47 μm). Therefore, the mode is under coupled and there is a drop in coupling efficiency in the region.

Instead of working at a single wavelength, these practical taper couplers are designed to work for a wavelength range. Accordingly, their coupling behaviors in frequency domain are studied. The measured spectrum at the cross port is presumably to have the same trends of the coupling spectrum, with an offset from the exact values. That offers the information of taper couplers in the frequency domain and can be used as another means to test our simulation method. The typical measured spectrum, along with simulation results is shown in Fig. 70. In simulation the wavelength is scanned correspondingly from 1520 nm to 1600 nm, at an interval of 2 nm. The results show that, though the taper coupler exhibits a certain degree of wavelength dependency, it has high coupling efficiency over a broad bandwidth.

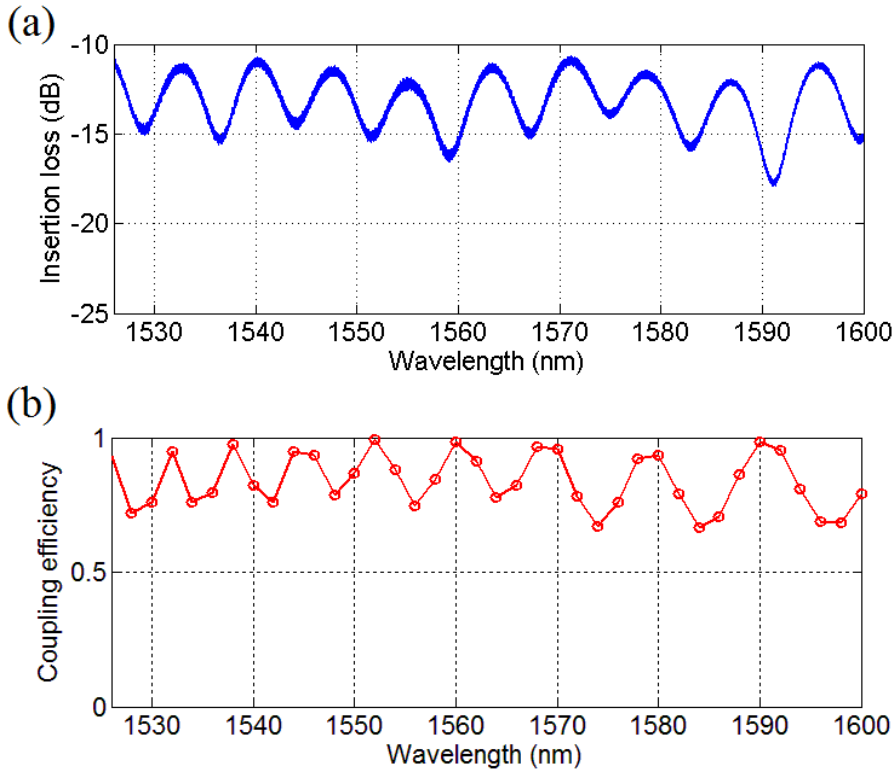

Fig. 70. Measured (a) and simulated (b) coupling spectra of taper coupler with tip width = 1.3 μm.

From the curve, we can see that the period of oscillation is less than 10 nm, and longer wavelengths have a larger oscillation period than shorter wavelengths: both are captured by the simulation. The oscillation of the coupling curve is a strong indication of mode beating while the phenomenon that longer wavelengths have a slightly larger oscillation period possibly comes from waveguide dispersion: the wavelength-dependent propagation constant. Simulation shows that when the wavelength varies from 1530 nm to 1540 nm, the confinement of the mode in As_2S_3 waveguide changes from 0.4536 to 0.4459 and the effective index changes from 2.2345 to 2.2331. Consequently, the

propagation constant changes from 9.1763 to 9.1110, decreasing by 0.7%, as shown in Table V.

Table V. Dispersion in As_2S_3-Ti hybrid waveguide.

Wavelength (nm)	**Confinement factor**	**neff**	**β (μm^{-1})**
1530	0.4536	2.2345	9.1763
1540	0.4459	2.2331	9.111
↑ 0.6%	↓ 1.8%	↓ 0.06%	↓ 0.7%

From the plot of γ in Fig. 71, we can learn that different wavelengths have different critical widths, which shifts to a larger value as the wavelength increases. Such change makes the mode at different wavelengths see the taper coupler slightly different, and the energy transfer does not take place at the same location: the mode of a shorter wavelength couples before that of a longer wavelength. Moreover, we can see that as wavelength increases, the rate of shift increases, confirming the presence of dispersion.

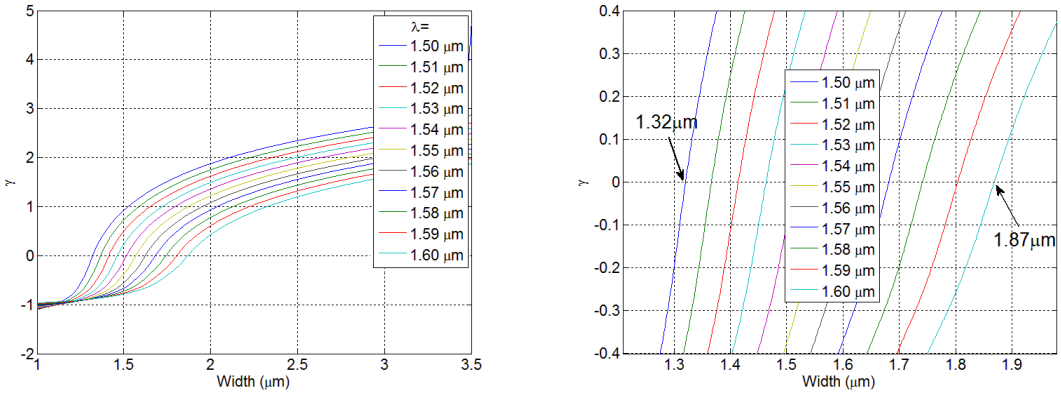

Fig. 71. Spectrum of normalized phase mismatch γ, with magnified critical width.

Because of a 0.3 μm expansion during fabrication, the average tip width of tapered As_2S_3 waveguide is 1.3 μm, and accordingly the transition width is 1.9 μm. Whether it is smaller or larger than that is dependent on the process conditions, which is hard to control and manifested in the measured coupling spectra, as shown in Fig. 72 (a) and Fig. 73 (a). Models are built to analyze them, in Fig. 72 (b) and Fig. 73 (b). In Fig. 72, there is a drop in coupling efficiency in the long wavelength region, while the model shows if the tip width is reduced to 1.2 μm, correspondingly the end width of the first stage is 1.8 μm, such a coupling spectrum will result. The phenomenon can be understood from the plot of γ in Fig. 71: at the wavelength of 1600 nm, the critical width is read to be 1.87 μm, which is larger than the actual transition width (1.8 μm). Hence the transfer of the energy has not completed yet at the end of the first stage, resumes at the second stage where the width varies very fast, and considerable energy is coupled to odd mode. Consequently, the coupling efficiency drops.

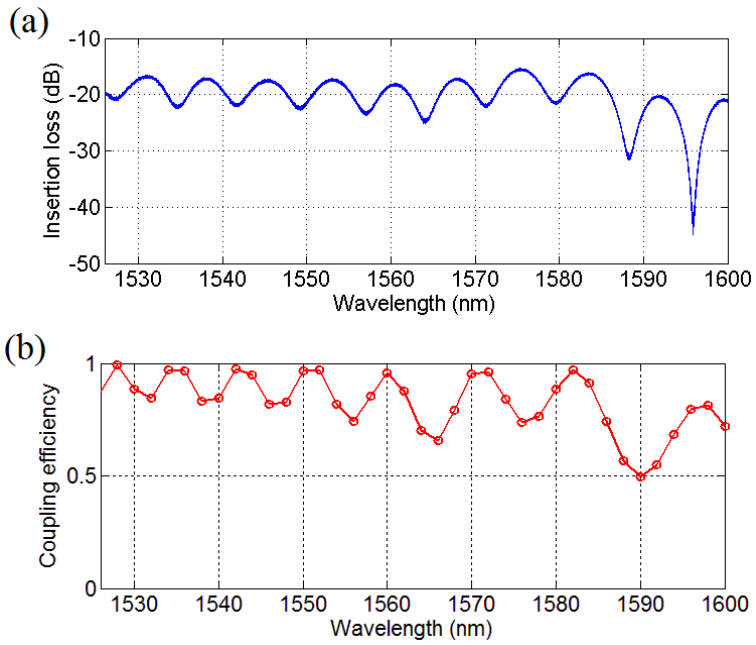

Fig. 72. Measured (a) and simulated (b) coupling spectra of taper coupler with tip width = 1.2 μm.

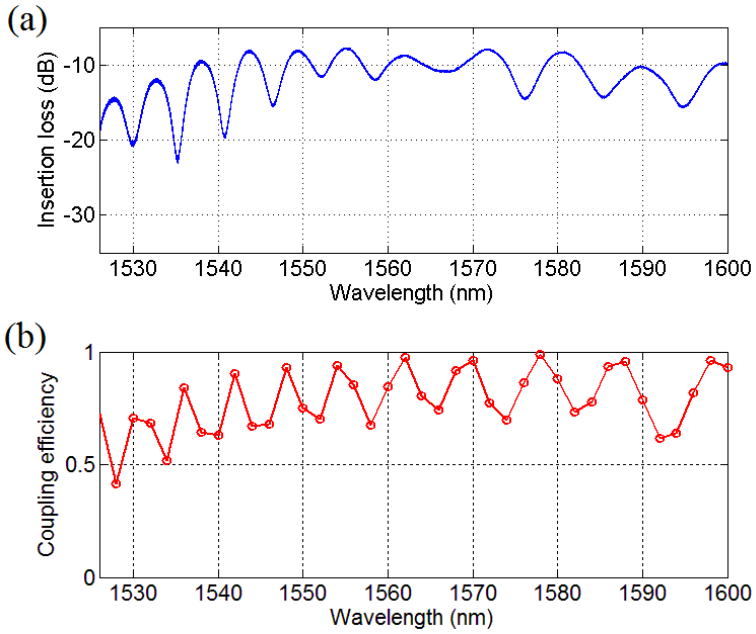

Fig. 73. Measured (a) and simulated (b) coupling spectra of taper coupler with tip width = 1.4 μm.

Similarly, the model explains the drop of coupling efficiency in the short wavelength region for Fig. 73. Provided that the tip width is larger, e. g. 1.4 μm, for short wavelengths such as 1525 nm, the critical width is 1.32 μm, which is smaller than the initial tip width. As a result, the odd mode is excited at the input of the taper coupler, and the coupling efficiency in this wavelength region is degraded, as shown in the curve.

From the above analysis, we see a tradeoff between the applicable wavelength range and the design parameters, which provides a way of controlling the frequency domain behavior of the taper couplers: By adjusting the transition width between two stages we can cut off longer wavelengths and by changing the tip width we can suppress the coupling of shorter wavelengths.

CHAPTER VI

CONCLUSION

Arsenic trisulfide (As_2S_3) waveguide devices on the substrate of lithium niobate ($LiNbO_3$) for integrated trace gas detection system were studied, from design to fabrication and to characterization. They were low-loss As_2S_3 waveguides, polarization converters using titanium diffused waveguides (Ti: $LiNbO_3$) and As_2S_3-Ti: $LiNbO_3$ mode couplers.

Straight and bent chalcogenide (As_2S_3) waveguides on $LiNbO_3$ substrates were studied to provide an optical interconnection for wavelengths up to mid infrared (IR). Designed for single mode propagation, they were fabricated through photolithography and dry-etching technology, and characterized on a mid IR measurement setup with a quantum cascade laser for the wavelength of 4.8 μm. Owing to the process development on etching, good sidewalls were obtained, resulting in a propagation loss as low as 0.33 dB/cm; the improved polishing method on end facets promoted the coupling efficiency to 81%; and the measurement results showed a less than 3 dB loss for a 250 μm bend radius. These results were substantially lower than the previous published ones (Table VI).

Table VI. Comparison of loss of chalcogenide waveguides.

Researchers	Insertion Loss	Propagation Loss
Nicolas Ho et al.	~20 dB	1.1 dB/cm
Candice Tsay et al.	~15 dB	4.5 dB/cm
Xin Xia et al.	~4 dB	0.33 dB/cm

Essential to some applications such as Faraday Rotation Spectroscopy, the function of polarization control, i. e. TE-TM conversion, was demonstrated using titanium diffused waveguides on a lithium niobate substrate based on the electro-optic effect. Two types of polarization converters were experimentally fabricated: one was made using x-cut, y-propagation with periodic electrodes along the propagation direction, while the other one was configured with x-cut, z-propagation and two outer electrodes plus a center one. They were characterized on a homemade, thermally controlled measurement setup at a wavelength of 2.05 μm. The z-propagation scheme, which has a larger bandwidth and simpler electrode design than the y-propagation one, exhibited a higher efficiency (92.3%) and a lower conversion voltage (25V). Because of its small bandwidth (3 nm) and tunability with temperature, the y-propagation polarization converter can play an important role in realizing narrow band filter functions.

Now that the integrated polarization converters using titanium diffused waveguides in $LiNbO_3$ are successfully demonstrated, it should be easy to make other functional devices. However, due to the small index contrast ($\Delta n<0.03\%$) and large

diffusion area, it is difficult for titanium diffused waveguides to realize compact patterns. That weakness can be compensated by As_2S_3 waveguides, which have a much higher index contrast (Δn=~20%). Hence in order to integrate As_2S_3 waveguide and the titanium waveguide polarization converter, an As_2S_3-Ti: $LiNbO_3$ taper coupler was studied. Although the preliminary experiments have shown the feasibility of such integration, the underlying mechanism was not well understood and guidelines for design were lacking. Therefore, a simulation method based on supermode theory and transfer matrix formalism was developed, and then applied to the taper coupler design, which are generally not adiabatic but highly efficient in terms of practical use. Simulations show that for those practical tapers, both adiabatic coupling and resonant coupling play an important role. There exists an optimum taper design with respect to the tip width, end width and length. A two-stage taper design can largely reduce the total length of the taper, e. g. by 64%, while keeping high coupling efficiency above 90%.

Following the guidelines, taper couplers were designed, fabricated and characterized. The measurement results agreed with the simulation results well, suggesting a good coupling efficiency. In addition, the experimental results confirm the validity of the modeling method, which in turn, was used to analyze the fabricated taper couplers. Frequency domain analysis shows that the taper couplers work for a range of wavelengths, which can be controlled by adjusting the transition width and the tip width.

These basic devices combined together provide a set of compact and versatile means for guiding and manipulating optical modes in integrated optical circuits for both near and mid infrared wavelengths, serving as cornerstones for integrated trace gas

detection systems and other infrared integrated optical circuits. Based on them, more complicated structures and functional devices can be developed in the future.

The As_2S_3 waveguide opens up the prospect of realizing a lot of waveguide devices (Fig. 74), such as directional couplers, multi-mode interference (MMI) couplers, Mach Zehnder Interferometers and ring filters. With phase engineering techniques, As_2S_3 waveguides with a certain dimension can be applied for nonlinearity study, such as optical tuning through self-phase or cross-phase modulation, and new frequency generation by four-wave-mixing. Together with phase modulation, arbitrary on-chip polarization control can be achieved based on the electro-optical effect of lithium niobate. In addition, the integration of As_2S_3 waveguides and Ti: $LiNbO_3$ waveguides makes those devices efficiently connected with single mode fibers and thus ready for commercialization.

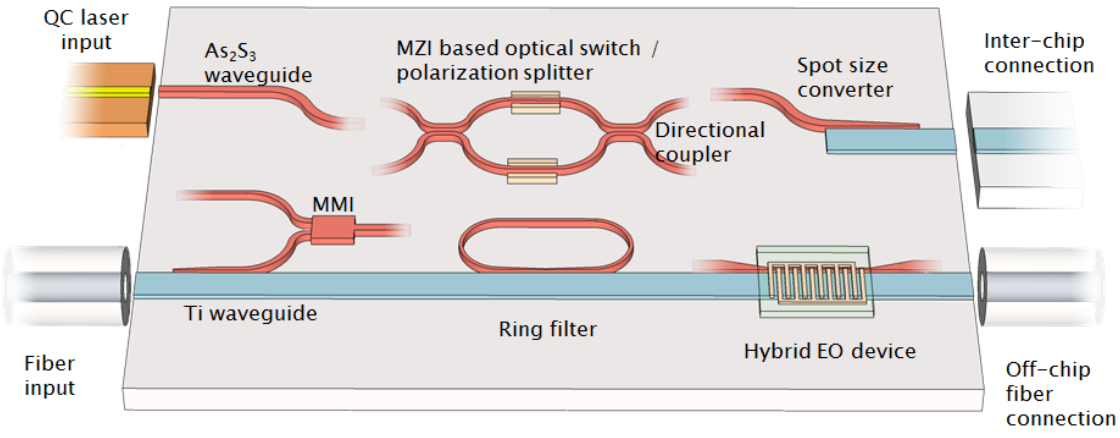

Fig. 74. Waveguide devices for integrated optical circuits.

REFERENCES

[1] B. Stuart, Ed., *Infrared Spectroscopy: Fundamentals and Applications, Analytical Techniques in the Sciences*. Dartford, Kent, UK: John Wiley & Sons, Ltd, 2004, p. 224.

[2] A. Yariv and P. Yeh, *Photonics, Optical Electronics in Modern Communications*, Sixth ed. New York: Oxford University Press, 2007.

[3] Mirthe. Available: www.mirthecenter.org, accessed in Jan, 2011.

[4] H. Nishihara, M. Haruna, and T. Suhara, Eds., *Optical Integrated Circuits, McGraw-Hill Optical and Electro-optical Engineering Series*. New York: McGraw-Hill Book Company, 1987, p. 374.

[5] J. Faist, F. Capasso, C. Sirtori, D. L. Sivco, J. N. Baillargeon, *et al.*, "High power mid-infrared (λ~ 5 μm) quantum cascade lasers operating above room temperature," *Appl. Phys. Lett.,* vol. 68, pp. 3680-3682, 1996.

[6] A. Zakery and S. R. Elliott, "Optical properties and applications of chalcogenide glasses: A review," *J. Non-Cryst. Solids.,* vol. 330, pp. 1-12, 2003.

[7] C. M. Jean-Francois Viens, A. Villeneuve, T. V. Galstian, E. J. Knystautas, M. A. Duguay, K. A. Richardson, and T. Cardinal, "Fabrication and characterization of integrated optical waveguides in sulfide chalcogenide glasses," *J. Lightw. Technol.,* vol. 17, p. 8, 1999.

[8] J. S. Sanghera, L. B. Shaw, and I. D. Aggarwal, "Applications of chalcogenide glass optical fibers," *C. R. Chim.,* vol. 5, pp. 873-883, 2002.

[9] W. S. Rodney, I. H. Malitson, and T. A. King, "Refractive index of arsenic trisulfide," *J. Opt. Soc. Am.,* vol. 48, pp. 633-635, 1958.

[10] V. Ta'eed, N. J. Baker, L. Fu, K. Finsterbusch, M. R. E. Lamont, *et al.*, "Ultrafast all-optical chalcogenide glass photonic circuits," *Opt. Exp.,* vol. 15, pp. 9205-9221, 2007.

[11] R. S. Weis and T. K. Gaylord, "Lithium niobate: Summary of physical properties and crystal structure," *Appl. Phys. A: Mat. Sci. & Process.,* vol. 37, pp. 191-203, 1985.

[12] A. W. Fang, H. Park, R. Jones, O. Cohen, M. J. Paniccia, *et al.*, "A continuous-wave hybrid AlGaInAs-silicon evanescent laser," *IEEE Photon. Technol. Lett.,* vol. 18, pp. 1143-1145, 2006.

[13] H. Park, A. W. Fang, O. Cohen, R. Jones, M. J. Paniccia, *et al.*, "A hybrid AlGaInAs-Silicon evanescent amplifier," *IEEE Photon. Technol. Lett.,* vol. 19, pp. 230-232, 2007.

[14] H Park, AW Fang, R Jones, O Cohen, O Raday, *et al.*, "A hybrid AlGaInAs-silicon evanescent waveguide photodetector," *Opt. Exp.,* vol. 15, pp. 6044-6052, 2007.

[15] A. Yariv and X. Sun, "Supermode Si/III-V hybrid lasers, optical amplifiers and modulators: A proposal and analysis," *Opt. Exp.,* vol. 15, pp. 9147-9151, 2007.

[16] M. E. Solmaz, D. B. Adams, S. Grover, W. Tan, X. Xia, *et al.*, "Compact bends for achieving higher integration densities for $LiNbO_3$ waveguides," *IEEE Photon. Technol. Lett.,* vol. 21, pp. 557-559, 2009.

[17] M. E. Solmaz, D. B. Adams, S. Grover, W. Tan, X. Xia, *et al.*, "First demonstration of an As_2S_3-on-$LiNbO_3$ ring resonator," in *Optical Fiber Comms. Conference*, San Diego, California, USA, 2009, paper OWV7.

[18] L. Tao and R. W. Ziolkowski, "Grating assisted waveguide-to-waveguide couplers," *IEEE Photon. Technol. Lett.,* vol. 10, pp. 693-695, 1998.

[19] B. Wang, J. Jiang, and G. Nordin, "Compact slanted grating couplers," *Opt. Exp.,* vol. 12, pp. 3313-3326, 2004.

[20] D. Taillaert, W. Bogaerts, P. Bienstman, T. F. Krauss, P. Van Daele, *et al.*, "An out-of-plane grating coupler for efficient butt-coupling between compact planar waveguides and single-mode fibers," *IEEE J. Quantum Electron.,* vol. 38, pp. 949-955, 2002.

[21] J. Haes, J. Willems, and R. G. Baets, "Design of adiabatic tapers for high-contrast step index waveguides," in *Linear Nonlinear Integrated Opt.,* Lindau, Federal Republic of Germany, 1994, pp. 685-693.

[22] Y. Ruan, W. Li, R. Jarvis, N. Madsen, A. Rode, *et al.*, "Fabrication and characterization of low loss rib chalcogenide waveguides made by dry etching," *Opt. Exp.,* vol. 12, pp. 5140-5145, 2004.

[23] W. C. Tan, M. E. Solmaz, J. Gardner, R. Atkins, and C. Madsen, "Optical characterization of As_2S_3 thin films prepared by magnetron sputtering," *J. Appl. Phys.,* vol. 107 p. 033524, 2010.

[24] J. Hu, V. Tarasov, N. Carlie, N. Feng, L. Petit, *et al.*, "Si-CMOS-compatible lift-off fabrication of low-loss planar chalcogenide waveguides," *Opt. Exp.,* vol. 15, pp. 11798-11807, 2007.

[25] Z. G. Lian, W. Pan, D. Furniss, T. M. Benson, A. B. Seddon, *et al.*, "Embossing of chalcogenide glasses: Monomode rib optical waveguides in evaporated thin films," *Opt. Lett.,* vol. 34, pp. 1234-1236, 2009.

[26] N. J. Baker, H. W. Lee, I. Littler, C. M. de Sterke, B. J. Eggleton, *et al.*, "Sampled Bragg gratings in chalcogenide (As_2S_3) rib-waveguides," *Opt. Exp.,* vol. 14, pp. 9451-9459, 2006.

[27] S. J. Madden, D. Y. Choi, D. A. Bulla, A. V. Rode, B. Luther-Davies, *et al.*, "Long, low loss etched As_2S_3 chalcogenide waveguides for all-optical signal regeneration," *Opt. Exp.,* vol. 15, pp. 14414-14421, 2007.

[28] V. G. Ta'eed, L. Fu, M. Pelusi, M. Rochette, I. C. Littler, *et al.*, "Error free all optical wavelength conversion in highly nonlinear As-Se chalcogenide glass fiber," *Opt. Exp.,* vol. 14, pp. 10371-10376, 2006.

[29] L. R. Deng, "Design of mid-infrared ridge-waveguide directional couplers by OptiWave simulation," in *Opt*, M. Osinski, Ed. NNIN REU 2006 Research Accomplishments, 2006, p. 2.

[30] N. Ho, M. C. Phillips, H. Qiao, P. J. Allen, K. Krishnaswami, *et al.*, "Single-mode low-loss chalcogenide glass waveguides for the mid-infrared," *Opt. Lett.,* vol. 31, pp. 1860-1862, 2006.

[31] C. Tsay, E. Mujagic, C. F. Gmachl, and C. B. Arnold, "Solution-cast As_2S_3 raised strip waveguides for integrated mid-ir optics," *Conference on CLEO/QELS*, Baltimore, MD, USA, 2009, paper CTuO2.

[32] O. Eknoyan, C. H. Bulmer, R. P. Moeller, W. K. Burns, and K. H. Levin, "Guided-wave electro-optic modulator in Ti: $LiNbO_3$ at 2.6 μm," *J. Appl. Phys.,* vol. 59, pp. 2993-2995, 1986.

[33] C. T. Lee, M. L. Wu, L. G. Sheu, P. L. Fan, J. M. Hsu, *et al.*, "Design and analysis of completely adiabatic tapered waveguides by conformal mapping," *J. Lightw. Technol.,* vol. 15, pp. 403-410, 1997.

[34] F. Xia, V. M. Menon, and S. R. Forrest, "Photonic integration using asymmetric twin-waveguide (ATG) technology: Part I-concepts and theory," *Selected Topics in IEEE J. Quantum Electron.,* vol. 11, pp. 17-29, 2005.

[35] X. Sun, H. Liu, and A. Yariv, "Adiabaticity criterion and the shortest adiabatic mode transformer in a coupled-waveguide system," *Opt. Lett.,* vol. 34, pp. 280-282, 2009.

[36] J. Haes, R. Baets, C. M. Weinert, M. Gravert, H. P. Nolting, *et al.*, "A comparison between different propagative schemes for the simulation of tapered step index slab waveguides," *J. Lightw. Technol.,* vol. 14, pp. 1557-1569, 1996.

[37] Wikipedia, "Maxwell's equations," in *Wikipedia.* Available: http://en.wikipedia.org/wiki/Maxwell's_equations, accessed in Jan, 2011.

[38] Wikipedia, "Insertion loss," in *Wikipedia.* Available: http://en.wikipedia.org/wiki/Insertion_loss, accessed in Jan, 2011.

[39] N. Yu, L. Diehl, E. Cubukcu, C. Pflügl, D. Bour, *et al.*, "Near-field imaging of quantum cascade laser transverse modes," *Opt. Exp.,* vol. 15, pp. 13227-13235, 2007.

[40] S. Thaniyavarn, "Wavelength-independent, optical-damage-immune $LiNbO_3$ TE-TM mode converter," *Opt. Lett.,* vol. 11, pp. 39-41, 1986.

[41] A. Yariv, *Optical Electronics in Modern Communications*, 5th ed. New York: Oxford University Press, 1997.

[42] J. M. Liu, "Coupling of Waves and Modes," in *Photonic Devices*, Cambridge: University Press, 2005, p. 1052.

[43] M. Solmaz, "Integration of arsenic trisulfide and titanium diffused lithium niobate waveguides," PhD dissertation, Electrical Engineering, Texas A&M University, College Station, 2010.

[44] P. K. Montgomery, K. Lucas, K. J. Strozewski, L. Zavyalova, G. Grozev*, et al.*, "Resist reflow for 193-nm low-K1 lithography contacts," in *Adv. Resist Technol. Process. XX*, Santa Clara, CA, USA, 2003, pp. 807-816.

[45] Y. Kang, S. Woo, S. Choi, and J. Moon, "Development of resists for thermal flow process applicable to mass production," in *Adv. Resist Technol. Process. XVIII*, Santa Clara, CA, USA, 2001, pp. 222-231.

[46] L. Dong, C. Fan, J. Huang, and H. Luo, "Experimental study of precision polishing of hard and brittle Material," *Key Eng. Mat.,* vol. 359 - 360, p. 4, 2008.

[47] R. Rabelo, "Spectral slicing filters in titanium diffused lithium niobate (Ti: $LiNbO_3$)," PhD dissertation, Electrical Engineering, Texas A&M University, College Station, 2008.

APPENDIX A

SCHEMATICS OF SAMPLE HOLDING CHUNKS FOR THERMALLY TUNABLE STAGE

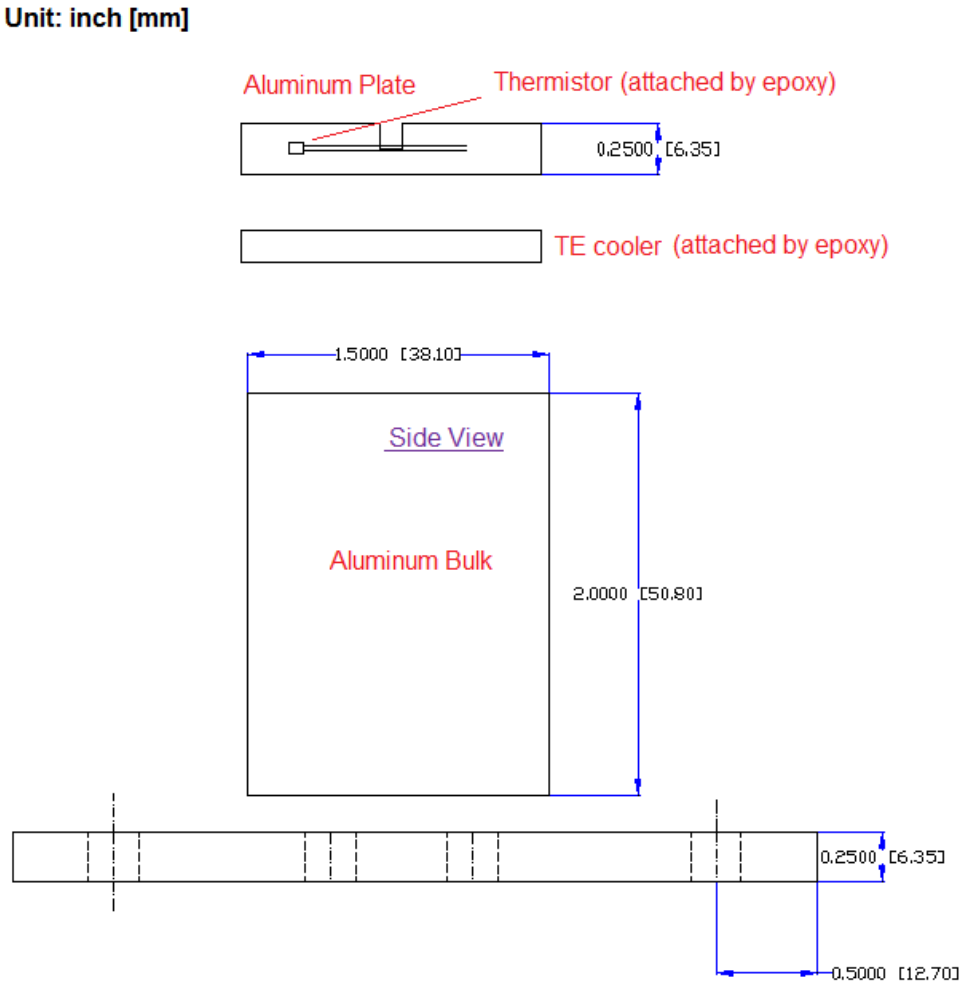

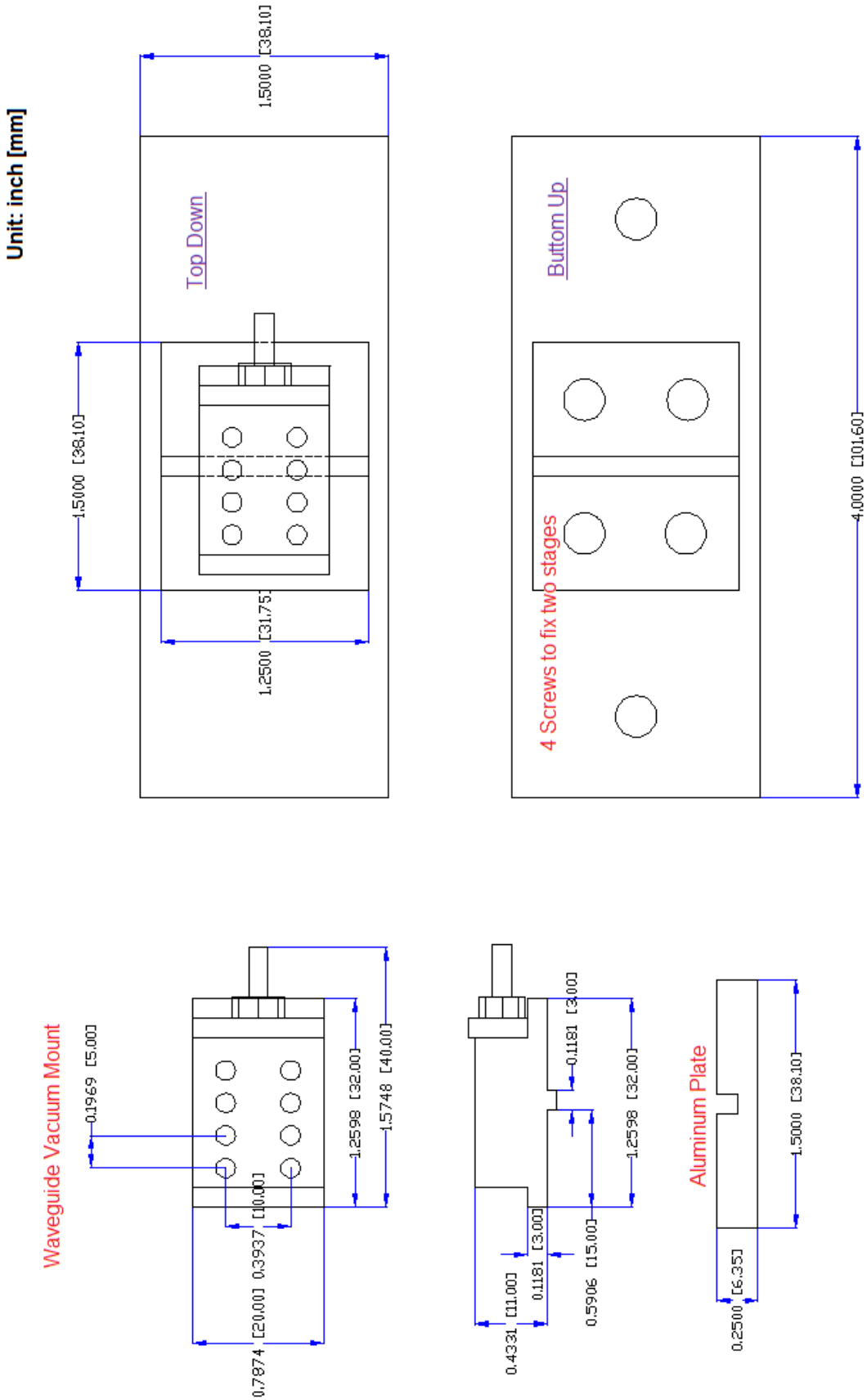
Unit: inch [mm]
Top Down
1.5000 [38.10]
1.5000 [38.10]
1.2500 [31.75]
Buttom Up
4 Screws to fix two stages
4.0000 [101.60]
Waveguide Vacuum Mount
0.1969 [5.00]
0.3937 [10.00]
0.7874 [20.00]
1.2598 [32.00]
1.5748 [40.00]
0.4331 [11.00]
0.1181 [3.00]
0.5906 [15.00]
0.1181 [3.00]
1.2598 [32.00]
Aluminum Plate
0.2500 [6.35]
1.5000 [38.10]

APPENDIX B

MATLAB CODE FOR TAPER COUPLER MODELING

```
% Taper Coupler Modeling Using Supermode Theory and Transfer Matrix Formalism
% For both two-stage tapers and linear tapers
% Author: Xin (Alex) Xia & Yifeng (Ivan) Zhou
% Date: Sept 12, 2010

%%%%%%%%%%%%%%%%%%%%%%%%%%%%%%%%%%%%%%%%%%%%%%%%%%%%%%%%%%%%%%%%%%%%%%%
Model building: data read-in and variable preparation
%%%%%%%%%%%%%%%%%%%%%%%%%%%%%%%%%%%%%%%%%%%%%%%%%%%%%%%%%%%%%%%%%%%%%%%

clear all;
format long;

% Read in data file of the even and odd mode for coupled waveguides generated by
FIMMWAVE
M0=load('adiabatic_taper_scan_1.53um_AsTi_TM_4_0.47um_air_0.6-
4.0um_FMM_80_Aug_11.txt');

Ws=1.0;                                  % start point 0.6<=W<=3.5
We=3.5;                                  % end point
N=4;                                     % number of total modes calculated
L1_tot=2000;
L2_tot=3000;
N1=301;

num=size(M0,2);
iter=length(M0)/N;
M1=zeros(iter,num);
M2=zeros(iter,num);
for i=1:iter,
   M1(i,:)=M0(N*i-3,:);
   M2(i,:)=M0(N*i-2,:);
end
temp_width=M1(:,1);
temp_neff_e=M1(:,4);
temp_beta_e=M1(:,3);
temp_neff_o=M2(:,4);
temp_beta_o=M2(:,3);
```

```
% Read in data file of the As2S3 mode for uncoupled waveguide generated by
FIMMWAVE
M0=load('adiabatic_taper_scan_1.53um_As_TM_4_0.47um_air_0.6-
4.0um_FMM_80_Aug_11.txt');

N=4;                                        %number of modes calculated
num=size(M0,2);
iter=length(M0)/N;
M1=zeros(iter,num);
M2=zeros(iter,num);
for i=1:iter,
   M1(i,:)=M0(N*i-3,:);
end
temp_beta_2=M1(:,3);
temp_neff_2=M1(:,4);
for i=1:size(temp_width,1),
   if Ws==temp_width(i),
      wi=i;
   end
   if We==temp_width(i),
      wj=i;
   end
end
iter=wj-wi+1;
width=ones(iter,1);
neff_e=ones(iter,1);
beta_e=ones(iter,1);
neff_o=ones(iter,1);
beta_o=ones(iter,1);
beta_2=ones(iter,1);
neff_2=ones(iter,1);
for i=1:iter,
   neff_e(i)=temp_neff_e(i+wi-1);
   beta_e(i)=temp_beta_e(i+wi-1);
   neff_o(i)=temp_neff_o(i+wi-1);
   beta_o(i)=temp_beta_o(i+wi-1);
   beta_2(i)=temp_beta_2(i+wi-1);
   neff_2(i)=temp_neff_2(i+wi-1);
   width(i)=temp_width(i+wi-1);
end

% Read in data file of the Ti mode for uncoupled waveguide generated by FIMMWAVE
beta_1=9.077716768*ones(iter,1);
neff_1=2.211932912*ones(iter,1);
```

```
% Interpolation for better resolution
width_int=[Ws:0.002:We];
width_int=width_int';
beta_1=interp1(width, beta_1, width_int, 'spline');
beta_2=interp1(width, beta_2, width_int, 'spline');
beta_e=interp1(width, beta_e, width_int, 'spline');
beta_o=interp1(width, beta_o, width_int, 'spline');
ref=zeros(length(width_int),1);

% Calculate and plot the propagation parameters delta, beta_c0 and k
delta=(beta_2-beta_1)/2;
beta_c0=(beta_e-beta_o)/2;
k=sqrt(beta_c0.^2-delta.^2);
gamma=delta./k;

figure;
set(gca,'Fontsize',16);
plot(width_int, beta_1,'k', width_int, beta_2,'b', width_int, beta_o,'g', width_int,
beta_e,'r','Marker','o','MarkerSize', 2);
grid;
legend('\beta_1','\beta_2','\beta_o','\beta_e');
title('\fontsize{18}Propagation Constants');
xlabel('\fontsize{16}Width of taper (\mum)');
ylabel('\fontsize{16}Propagation constant (1/\mum)');

figure;
set(gca,'Fontsize',16);
plot(width_int, delta, 'r-', width_int, beta_c0, 'g-', width_int, k, 'b-',
'Marker','o','MarkerSize', 2);hold on;
plot(width_int, ref, 'k--');
grid;
legend('\delta','\beta_c','k');
title('\fontsize{18}Propagation parameters');
xlabel('\fontsize{16}Width of taper (\mum)');
ylabel('\fontsize{16}Propagation constant (1/\mum)');

figure;
set(gca,'Fontsize',16);
plot(width_int, gamma, 'r-','Marker','o','MarkerSize', 2); hold on
plot(width_int, ref, 'k--');
grid;
legend('\gamma');
title('\fontsize{18}Normalized mismatch of propagation constants');
```

```
xlabel('\fontsize{16}Width of taper (\mum)');
ylabel('\fontsize{16}Propagation constant (1/\mum)');

%%%%%%%%%%%%%%%%%%%%%%%%%%%%%%%%%%%%%%%%%%%%%%%%%%%%%%%%%%%%%%%%%%%%%%%
Model cascade: construct model for different taper structures
%%%%%%%%%%%%%%%%%%%%%%%%%%%%%%%%%%%%%%%%%%%%%%%%%%%%%%%%%%%%%%%%%%%%%%%

% For two-stage tapers
N2=length(beta_c0)-N1;
dz1=L1_tot/(N1-1);
dz2=(L2_tot-L1_tot)/N2;
L1=[0:dz1:L1_tot];
L2=[L1_tot+dz2:dz2:L2_tot];
L=[L1,L2];

MT=1;
beta_c=zeros(1,length(beta_c0)-1);
delta_c=zeros(1,length(beta_c0)-1);
k_c=zeros(1,length(beta_c0)-1);
kapa=zeros(1,length(beta_c0));
tran=zeros(1,length(beta_c0));
kapa(1)=0;
tran(1)=1;
phase=0;
wave_start=[1;0];

for i=1:length(beta_c0)-1
   beta_c(i)=(beta_c0(i)+beta_c0(i+1))/2;
   delta_c(i)=(delta(i)+delta(i+1))/2;
   k_c(i)=(k(i)+k(i+1))/2;
   dz=L(i+1)-L(i);
   sp=delta_c(i)*dz+2*phase;
   MT0=[(cos(beta_c(i)*dz)+j*delta_c(i)/beta_c(i)*sin(beta_c(i)*dz))*exp(-
j*delta_c(i)*dz) (-j*k_c(i)/beta_c(i)*sin(beta_c(i)*dz))*exp(-j*sp);(-
j*k_c(i)/beta_c(i)*sin(beta_c(i)*dz))*exp(j*sp) (cos(beta_c(i)*dz)-
j*delta_c(i)/beta_c(i)*sin(beta_c(i)*dz))*exp(j*delta_c(i)*dz)];
   MT=MT0*MT;
   phase=phase+delta_c(i)*dz;
   wave_end=MT*wave_start;
   kapa(i+1)=abs(wave_end(2))^2;
   tran(i+1)=abs(wave_end(1))^2;
end

figure;
```

```
set(gca,'Fontsize',16);
plot(L,kapa,'r','Marker','o','MarkerSize', 2);hold on
grid;
title('\fontsize{18}Adiabatic Taper 1-1.6-3.5&2:1');
xlabel('\fontsize{16}Length (\mum)');
ylabel('\fontsize{16}Coupling efficiency');

% % For linear tapers
%
%    L_tot=5000;
%    dz=L_tot/(length(beta_c0)-1);
%    L=[0:dz:L_tot];
%
%    MT=1;
%    beta_c=zeros(1,length(beta_c0)-1);
%    delta_c=zeros(1,length(beta_c0)-1);
%    k_c=zeros(1,length(beta_c0)-1);
%    kapa=zeros(1,length(beta_c0));
%    tran=zeros(1,length(beta_c0));
%    kapa(1)=0;
%    tran(1)=1;
%    phase=0;
%
%    for i=1:length(beta_c0)-1
%       beta_c(i)=(beta_c0(i)+beta_c0(i+1))/2;
%       delta_c(i)=(delta(i)+delta(i+1))/2;
%       k_c(i)=(k(i)+k(i+1))/2;
%       dz=L(i+1)-L(i);
%       sp=delta_c(i)*dz+2*phase;
%       MT0=[(cos(beta_c(i)*dz)+j*delta_c(i)/beta_c(i)*sin(beta_c(i)*dz))*exp(-
j*delta_c(i)*dz) (-j*k_c(i)/beta_c(i)*sin(beta_c(i)*dz))*exp(-j*sp);(-
j*k_c(i)/beta_c(i)*sin(beta_c(i)*dz))*exp(j*sp) (cos(beta_c(i)*dz)-
j*delta_c(i)/beta_c(i)*sin(beta_c(i)*dz))*exp(j*delta_c(i)*dz)];
%       MT=MT0*MT;
%       phase=phase+delta_c(i)*dz;
%       kapa(i+1)=abs(MT(2,1))^2;
%       tran(i+1)=abs(MT(1,1))^2;
%    end
%
%    figure;
%    set(gca,'Fontsize',16);
%    plot(L,kapa,'r','Marker','o','MarkerSize', 2);
% %     semilogx(L,kapa,'r','Marker','o','MarkerSize', 2);
%    grid;
```

```
%     legend(['L=' num2str(L_tot) '\mum']);
%     title('\fontsize{18}Linear Tapers');
%     xlabel('\fontsize{16}Length (\mum)');
%     ylabel('\fontsize{16}Coupling efficiency');
```

VITA

Xin Xia was born in Hubei, China. He received his Bachelor of Science degree in Optoelectronics from Huazhong University of Science and Technology in China in 2006. He started pursuing his graduate study in Electrical and Computer Engineering Department at Texas A&M University in September 2006. He received his Ph.D. degree in May 2011. His research interests include the design of integrated optical devices and the development of fabrication process.

Dr. Xia may be reached at Texas A&M University, Electrical and Computer Engineering Department, College Station, TX, 77843-3128. His email is pursuenp@gmail.com.